INTERFACE AND SIZE EFFECTS ON TiN-BASED NANOSTRUCTURED THIN FILMS

A Dissertation

by

ICKCHAN KIM

Submitted to the Office of Graduate Studies of
Texas A&M University
in partial fulfillment of the requirements for the degree of

DOCTOR OF PHILOSOPHY

May 2011

Major Subject: Electrical Engineering

Interface and Size Effects on TiN-based Nanostructured Thin Films

Copyright 2011 Ickchan Kim

INTERFACE AND SIZE EFFECTS ON TiN-BASED NANOSTRUCTURED THIN FILMS

A Dissertation

by

ICKCHAN KIM

Submitted to the Office of Graduate Studies of
Texas A&M University
in partial fulfillment of the requirements for the degree of

DOCTOR OF PHILOSOPHY

Approved by:

Chair of Committee,	Haiyan Wang
Committee Members,	Jun Kameoka
	Jim Ji
	Lin Shao
Head of Department,	Costas Georghiades

May 2011

Major Subject: Electrical Engineering

ABSTRACT

Interface and Size Effects on TiN-based Nanostructured Thin Films. (May 2011)

Ickchan Kim, B.S., In-Ha University, Incheon, Korea;

M.S., Texas A&M University

Chair of Advisory Committee: Dr. Wang, Haiyan

Titanium nitride coatings have been widely applied and studied as high temperature diffusion barrier for silicon devices in microelectronics, wear resistant coatings in turbine blade materials, and materials for future high temperature nuclear reactors. In order to enhance the material property, superlattices is one of artificially engineered protective coatings, such as AlN/TiN and TaN/TiN multilayered films.

Epitaxial cubic multilayer films, TaN/TiN and AlN/TiN nanolayers were grown on Si(001) by Pulsed Laser Deposition (PLD) with various nanolayer thicknesses and number of interfaces. Microstructural studies include X-ray diffraction (XRD), transmission electron microscopy (TEM), and high resolution TEM with ion-irradiation experiments. Electrical, mechanical and thermal property studies were conducted for the interface and size effects on the nanolayers by using nanoindentation and Transient Thermo-Reflectance (TTR) methods.

The microstructural and hardness study on TaN/TiN films with ion irradiation (12 keV and 50 keV He^{+}) suggest no obvious microstructural or mechanical behavior change due to ion irradiation. In addition, titanium nitride that serves as effective

diffusion barrier to prevent the inter-diffusion between the nuclear fuel and the cladding material was studied in order to enhance the lifetime of the fuels and the reliability of the fuel claddings. The TiN has good adhesion with the stainless steel and higher hardness than that of bulk TiN on the stainless steel. Thermal conductivity test demonstrates that thin TiN film has compatible thermal conductivity as the MA957 and HT-9 bars.

The size effect on electrical resistivity is dominant in both of the epitaxial cubic and the polycrystalline TiN thin films in the thickness ranged from ~60 nm down to ~35nm. In the TaN/TiN multilayer, the grain scattering effect on resistivity is dominant rather than interface influence on the resistivity with comparing epitaxial cubic phase and polycrystalline phase.

The microstructure and hardness studies of the AlN/TiN multilayer films with He^{+} implantation present that the suppression of amorphization in AlN layers and the reduction of radiation-induced softening were achieved in all nanolayer films. Radiation tolerance was found to be size dependent and the layer thickness leading to the highest radiation tolerance was around 10 nm. In addition, the embedded epitaxial cubic AlN with cladding TiN nanolayers showed higher effective thermal conductivity than that of AlN single layer as well as the embedded polycrystalline AlN in the thickness ranged from 10 nm down to 2 nm. It confirms a suppressed size effect, which reduces the amount of decrease in through-plane thermal conductivity.

DEDICATION

Dedicate to my family,

Courtney Kim, Conrad Hyunsoo Kim, and Keumsil Kang

ACKNOWLEDGEMENTS

I would like to thank my committee chair, Dr. Haiyan Wang, and my committee members, Dr. Jun Kameoka, Dr. Jim Ji, and Dr. Lin Shao, for their guidance and support throughout the course of this research.

Special appreciation must go to my lab members in Dr. Wang's group, Dr. Xinghang Zhang, Dr. Mihai G. Burzo, Dr. Pavel L. Komarov, and Dr. Peter E. Raad for their help in experimental accomplishments, valuable suggestions, and critical advice. I also deeply appreciate Dr. Lin Shao and Dr. Xinghang Zhang for their kindness and allowing me to use their apparatus in laboratory.

Many thanks go out to Dr. Yulia Vasilyeva and Dr. William Lackowski for their advice and helping me use the experimental apparatus in the Materials Characterization Facility (MCF) Laboratory. I deeply appreciate the very kind and helpful advice of Dr. Jaime Grunlan for the scientific study.

I would particularly like to thank Dr. Michael Pendleton, and Mr. Tom Stephens, for their advice and help in using the apparatus of the Microscopy and Imaging Center (MIC).

Thanks also to my friends, colleagues, and the department faculty and staff for making my time at Texas A&M University a great experience.

Finally, appreciate my wife, daughter, and son, for their encouragement, patient support, and love.

TABLE OF CONTENTS

Page

ABSTRACT iii

DEDICATION v

ACKNOWLEDGEMENTS vi

TABLE OF CONTENTS vii

LIST OF FIGURES ix

LIST OF TABLES xiv

CHAPTER

I INTRODUCTION 1

1.1 Introduction 1
1.2 Interface and size effects in thin films 3
1.3 Material properties of TiN, TaN, and AlN 10
1.4 Outline 13

II RESEARCH METHODOLOGY 15

2.1 Pulsed laser deposition method 15
2.2 X-ray diffraction 28
2.3 Transmission electron microscopy 34
2.4 Transient thermo-reflectance method 44
2.5 Measurement uncertainty of TTR method 51
2.6 Four-point probe method 53

III EPITAXIAL TaN/TiN NANOLAYERS WITH UNIQUE ELECTRICAL AND RADIATION TOLERANCE PROPERTIES 58

3.1 Overview 58
3.2 Introduction 59

CHAPTER Page

3.3 Experimental details 61
3.4 Results and discussion 64
3.5 Summary 82

IV HIGHLY TEXTURED AND EPITAXIAL AlN/TiN NANOLAYERS WITH ENHANCED RADIATION TOLERANCE PROPERTIES 84

4.1 Overview 84
4.2 Introduction 84
4.3 Experimental details 87
4.4 Results and discussion 88
4.5 Summary 104

V EXPERIMENTAL INVESTIGATION OF SIZE EFFECT AND PHASE INFLUENCE ON THERMAL PROPERTY OF TiN/AlN/TiN NANOLAYERS 105

5.1 Overview 105
5.2 Introduction 106
5.3 Experimental details 109
5.4 Results and discussion 113
5.5 Summary 133

VI TiN-BASED COATINGS FOR FUEL CLADDING TUBES 136

6.1 Overview 136
6.2 Introduction 136
6.3 Experimental details 138
6.4 Results and discussion 142
6.5 Summary 157

VII SUMMARY AND CONCLUSIONS 158

REFERENCES 161

VITA 168

LIST OF FIGURES

FIGURE Page

1.1 Hardness change of Cu/V multilayer after ion irradiation vs. individual layer thickness by Fu *et al.* 4

1.2 Precise control of thermal conductivity at the nanoscale through individual phonon-scattering barriers by Pernot *et al.* 7

1.3 Length scale effect on the electronic transport properties of nanometric Cu/Nb multilayers: (a) Resistivity of Cu/Nb multilayered films and (b) Resistivity for pure Cu and pure Nb thin films by Lima *et al.*. 9

2.1 Schematic diagram of a single target pulsed laser deposition system. 16

2.2 Schematic diagram showing the different phases present during laser irradiation of a target: (A) unaffected target, (B) evaporated target material, (C) dense plasma absorbing laser radiation, and (D) expanding plasma outer edge transparent to the laser beam.. 24

2.3 Diffraction for a set of planes with inter-plane distance d which is conditioned to Bragg's Law.. 30

2.4 Schematic of an X-ray diffractometer. 33

2.5 The variation of light intensity across a set of Airy rings. Most of the intensity (84%) lies within the first ring that is within a spot of diameter d_1.. 37

2.6 The intensity of the Airy rings from two neighboring pinholes. The intensity distributions from each of the pinholes separately are shown as solid lines; the combined profile from the two pinholes acting together is shown dotted. At the Rayleigh resolution limit, as shown here, the maximum intensity from one pinhole coincides with the first minimum from the other giving a resolution limit of $d_1/2$. 38

2.7 Schematic of lenses in a transmission electron microscope. Note the dashed line indicating one group of diffracted electrons that converge in the back focal plane of the objective lens. 43

FIGURE Page

2.8 Schematic of the Transient Thermo-Reflectance (TTR) system in NETSL at SMU by Burzo *et al.* 46

2.9 A collinear four-point probe array. 55

3.1 Schematic of prepared TiN/TaN nanolayer film with different nanolayer thickness for radiation tolerance experiment 62

3.2 Schematic of prepared TiN/TaN nanolayer film with different number of interface and nanolayer thickness for electrical resistivity measurement 62

3.3 SRIM calculation: comparison of damage profile for TiN/TaN 16/2 nm multilayer, TiN, and TaN single layers by 12 keV He^{+} ion implantation 65

3.4 SRIM calculation: comparison of damage profile for TiN/TaN 20/5 nm multilayer, TiN, and TaN single layers by 50 KeV He+ ion implantation 66

3.5 TEM image of TiN/TaN (20/5nm) multilayer as-deposited 67

3.6 TEM image of TiN/TaN multilayer after ion implantation (50keV) 68

3.7 TaN/TiN (16/2nm) nanolayer after ion irradiation: TEM examination suggests that the crystalline structure of the nanolayer structure remains after 12keV He, $4x10^{16}/cm^2$. Some He accumulation is observed at the layer interfaces 70

3.8 STEM image (a) of 2/16 nm TaN/TiN and EDX analysis (b) after ion irradiation with 12 keV 71

3.9 Hardness of TaN/TiN specimens as-deposited and ion-irradiated with 50 keV and 12 keV He^{+} 73

3.10 Cross-sectional TEM images with selected diffraction patterns of TaN/TiN nanolayers with various thicknesses and interfaces between TaN and TiN layers on TiN Buffer layer: epitaxial cubic phase TaN/TiN (a), (b), and (c) and poly-crystalline TaN/TiN (d), (e), and (f) 75

3.11 High resolution cross-sectional TEM images of epitaxial 4nm and polycrystalline 2nm thick TaN specimens in TaN/TiN 76

FIGURE Page

3.12 Resistivity as a function of film thickness on TiN films deposited at 800 °C........ 78

3.13 Measured resistivity on epitaxial cubic phase and polycrystalline TiN single layers with various thicknesses........ 79

3.14 Measured resistivity on epitaxial cubic phase and polycrystalline TaN/TiN nanolayers with various number of interface......... 81

4.1 SRIM simulation provides a guideline for the ion radiation experiment and compares damage vs. depth after ion implantation of 50 keV He ion for TiN and AlN single layers........ 89

4.2 Low magnification XTEM micrographs and selected area diffraction (SAD) patterns of AlN single layer films for (a) as-deposited and (b) ion-irradiated with He^+ 50 keV ions at a dose of $4x10^{16}$ cm^{-2}, and (c) HRTEM image and FFT of the amorphized regime in AlN single layer film after radiation........ 90

4.3 Low magnification XTEM micrographs and SAD patterns of TiN/AlN 20/20 nm sample: (a) as-deposited and (b) ion-implanted with He^+ 50 keV ions at a dose of $4x10^{16}$ cm^{-2}........ 92

4.4 Low magnification XTEM micrographs and SAD patterns of TiN/AlN 5/5 nm sample: (a) as-deposited and (b) ion-implanted with He^+ 50 keV ions at a dose of $4x10^{16}$ cm^{-2}........ 93

4.5 HRTEM micrographs and SAD patterns of TiN/AlN 20/20 nm sample: (a) as-deposited and (b) ion-irradiated with He^+ 50 keV ions at a dose of $4x10^{16}$ cm^{-2}........ 94

4.6 High resolution cross-section TEM micrographs and SAD patterns of TiN/AlN 5/5 nm sample: (a) as-deposited and (b) ion-irradiated with He^+ 50 keV ions at a dose of $4x10^{16}$ cm^{-2}........ 95

4.7 Hardness vs. indentation depth for (a) as-deposited and (b) ion-irradiated TiN and AlN single layer and TiN/AlN multilayer films........ 97

4.8 (a) Averaged hardness vs. nanolayer thickness for as-deposited and ion-irradiated TiN/AlN nanolayer films and (b) Hardness decrement vs. nanolayer thickness for all nanolayer samples with dashed lines indicating the hardness reduction for single layer AlN and TiN samples........ 99

FIGURE Page

5.1 Schematic cross-section of sample with applied TTR measurement: (a) TiN single layer, (b) AlN single layer, and (c) embeded AlN layer with various thicknesses between TiN layers on TiN Buffer layer....................... 110

5.2 (a) Schematic of gold deposited TiN/AlN/TiN sample to apply TTR method and (b) Schematic of the Transient Thermo-Reflectance (TTR) System in NETSL at SMU by Burzo et al 111

5.3 Cross-sectional TEM images with selected diffraction patterns of embeded AlN layer with various thicknesses (8 nm, 4 nm, and 2 nm) between TiN layers on TiN Buffer layer: Embedded epitaxial cubic AlN (a, b, and c) and poly-crystalline AlN (d, e, and f) in TiN layers.................................... 114

5.4 HR TEM images of 2 nm (a) epitaxial cubic AlN and (b) polycrystalline AlN layers 115

5.5 HR TEM images of 2 nm epitaxial cubic AlN layer that noise filtered by Fast Fourier Transform (FFT) 116

5.6 Measured intrinsic thermal conductivities (K_{int}) of TiN single layers depending on thickness and crystal structure 124

5.7 Normalized TTR response and the matched numerical response within 1.5% error for embedded AlN layers: 1.8 nm, 2.8 nm, and 8.8 nm epitaxial cubic AlN layers... 127

5.8 Effective thermal conductivity (K_{eff}) of embedded AlN layers depending on layer thickness and crystal structures 129

6.1 Optical microscope images of TiN/HT-9 and TiN/MA-957 specimens showing very smooth surface of the coatings 139

6.2 (a) As-deposited and thermal-cycle tested TiN/HT-9 and TiN/MA957 specimens and (b) thermal cycle test: the maximum temperature is 570 °C in vacuum of 10^{-7} Torr. 141

6.3 Plan-view SEM Image of 2μm TiN/HT-9 as-deposited and thermal cycle tested with low magnification 144

6.4 Plan-view SEM Image of 2μm TiN/MA-957 as-deposited and thermal cycle tested with high magnification... 144

FIGURE Page

6.5 Cross-sectional SEM images (a) before and (b) after thermal cycle tested TiN/HT-9 tube 145

6.6 Load vs. depth of nanoindentation measurements before and after thermal-cycle test: (a) TiN/HT-9 and (b) TiN/MA957 147

6.7 SEM image of a scratch test track on TiN/HT-9 sample after scratch test with (a, b) 30 mN, (c, d) 60 mN, and (e, f) 90 mN normal load 149

6.8 Schematic cross-section of sample with applied TTR measurement 151

6.9 Measured intrinsic thermal conductivity (K_{int}) of HT-9 and MA957 by TTR method 152

6.10 Measured intrinsic thermal conductivity (K_{int}) of TiN on HT-9 and MA957 by TTR method and calculated effective thermal conductivity (K_{eff}) of TiN/HT9 and TiN/MA957 154

6.11 TEM image of Ce/TiN (200 nm) /HT-9 after annealing: Ce diffusion test on TiN/HT-9 at 600 °C for 12 hours at vacuum pressure of 1×10^{-6} mbar 155

LIST OF TABLES

TABLE Page

1.1 Material properties of TiN, TaN, and AlN at room temperature. 13

5.1 Thermal and optical properties of the Au layer deposited on samples 118

5.2 Properties of the samples utilized in the TTR system 122

5.3 Properties of the samples utilized to measure thermal property of the embedded AlN by TTR system.. 126

6.1 Hardness of TiN/HT-9 and TiN/MA-957 specimens 146

CHAPTER I

INTRODUCTION

1.1 Introduction

There are numerous applications for the use of thin films such as diffusion barrier in microelectronics, enhanced radiation tolerance in nuclear power plant, thermoelectric device, and lubricating coatings. As technology proceeds towards smaller and more effective device, one faces varied material properties in thin films, which are dissimilar to bulk materials due to size effect so-called. Thus, it is necessary to identify new materials or materials with new structures to meet the various demands for suitable properties in the thin film applications. One typical new structure is a nanolayered structure containing many thin layers, where both of size and interface effects on material property shall be considered.

For this study metal-nitride thin films are selected. Metal-nitride thin films are useful materials with numerous current and foreseeable industrial applications as well as great interest to the scientific community. Although most of their applications are recent; these so-called refractory nitrides have been known for over one hundred years because of their high melting points and chemical inertness. Recently nitride-based thin film have attracted a lot of research efforts for improving hard coating applications, diffusion

---

This dissertation follows the style and format of Journal of Nuclear Materials.

barriers for metal gates or contacts in micro-electronic devices, and optical light emitting diodes. The wide range of applications reflect the variety of these materials and the diversity of the industry needs [1-3].

In addition, nitrides are considered to be one of the advanced nuclear fuel forms for waste storage and can be a potential diffusion barrier to minimize fuel-cladding interactions [4, 5]. Ion irradiation-induced amorphization in ceramics has been previously reported as one primary degradation phenomenon in ceramics [6]. In spite of the fact that the ion irradiation damage has been studied in several nanolayered metallic systems [7, 8], similar studies on nanostructured or nanolayered ceramics [5, 9, 10] are still scarce.

As decreasing nanolayer thickness and depending on crystal phase in the nanolayer system, the electrical and thermal properties also dramatically vary [11-15] from bulk values as well as mechanical property and radiation tolerance. These features have been a fundamental challenge for nanoelectronics heat and electrical resistivity management in microelectronics. Moreover, the interface in multilayer films is another major factor to decide material properties as interfacial point defects and misfit dislocations vary significantly indifferent systems.

The nitride-based materials studied and presented in this dissertation are the transition metals nitrides such as TiN, TaN and AlN, either as a single layer or a multilayer structure. In this study, the interface and size effects as well as crystal phase influence on radiation tolerance and on electrical thermal properties were studied for

thin TaN/TiN and AlN/TiN multilayered films with varied nanolayer thickness, interfacial density and crystal phase such as epitaxial cubic phase and polycrystalline.

1.2 Interface and size effects in thin films

Enhanced radiation tolerance in nanocrystalline or nanolayered metallic systems have been reported both experimentally and theoretically. For example, microstructural changes caused by helium ion-irradiation in several multilayer systems, including immiscible Cu/Nb [16], Cu/V [7], and miscible Al/Nb [17], and Fe/W [8], have been systematically studied. It was reported that certain type of immiscible interfaces, such as Cu/V as shown in Fig. 1.1, could significantly enhance ion-irradiation tolerance of metallic materials compared with bulk counterpart. Dramatic reductions of swelling, bubble density, lattice expansion and radiation hardening are observed in Cu/V multilayers, wherein interface act as effective sinks to absorb radiation induced point defects and promote the annihilation of opposite type of defects (Frenkel pairs), and consequently reduce the overall point defect density in the multilayers [7, 8, 16, 18].

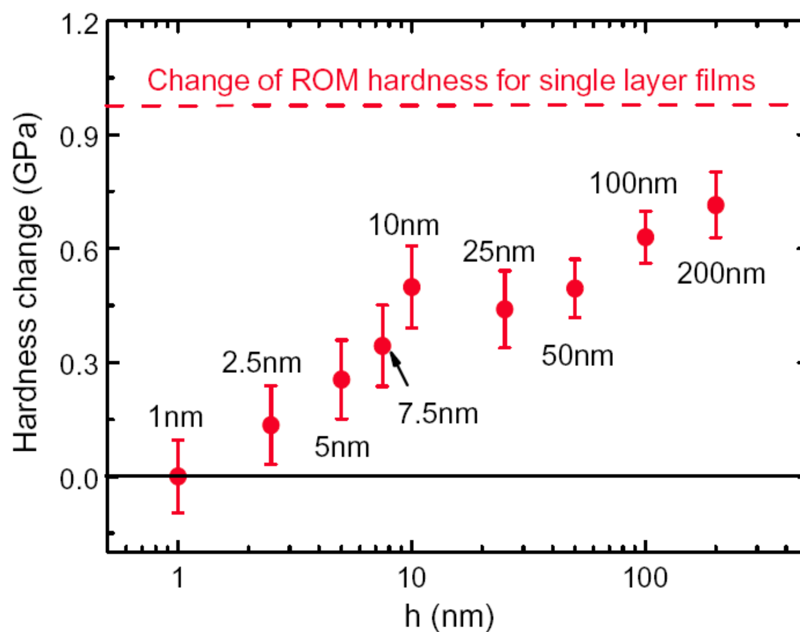

Fig. 1.1 Hardness change of Cu/V multilayer after ion irradiation vs. individual layer thickness by Fu *et al.*[7]

Size effect on the thermal and electronic transport properties was studied by varying nanolayer thickness in single layer and multilayers. Based on the kinetic theory, thermal conductivity for a solid can be calculated as follows, Rohsenow and Choi [19], Cahill *et al*.[20], and Omar, M. A.[21]:

$$K = \frac{1}{3} C_v v l \tag{1.1}$$

where K is the thermal conductivity, $C_v = C_s$ is the phonon specific heat per unit volume, $v = v_s$ is the averaged acoustic speed, and $l = l_s$ is the phonon mean free path in for dielectric materials. For thermal conduction in metals, $C_v = C_e$ is the electronic specific heat per unit volume, $v = v_e$ is the electron speed at Fermi levels, and $l = l_e$ is the electron mean free path at Fermi levels. Having investigated thermal properties of metallic and dielectric materials based on Eq. (1.1), researchers have shown a “Size Effect” in ultra-thin (sub 100 nm) and thin (sub 1 μm) films. Flik *et al*.[22] showed that boundary scattering increases with ratio l/h, where l is the bulk value of the mean free path of the heat carriers and h is the film thickness in metallic and dielectric materials. If the film thickness h is less than or approaches l, the effect of boundary scattering must be considered while the volume resistance of the film may be neglected when $l \ll h$. Moreover, Flik showed that the microscale regime criteria has to be used for thermal conduction in both metallic and dielectric films if $h < 7l$, which is the dimension that separates the microscale and macroscale regimes.

In multilayer films, the thermal conductivity of the embedded layer has not only the classical size effect, such as diffusive boundary scattering, but also the effect of partial phonon spatial confinement due to the partial reflections and transmissions of lattice waves at the layer boundary with dissimilar elastic properties. Zou *et al.*[12] described that the effect of partial phonon confinement leads to a higher thermal conductivity of the embedded GaN layer in an AlN/GaN/AlN heterostructure than that in a single GaN thin film with the same total structure thickness. Based on the solution of the phonon Boltzmann equation in the phonon relaxationtime approximation, they entered the partial phonon spatial confinement effect in the calculation for the thermal conductivity through phonon dispersion, phonon group velocity, quasi-two-dimensional (2D) phonon density of states, and phonon scattering rates. The simulated thermal conductivity of the embedded GaN layer showed a thickness dependence with varying the thicknesses of the embedded GaN layer or the cladding layers (AlN) [12]. Point defect and dislocation density will affect the phonon scattering rate, and the specifics of the boundary condition depend on the relative elastic properties of the interfacing materials.

Costescu's group measured thermal conductance of interfaces between epitaxial TiN and single crystal oxides (TiN/MgO(001), TiN/MgO(111), and TiN/Al_2O_3(0001)) at temperatures between 79.4 and 294 K by applying the time-domain thermoreflectance (TDTR) method [23]. The thermal conductance $G \approx 700$ M W m^{-2} K^{-1} (interface resistance R=G^{-1}=0.143×10^{-8} m^2 K W^{-1}), is about 5 times higher than the highest values reported previously for any individual interface near room temperature. The interface

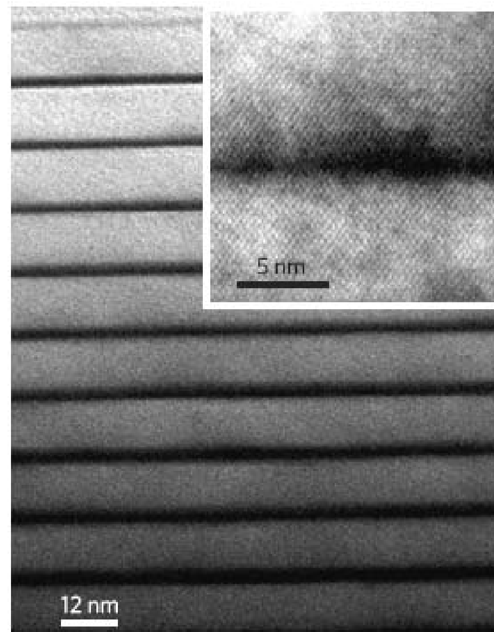

(a)

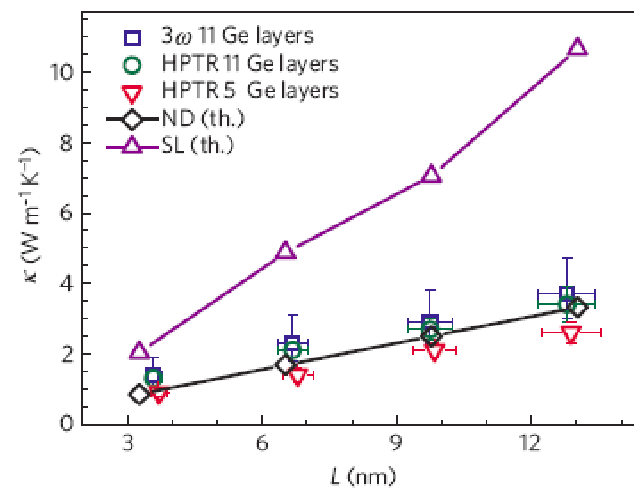

(b)

Fig. 1.2 Precise control of thermal conductivity at the nanoscale through individual phonon-scattering barriers by Pernot *et al.*[24]

thermal resistance can be compared with 1.68×10^{-8} m^2 K W^{-1} and 0.78×10^{-8} m^2 K W^{-1} in the interfaces of Au/SiO_2/Si and Au/Cr/SiO_2/Si without epitaxy, respectively [25]. Although the number of interfaces was increased in Au/Cr/SiO_2/Si, the sum of interface resistance was reduced in the sample. In addition, epitaxial TiN and single crystal oxides shows a 5 times higher interface thermal resistance than Au/Cr/SiO_2/Si without epitaxy.

Costescu's group [23] did not observe significant differences in G for the three TiN interfaces. In particular, the 8% in-plane lattice mismatch between TiN(111) and Al_2O_3(0001)—and the interface stacking faults in the TiN/MgO(111) and TiN/Al_2O_3 samples—do not modify the thermal transport properties significantly. Apparently, the additional interface disorders in these samples did not change the phonon transmission coefficient significantly.

Using highly phonon diffusive interfaces by nanodot systems, Pernot *et al.*[24] achieved a room-temperature thermal conductivity, K, down to about 0.9 W m^{-1} K^{-1}, in SiGe/Si multilayered structures with as little as five barriers as shown in Fig. 1.2. This demonstrated the ability to controll thermal conductivity with 1 W $m^{-1}K^{-1}$ precision and spatial resolution below the 20 nm range is very relevant to the development of integrated miniaturized energy harvesting or thermal management devices. The highly diffusive interfaces permit the precise control of thermal conductivity at the local level. The result suggests that possibly electronic properties may be controlled simultaneously as well.

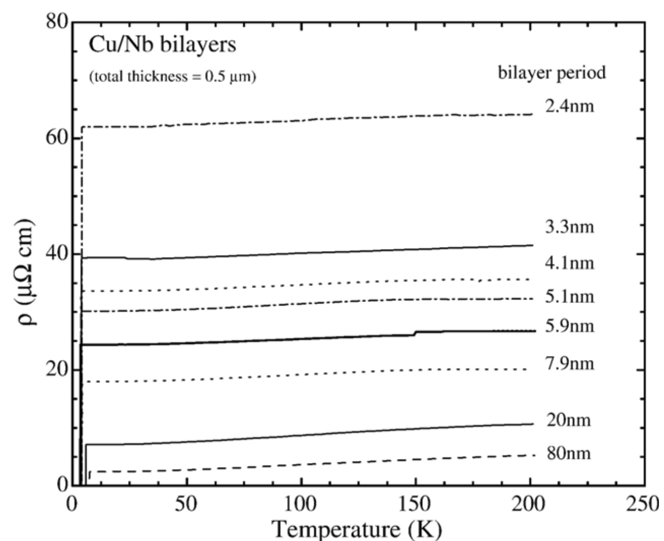

(a)

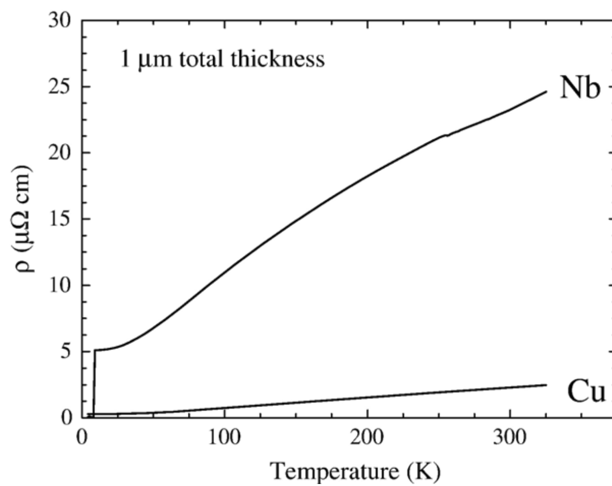

(b)

Fig. 1.3 Length scale effect on the electronic transport properties of nanometric Cu/Nb multilayers: (a) Resistivity of Cu/Nb multilayered films and (b) Resistivity for pure Cu and pure Nb thin films by Lima *et al*.[11]

Lima *et al*.[11] studied the effects of interface and grain boundary scattering on the electrical resistivity of Cu/Nb multilayers with varying bilayers thickness. They reported that the resistivity seems to be related to the thickness of the individual layers rather than the total film thickness with showing the relative importance of the grain boundary and the interface scattering. As shown in Fig. 1.3(a), the resistivity was increased over 60 μΩcm as the bilayer period decreased down to 2.4 nm, and this value is much higher than that of Nb and Cu single layers as shown in Fig. 1.3(b). Their results suggest a clear correlation between the resistivity and the bilayer thickness. When the thickness of each individual layer is comparable to the electronic mean free path, interface scattering is predominant. Grain boundary scattering was shown to be particularly important to the thicker films [11].

1.3 Material properties of TiN, TaN, and AlN

TiN has been extensively used as a hard wear resistant coating for cutting tools, and as corrosion and abrasion resistant layers on optical and mechanical components. Further elaboration on the microstructure and composition of nitride films has improved dramatically some properties of these nitride films [26], a quick example shows that nanocrystalline quality of TiN films enhances grain boundary sliding and grain boundary diffusion related creep phenomena, and further improve the ductility of coatings. On the other hand, compositional designed TiN based alloys, such as cubic-phase $Ti_{1-x}Al_xN$ thin films in a state of compressive residual stress, and compositionally modulated nitride

films such as multilayer and superlattices, show much higher thermal stability and better mechanical property [27-29].

Tantalum nitride (TaN_x) has a variety of different phases as it will be shown in the next chapter, with all sharing similar characteristics such as very high melting point and elevated heat of formation. The stoichiometric TaN phase exhibits a melting point T_m=3093°C, and a heat of formation ΔH_f (298 K) = -252.3 kJ/mol, which demonstrates excellent structural stability at elevated temperatures. Moreover the TaN_x/Si interface is more stable than its counterpart Ta/Si, based on the higher activation energy needed for silicide formation in the case of tantalum nitride. This property is attributed to the increased thermal budget required to ensure the dissociation of Ta-N bonds prior to the formation of Ta-Si bonds [30]. From the structural perspective, all TaN_x phases can be simply described as close-packed arrangements of Ta atoms, with the smaller N atoms inserted into interstitial sites. The processing and property correlations of TaN thin films are studied as radiation barriers by epitaxial cubic phased TaN/TiN nanolayered film.

Aluminum nitride has a hexagonal crystal structure in bulk and is a covalent bonded material. However, it was revealed that the crystal structure of AlN changes from Wurtzite type to NaCl type for superlattice and the film hardness dramatically increased [31]. NaCl phase of AlN is one of the phases that exist under high pressure and it is expected that there will be a high bulk modulus. The use of sintering aids and hot pressing is required to produce a dense technical grade material. The material is stable up to very high temperatures in inert atmospheres. In air, surface oxidation occurs above 700°C. A layer of aluminum oxide forms which protects the material up to

1370°C. Above this temperature bulk oxidation occurs. Aluminum nitride is stable in hydrogen and carbon dioxide atmospheres up to 980°C. The material dissolves slowly in mineral acids through grain boundary attack, and in strong alkalis through attack on the aluminum nitride grains. The material hydrolyzes slowly in water. Most current applications are in the electronics area where heat removal is important. This material is of interest as a non-toxic alternative to beryllia. Metallization methods are available to allow AlN to be used in place of alumina and BeO for many electronic applications. Metallization methods are available to allow AlN to be used in electronics applications similar to those of alumina and beryllium oxide. Currently there is much research into developing light-emitting diodes that operate in the ultraviolet using the gallium nitride based semiconductors and, using the alloy aluminum gallium nitride, wavelengths as short as 250 nm have been achieved [14, 32, 33]. Mechanical, thermal, electrical properties of the bulk sized TiN, TaN, and AlN materials are shown in Table 1.1.

Table 1.1 Material properties of TiN, TaN, and AlN at room temperature [33]

Material	Lattice (Å)	Density (g/cm^3)	Melting Point (°C)	Resistivity (Ωμ-cm)	Hardness (GPa)	Specific Heat (J/mol.k)	Thermal Conductivity (W/m.K)	Thermal Expansion (x10^{-6}/°C)
TiN	4.24	5.4	2950	20±10	18-21	33.74	19.2	9.35
TaN	4.34	14.3	3093	135	11.0	40.60	8.78	8.0
c-AlN	4.36	3.285	–	–	–	–	–	–
h-AlN	a=3.11 c=4.98	3.255	2200	10E+20	11.8	30.30	285	a: 5.3 c: 4.2

1.4 Outline

Chapter II, which follows, shows the research methodology of the experimental work such as Pulsed Laser Deposition (PLD), X-ray diffraction (XRD), Transmission Electron Microscopy (TEM), thermal conductivity by the Transient Thermo-Reflectance (TTR) Method and resistivity measurement by four-point probe methods. Chapter III gives a study for epitaxial TaN/TiN nanolayers for electrical and radiation tolerance properties. A study on the highly textured and epitaxial AlN/TiN nanolayers with enhanced radiation tolerance properties is presented in Chapter IV. Experimental investigation of size effect and phase influence on the thermal property of TiN/AlN/TiN nanolayers is presented in Chapter V. Chapter VI shows a study for TiN-based coatings

for fuel cladding tubes. The summary and conclusions from this research are presented in Chapter VII.

CHAPTER II

RESEARCH METHODOLOGY

2.1 Pulsed laser deposition method

The development of high-intensity beam energy lasers enabled Pulsed Laser Deposition (PLD) for growing thin film, which is the main technique for deposition of the metal nitrides studied in this study. Pulsed laser deposition (PLD) is a thin film deposition technique where a high power pulsed laser beam is focused to strike a target of the material inside a vacuum chamber. The target material is evaporated as plasma plume and deposits as a thin film on a substrate such as a silicon wafer facing the target. This process can occur in ultra high vacuum or in the presence of a background gas, such as oxygen that is commonly used when depositing oxides to fully oxygenate the deposited films.

With the development of PLD theoretical and experimental studies were carried on the laser-target interaction (solid or gas) [34]. The first demonstration for the idea of thin film deposition by PLD came up in 1965 by Smith and Turner [35]. The absorbed energy in the target is first converted to electronic excitation and then into thermal, chemical and mechanical energy resulting in evaporation, ablation, plasma formation and even exfoliation [36]. The ejected species expand into the surrounding vacuum in the form of a plume containing many energetic species including atoms, molecules,

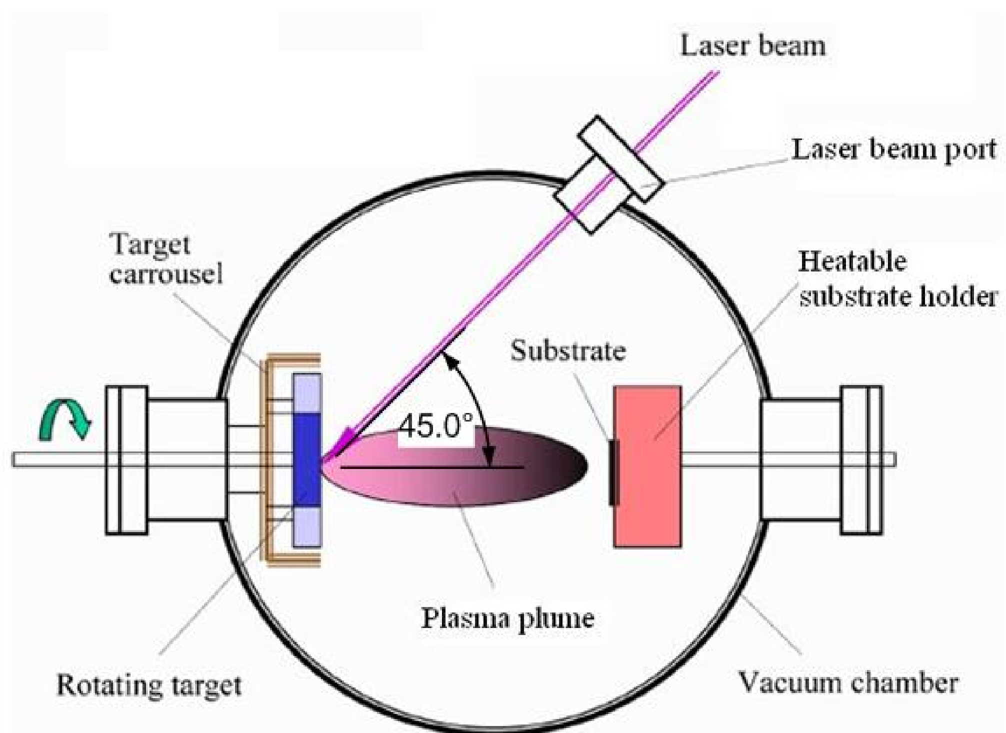

Fig. 2.1 Schematic diagram of a single target pulsed laser deposition system

electrons, ions, clusters, particulates and molten globules, before depositing on the typically hot substrate.

The main advantage of PLD method is monochromaticity, high energy density, and directionality. Monochromaticity permits the control of the depth of heat treatment or selectivity. The high energy density and directionality allows strongly localized heat and photo treatment of materials with a spatial resolution rather than its wavelength. In addition, the pulsed laser deposition method can reproduce the target stoichiometry with little contamination and in situ control of thin films properties. Figure 2.1 shows a schematic of the experimental setup. It consists of a target holder and a substrate holder in a high vacuum chamber maintained by a turbomolecular pump. The bulk target material is oriented at an angle of 45° with respect to the incident laser beam. A high-power laser beam is focused on target surface by using a set of optical components and the laser energy density is controlled depending on target materials. The evaporated material is deposited onto a substrate placed parallel to the target surface at distance of 4-6 cm.

The deposited film quality depends on various parameters such as substrate temperature, laser energy density, pulse repetition rate, pressure in the chamber, and substrate-target distance. The temperature of the substrate can be adjusted from room temperature to 800 °C depending on vacuum system. Film growth can be carried out in a reactive environment containing any kind of gas with or without plasma excitation. The basic physical principles for understanding PLD is the laser-target interactions during

the pulse duration (25 ns relying on laser) and after. It can be defined into three separate steps as follows:

(i) interaction of the laser beam with the target material resulting in the evaporation of the surface layers

(ii) interaction of the evaporated material with the incident laser beam resulting in an isothermal plasma formation and expansion

(iii) anisotropic adiabatic expansion of the plasma leading to the characteristic nature of the laser deposition process.

The first two initial regimes take place at the start and through the laser pulse duration, the third regime starts right after the laser pulse terminates [37].

(i) Interaction of the laser beam with the target material

The evaporation of the material from the target by laser irradiation depends on the interaction of the laser beam and the target. The intense heating of the surface layers by the high-energy nanosecond laser pulses results in the melting and evaporation of surface layers with some depth. The thermal parameters such as heating rate, melting and evaporation depend on: (a) lasers parameters (pulse energy density E, pulse duration τ, shape of the laser pulse, and wavelength λ), and (b) materials properties (reflectivity, absorption coefficient, heat capacity, density, thermal conductivity, etc). The heating and melting process essentially involves the solution of a three-dimensional heat flow equation that can be simplified to one-dimensional heat flow equation with the

appropriate boundary conditions and taking into account the phase changes of the material. The simplification is mainly due to the laser beam size, which is much larger than that of the melt depth, and the equation reduces to:

$$\rho_i(T)C_P(T)\frac{\partial T_i(x,t)}{\partial t} = \frac{\partial}{\partial t}\left(K_i(T)\frac{\partial T_i(x,t)}{\partial x}\right) + I_0(t)\left(1-R(T)\right)e^{-a(T)x} \qquad (2.1)$$

where

x: Direction perpendicular to the sample

t: Time

i: 1, 2 refers to the solid and liquid interface respectively

ρ_i: Temperature dependant density

$C_p(T)$: Specific heat capacity at constant pressure of the target material

$R(T)$: Temperature dependant reflectivity

$a(T)$: Absorption coefficient at the laser wavelength

$I_0\,(t)$: Incident laser intensity with time dependant

K_i : Thermal conductivities of solid and liquid phases at the interface

The evaporation characteristics of the pulsed laser irradiated material can be achieved by finite difference method. In addition, simpler calculations based on energy conservation can be applied to determine the evaporation characteristics as function of the laser and materials parameters and the amount of material evaporated per laser pulse

is calculated by using the energy conservation. The energy on the target by the laser beam is equal to the energy needed to vaporize the surface layers plus the losses due to thermal conduction of the substrate and absorption by the plasma. The vaporization energy is given by the energy threshold E_{th}, that represents the minimum energy for appreciable evaporation. Plasma and other losses and E_{th} vary with pulse energy density. Then, the heat balance equation is given by:

$$\Delta x_i = \frac{(1-R)(E-E_{th})}{\Delta H + C_v \Delta T} \tag{2.2}$$

Δx_i: Evaporated thickness

R: Reflectivity

ΔH: Latent heat

C_v: Specific heat capacity at constant volume

ΔT: Maximum temperature rise

This equation is valid for conditions where the thermal diffusion distance $\sqrt{2D\tau}$ is larger than the absorption length of the laser beam in the target material, $1/\alpha_t$.The term D refers to the thermal diffusivity and τ refers to the laser pulse duration.

(ii) Interaction of the laser beam with the evaporated material

The laser induced high surface temperature (> 2000K) of the target material results in the emission of positive ions and electrons from the free surface. The emission of electrons from a solid surface can be described by the Richardson's equation that shows an exponential increase in the electron emission as a function of temperature. The thermionic emission of positive ions can be calculated by the Langmuir-Saha equation that shows a similar relation with temperature as the electron emission. This equation is expressed as follows:

$$\frac{i_+}{i_0} = \left(\frac{g_+}{g_0}\right) \exp^{(\phi - I)/KT} \tag{2.3}$$

where i_+ and i_0 are the positive and neutral ion fluxes leaving the surface at a temperature T respectively, g_+ and g_0 represent the statistical weight of the positive ionic and neutral states, ϕ is the electron work function, and I is the ionization potential of the material coming from the target surface. The fraction of the ionized species increases with increasing the temperature due to $I > \phi$. The surface temperature is close to the boiling point of the target material (~ 3000K) and higher temperatures can be achieved in the evaporated plasma by the interaction of the laser with it. The penetration and absorption of the laser beam by the plasma depends on the electron-ion density, temperature, and the wavelength of the laser radiation. The plasma frequency v_p should

be lower than the laser frequency for penetration and absorption, otherwise all the radiation would be reflected by the plasma. For instance, an excimer laser (KrF) wavelength of λ=248 nm, its corresponding laser frequency is 12.097 x 10^{14} s^{-1}, then the plasma frequency is given by the expression as follows:

$$\nu_p = 8.9 \times 10^3 n_e^{0.5} \qquad (2.4)$$

where n_e is the electron concentration in the plasma. Using the above equation, the calculated critical electron density for the laser radiation reflection by the plasma is found to be 1.35 x 10^{22} cm^{-3}. This critical electron density value is about the concentrations of atoms in a solid or liquid. The presence of a diffused plasma boundary and the gradual decrease in the plasma density away from the surface results in a even much lower density than the calculated value. Therefore, energy loss caused by the reflection of the excimer laser due to the plasma is assumed minimum.

The material evaporated from the hot target surface is further heated by the absorption of the laser radiation. Although the laser evaporation for the deposition of thin films occurs at much lower power densities, where plasma temperatures are of the order of 10000 K, the heating mechanism and other physical phenomena are similar to the laser-generated high temperature plasma. The initial temperature of the evaporated material depends on the absorption of energy by the plasma. It has been found that the primary absorption mechanism for the ionized plasma is due to the electron-ion collisions. The absorption occurs by an inverse Bremsstrahlung process, which involves

the absorption of a photon by a free electron. However, during the initial stages of the laser pulse when very low electron and ion densities and a large number of neutral atoms are present, free-free transitions involving neutral atoms may provide the primary absorption mechanism. With a slight increase in ion density, the free-free transitions involving ions take over and become the dominant mechanism for laser absorption. The absorption coefficient α_p (cm^{-1}) of the plasma for free-free transitions involving ions can be expressed as,

$$\alpha_p = 3.69 \times 10^8 \left(\frac{Z^3 n_i^2}{T^{0.5} \nu^3} \right) \left(1 - e^{-h\nu/KT} \right) \tag{2.5}$$

where *Z*, *ni* and *T* are the average charge, ion density, and temperature of the plasma respectively; *h*, *K*, and *v* are the Planck constant, Boltzmann constant, and frequency of the laser radiation respectively. The laser energy is highly absorbed if ($\alpha_p X$) is large, where *X* is the dimension perpendicular to the target of the expanding plasma. This equation shows that the absorption coefficient of the plasma is proportional to ni^2. Thus the plasma absorbs the laser at distances very close to the target where density of the ionized species is high. The term $\left(1 - e^{-h\nu/KT}\right)$ (in Equation 2.5) represents the losses due to stimulated emission. This loss term is dependent on the plasma temperature and also the laser wavelength. For the KrF excimer laser, λ = 248 nm, the exponential term becomes unity for T << 40,000 K and can be approximated by *hv/KT* for T >> 40,000 K.

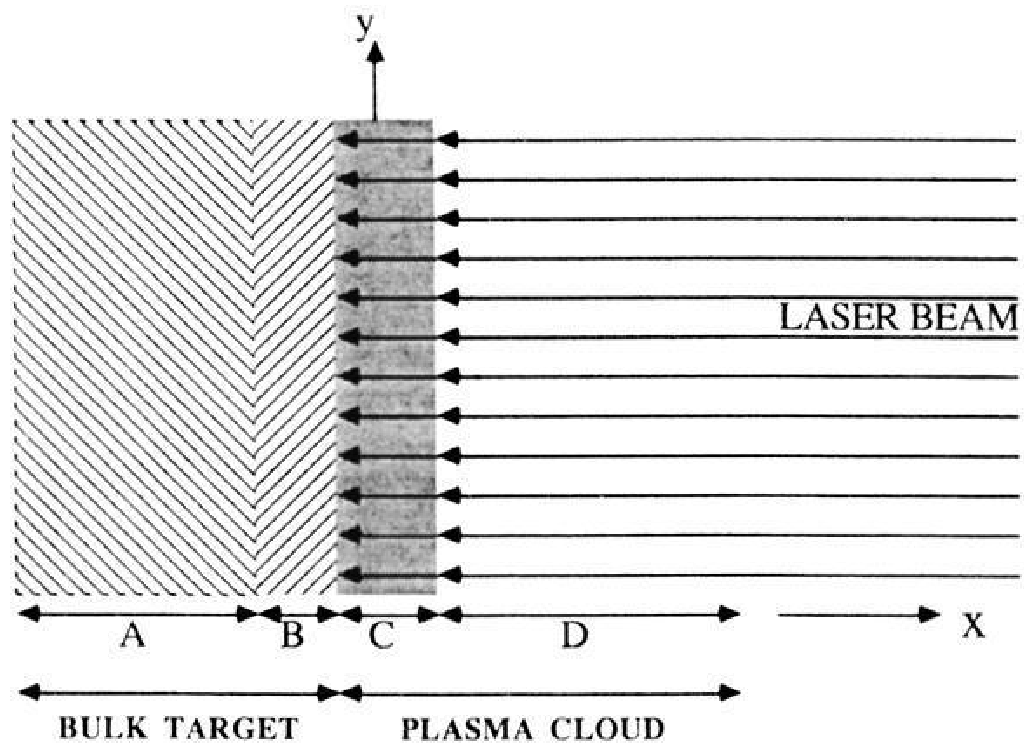

Fig. 2.2 Schematic diagram showing the different phases present during laser irradiation of a target: (A) unaffected target, (B) evaporated target material, (C) dense plasma absorbing laser radiation, and (D) expanding plasma outer edge transparent to the laser beam [38]

The absorption term also shows a $T^{-3/2}$ temperature dependence at high temperatures (T >>40 000 K) and $T^{-0.5}$ dependence at low temperatures (T >> 40,000 K). The frequency variation of the absorption coefficient changes from v^2 to v^3, depending on the value of *hv/KT*. The high expansion velocities of the leading plasma edge, the electron and ion densities decrease very rapidly with time, thus making the plasma transparent to the laser beam at a large distance from the target surface.

As the plasma is constantly augmented at the inner edge by the evaporated target material during the time of the laser pulse, a high density of ions is produced near the surface of the target. The area near the target surface is constantly absorbing the laser radiation during the time interval of the laser pulse, while the outer edge of the plasma is transparent to the laser beam. Based on the observations, a schematic diagram of the laser interaction with the plasma target is shown in Fig. 2.2. The diagram shows that during the incidence of the laser pulse four separate regions can be distinguished as follows:

(A) unaffected bulk target

(B) evaporating target surface

(C) area near the surface absorbing the laser beam

(D) rapidly expanding outer edge which is transparent to the laser

It is reasonable to assume that during the duration of the laser pulse and isothermal temperature is attained near the target surface. A dynamic equilibrium exists

between the plasma absorption and the rapid transfer of thermal energy into kinetic energy. These two mechanisms control the isothermal temperature of the plasma. The rapid expansion of the plasma in vacuum results from large density gradients. The plasma which is absorbing the laser energy can be simulated as a HT-HP gas which is initially confined to a very small dimension and suddenly allowed to expand in vacuum. Because of the large pressure gradients initially present near the outer edge (vacuum), very high expansion velocities are induced at this edge. In the initial stages of the plasma expansion when the particle density is of the order of 10^{19}-10^{20} cm^{-3}, the mean free path of the particles is short, and the plasma behaves as a continuum fluid. The equations of gas dynamics can be applied to simulate its expansion. The density is maximum at the inner edge of the plasma, while the velocity is minimum. When the expansion velocities increase, the acceleration starts to diminish and ultimately becomes zero, and this result in a similar elongated plasma shape [37, 38].

(iii) Adiabatic plasma expansion and deposition of thin films

After the termination of the laser pulse, no particles are evaporated or injected into the inner edge of the plasma; we analyze the adiabatic expansion of this plasma into vacuum after the termination of the laser pulse. Also, the adiabatic expansion of the plasma occurs where the temperature can be related to the dimension of the plasma by the adiabatic thermodynamic equation given by:

$$T\left[X(t)Y(t)Z(t)\right]^{\gamma-1} = const \tag{2.6}$$

where γ is the ratio of the specific heat capacities at constant pressure and volume. The thermal energy is rapidly converted into kinetic energy, with plasma attaining extremely high expansion velocities. In the adiabatic expansion regime, the velocity of the plasma increases due to a decrease in thermal energy of the plasma. As there is no injection of particles in the inner edge of the plasma, the density and pressure gradients can be expressed in a similar form as when taking into account the injection of particles into the plasma. The gas dynamic equation that dictates the expansion of the plasma is the same as in the previous regime expect that the equation of energy and adiabatic equation of state also need to be solved. The adiabatic equation of state is given as,

$$\frac{1}{P}\left(\frac{\partial P}{\partial t} + \bar{v}\cdot\nabla P\right) - \frac{\gamma}{n}\left(\frac{\partial n}{\partial t} + \bar{v}\cdot\nabla n\right) = 0 \tag{2.7}$$

and the equation of temperature is given by,

$$\frac{\partial T}{\partial t} + \bar{v}\cdot\nabla T = (1-\gamma)T\nabla\cdot\bar{v} \tag{2.8}$$

With assuming that there are no spatial variations in the plasma temperature, or $\nabla T = 0$, the initial transverse dimension (Y or Z) are in the millimeters range while in the

perpendicular dimension (X) the values are much smaller and in the micrometer range corresponding to the expansion length in the isothermal regime. The highest velocities are in the direction of the smallest dimension with giving the characteristic elongated plasma shape outward from the target surface [37, 38].

2.2 X-ray diffraction

In order to obtain information about crystalline or amorphous structure in materials, X-ray diffraction (XRD) is an important non-destructive experimental technique. The success of this technique has enabled scientist how to determine crystal structures of metal and alloys, minerals, polymers, organic and inorganic compounds. X-ray diffraction of thin films addresses important properties such as crystal structure, lattice constant, preferred orientation, defects, stress or strain, etc [39]. Basic description of the XRD is explained with two contents such as (i) Lattice planes and Bragg's Law and (ii) Thin film X-ray diffraction.

(i) Lattice planes and Bragg's law

X-rays primarily interact with electrons in atoms. When x-ray photons collide with electrons, some photons from the incident beam will be deflected away from the direction where they original travel, much like billiard balls bouncing off one another. If the wavelength of these scattered x-rays did not change (i.e. x-ray photons did not lose

any energy), the process is called elastic scattering (Thompson Scattering) in that only momentum has been transferred in the scattering process. These are the x-rays that we measure in diffraction experiments, as the scattered x-rays carry information about the electron distribution in materials. On the other hand, In the inelastic scattering process (Compton Scattering), x-rays transfer some of their energy to the electrons and the scattered x-rays will have different wavelength than the incident x-rays. Diffracted waves from different atoms can interfere with each other and the resultant intensity distribution is strongly modulated by this interaction. If the atoms are arranged in a periodic fashion, as in crystals, the diffracted waves will consist of sharp interference maxima (peaks) with the same symmetry as in the distribution of atoms. Measuring the diffraction pattern therefore allows us to deduce the distribution of atoms in a material. The peaks in x-ray diffraction patterns are directly related to the atomic distances. For example, consider an incident x-ray beam interacting with the atoms arranged in a periodic manner (2 dimensions) as shown in Fig. 2.3. The atoms, represented as green spheres in the graph, can be viewed as forming different sets of planes in the crystal (colored lines in graph on left). For a given set of lattice plane with an inter-plane distance of d, the condition for a diffraction (peak) to occur can be written as follows:

$$2d \sin\theta = n\lambda \tag{2.9}$$

Equation 2.9 is known as the Bragg's law with variables, such as the wavelength

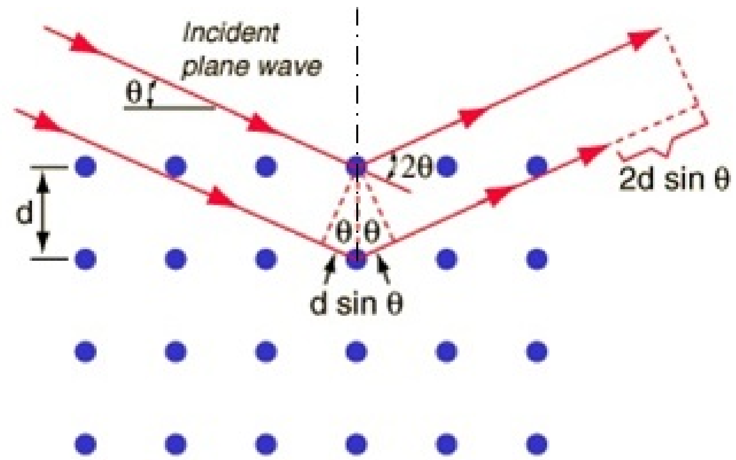

Fig. 2.3 Diffraction for a set of planes with inter-plane distance d which is conditioned to Bragg's Law

of the x-ray (λ), the scattering angle (θ), and an integer number (n) representing the order of the diffraction peak. The Bragg's Law is one of most important laws used for interpreting xray diffraction data. The single, critical, thing that Bragg's Law imparts is as follows: scattering from a crystal occurs in all directions. However the scattering is only visible in a finite number of directions that obey the above law, i.e. the path difference between waves scattered by adjacent lattice planes is a multiple of the wavelength of the radiation - the waves are in phase and constructively interfere. It is important to point out that although we have used atoms as scattering points in this example, Bragg's Law applies to scattering centers consisting of any periodic distribution of electron density. In other words, the law holds true if the atoms are replaced by molecules or collections of molecules, such as colloids, polymers, proteins and virus particles.

(ii) Thin film X-ray diffraction

Thin film diffraction refers not to a specific technique but rather a collection of x-ray diffraction techniques used to characterize thin film samples grown on substrates. These materials have important technological applications in microelectronic and optoelectronic devices, where high quality epitaxial films are critical for device performance. Thin film diffraction methods are used as important process development and control tools, as hard X-rays can penetrate through the epitaxial layers and measure the properties of both the film and the substrate. There are several special considerations

for using x-ray diffraction to characterize thin film samples. First, reflection geometry is used for these measurements as the substrates are generally too thick for transmission. Second, high angular resolution is required because the peaks from semiconductor materials are sharp due to very low defect densities in the material. Consequently, multiple bounce crystal monochromators are used to provide a highly collimated x-ray beam for these measurements. The basic x-ray diffraction measurements made on thin film samples include:

- Precise lattice constants measurements derived from 2θ - θ scans, which provide information about lattice mismatch between the film and the substrate and therefore is indicative of strain and stress.
- Rocking curve measurements made by doing a θ scan at a fixed 2θ angle, the width of which is inversely proportionally to the dislocation density in the film and is therefore used as a gauge of the quality of the film.
- Superlattice measurements in multilayered heteroepitaxial structures, which manifest as satellite peaks surrounding the main diffraction peak from the film. Film thickness and quality can be deduced from the data.
- Glancing incidence X-ray reflectivity measurements, which can determine the thickness, roughness, and density of the film This technique does not require crystalline film and works even with amorphous materials.
- Texture measurements to determine the orientation of crystalline grains in a polycrystalline sample.

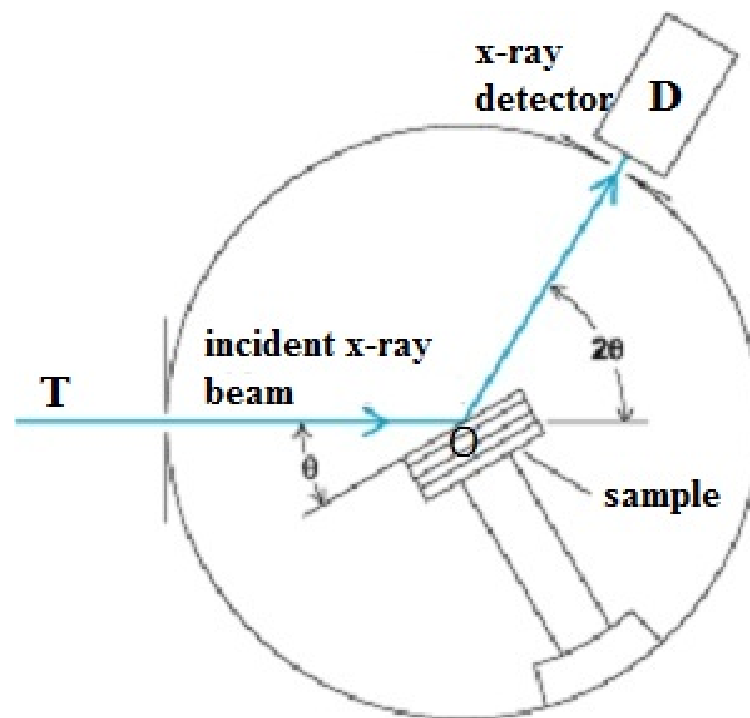

Fig. 2.4 Schematic of an X-ray diffractometer

The essential features of an x-ray spectrometer are shown in Fig. 2.4. It is important to remark that the incident beam and the diffracted beam are always coplanar; and the angle between the diffracted beam and the transmitted beam is always 2θ. Incident X-rays, *T* on a sample may be set at any desired angle to the incident beam by rotation about an axis through *O*, which is the center of the spectrometer circle. *D* is the detector that measures the intensity of the diffracted x-rays; the sample can be rotated about *O* and set at any desired angular position. Thus, by measuring the peak positions, one can determine the shape and size of the unit cell, and one can determine the positions of atoms within the unit cell by measuring the intensities of the diffracted beams. Conversely, if the shape and size of the unit cell of the crystal are known, we can determine the positions of all the possible lines of the film [39-41].

2.3 Transmission electron microscopy

Transmission electron microscopy (TEM) is a microscopy technique, which uses a beam of electrons transmitted through an ultra thin specimen and the beam interacts with the specimen as it passes through. An image is formed from the interaction of the electrons transmitted through the specimen; the image is magnified and focused onto an imaging device. TEM has a resolution and magnification capabilities that are over a thousand times beyond that offered by the light microscope. Its basic operation is similar as the light microscope but uses electrons instead of light.

(i) Resolution and magnification

Usually referred as the resolving power, which can be defined as the closest spacing of two points which can clearly be seen through the microscope to be distinguished as separate entities. Notice that this is not the necessarily the same as the smallest point which can be seen with the microscope, which often is smaller than the resolution limit. Even if all the lenses of the microscope were perfect and introduced no distortions into the image, the resolution would nevertheless be limited by a diffraction effect. Inevitable in any microscope the light must pass through a series of restricted openings, the lenses themselves or the apertures. Whenever light passes through an aperture, diffraction occurs so that a parallel beam of light (seen as an spot) is transformed into a series of cones, which are seen as circles and are known as Airy rings. For light of a given wavelength the diameter of the central spot is inversely proportional to the diameter of the aperture from which the diffraction is occurring. Consequently the smaller the aperture, the larger is the central spot of the Airy disc. For having clearly visible Airy disc very small apertures are used, but the same effect occurs from relatively large apertures in light microscopes. The diffraction effect limits the resolution of a microscope because the light from a very small point in the object suffers diffraction, particularly by the objective aperture, and even an infinitely small point becomes a small Airy disc in the image. In order to make this disc as small as possible, the aperture must be as large as is feasible. Considering the resolution of the microscope in more detail, starting with the Airy disc, Fig. 2.5 shows the variation of the light

intensity across the series of rings which make up the disc. The central spot is very much more intense than any other ring and in fact contains 84% of all the light intensity. Consequently for many purposes the rings can be ignored and we can assume that all the light falls in a spot of diameter d_1, where $d_1 \alpha 1/(\text{aperture diameter})$. Rayleigh proposed a criterion that works well in most cases and has been used extensively ever since; when the maximum of intensity of an Airy disc coincides with the first minimum of the second, then the two points can be distinguished. Figure 2.6 illustrates that the resolution limit is $d_1/2$. Microscopes apertures are normally referred to in terms of the semi-angle, α, which subtends to the specimen. Then, it is possible to derive from diffraction theory an expression for the resolution as follows:

$$\gamma = \frac{0.61\lambda}{n \sin \alpha} \tag{2.10}$$

where λ is the wavelength of the radiation, n is the refractive index of the medium between the object and the lenses, and α is the semi-angle of collection of the magnifying lens. The product, *nsinα* is called the numerical aperture (NA).

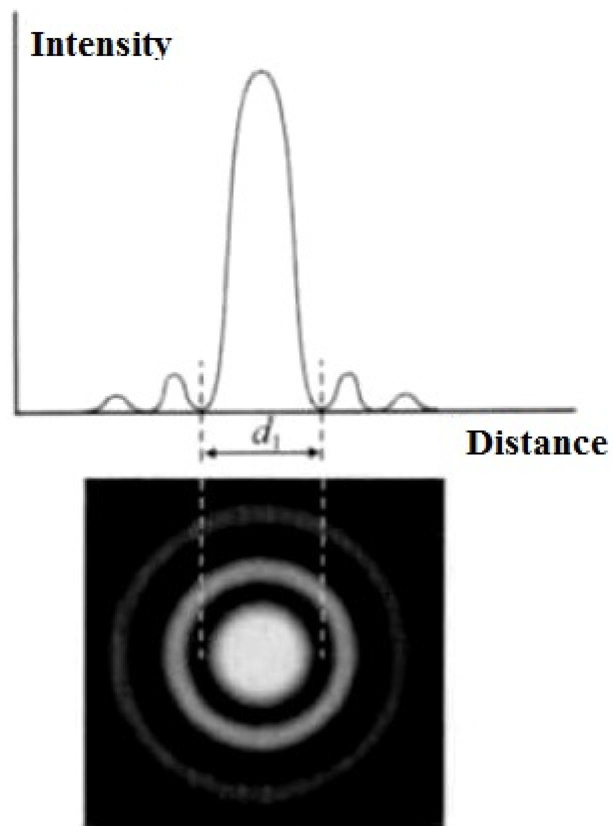

Fig. 2.5 The variation of light intensity across a set of Airy rings. Most of the intensity (84%) lies within the first ring that is within a spot of diameter d_1 [42].

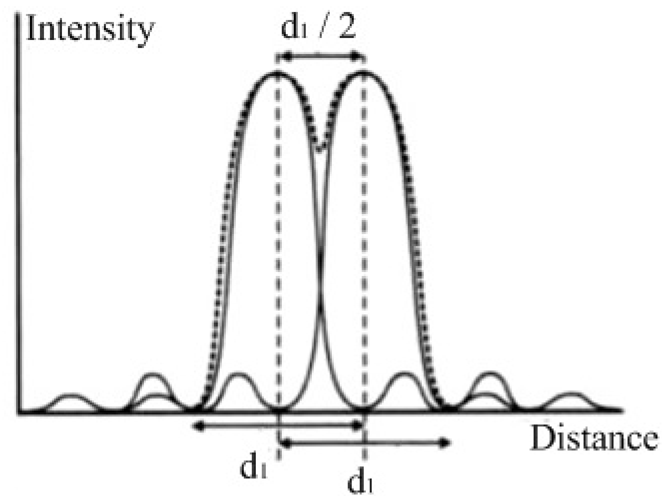

Fig. 2.6 The intensity of the Airy rings from two neighboring pinholes. The intensity distributions from each of the pinholes separately are shown as solid lines; the combined profile from the two pinholes acting together is shown dotted. At the Rayleigh resolution limit, as shown here, the maximum intensity from one pinhole coincides with the first minimum from the other giving a resolution limit of $d_1/2$ [42].

Besides forming images with high resolution, the lenses of an electron microscope are able to magnify these images. Magnification refers to the degree of enlargement of the diameter of a final image compared to the original. In practice, magnification equals a distance measured between two points on an image divided by the distance measured between these same two points on the original object, or

$$Mag = \frac{d(image)}{d(object)} \tag{2.11}$$

Consequently, if the image distance between two points measures 25.5 mm while the distance between these same two points on the object measures 5 mm, then the magnification is 5.1. There are at least three magnifying lenses in an electron microscope: the objective, intermediate, and projector lenses. The final magnification is calculated as the product of the individual magnifying powers of all of the lenses in the system [42].

(ii) High resolution

Most of the conditions used to achieve high resolution in the electron microscope are the opposite conditions discussed above for the high contrast mode. Since contrast will be lacking in these specimens, efforts should be made to boost contrast using appropriate specimen preparation and darkroom techniques, as described in the previous

section. The following describes some considerations for obtaining High Resolution images:

- The objective lens should be adjusted to give the shortest possible focal length and the proper specimen holders used. In some systems, this is simply a matter of pressing a single button, whereas, in certain microscopes several lens currents must be changed concomitantly. Perhaps it may even be necessary to insert a different polepiece in the objective lens.
- Adjustments to the gun, such as the use of higher accelerating voltages, will result in higher resolution for the reasons already mentioned in the discussion on high contrast. Chromatic aberration may be further lessened by using field emission guns since the energy spread of electrons generated from such guns is considerably narrower. (The energy spread for tungsten = 2 eV while field emission = 0.2–0.5 eV.) In an electron microscope equipped with a conventional gun, a pointed tungsten filament will generate a more coherent, point source of electrons with better resolution capabilities.
- Use apertures of appropriate size. For most specimens, larger objective lens apertures should be used to minimize diffraction effects. If contrast is too low due to the larger objective aperture, smaller apertures may be used but resolution will be diminished. In addition, they must be kept clean since dirt will have a more pronounced effect on astigmatism. Small condenser lens apertures will diminish spherical aberration, but this will be at the expense of overall

illumination. The illumination levels may be improved by altering the bias to effect greater gun emissions; however, this may thermally damage the specimen.

- Specimen preparation techniques may also enhance the resolution capability. Extremely thin sections, for instance, will diminish chromatic aberration. Whenever possible, no supporting substrates should be used on the grid. To achieve adequate support, this may require the use of holey films with a larger than normal number of holes. The areas viewed are limited to those over the holes.
- Miscellaneous conditions such as shorter viewing and exposure times will minimize contamination, drift, and specimen damage, and help to preserve fine structural details. Some of the newest microscopes have special accessories for minimal electron dose observation of the specimen and may even utilize electronic image intensifiers to enhance the brightness and contrast of the image. Anticontaminators over the diffusion pumps and specimen area will diminish contamination and resolution loss. High magnifications will be necessary, so careful adjustment of the illuminating system is important. It may take nearly an hour for the eyes to totally adapt to the low light levels, and this adaption will be lost if one must leave the microscope room. Alignment must be well done and stigmation must be checked periodically during the viewing session. The circuitry of the microscope should be stabilized by allowing the lens currents and high voltage to warm up for 1 to 2 hours before use. Bent specimen grids should be avoided since they may place the specimen in an improper focal plane for

optimum resolution. In addition, they prevent accurate magnification determination and are more prone to drift since the support films are often detached.

(iii) Electron diffraction

A TEM can generate a diffraction pattern from a specimen. This is because the diffraction pattern is always present in the back focal plane of the objective lens. From the ray diagram shown in Fig. 2.7, it is apparent that the forward scattered diffracted electrons come to a focal point (this is the back focal plane of the objective lens) but are excluded by the objective aperture. As will be shown, one of the operational requirements to obtain diffraction patterns may involve removal of the objective aperture or the use of a larger aperture. Although diffraction patterns are generated by all specimens, some patterns have more information about the nature of the specimen than do others. For instance, specimens with randomly or non periodically oriented atoms generate a diffuse electron diffraction pattern that simply confirms that the atoms of the specimen are not arranged in a repeating or periodic manner. By contrast, whenever the specimen or parts of the specimen consist of molecules or atoms with a repeating periodicity (as in a crystalline lattice), then a diffraction pattern is formed that may be useful in the identification of the crystal or molecule. Electron diffraction may give the spacing of the crystalline lattice and (since various crystals have unique lattice spacings and diffraction patterns) the chemical identity of the crystal. On the other hand, electron

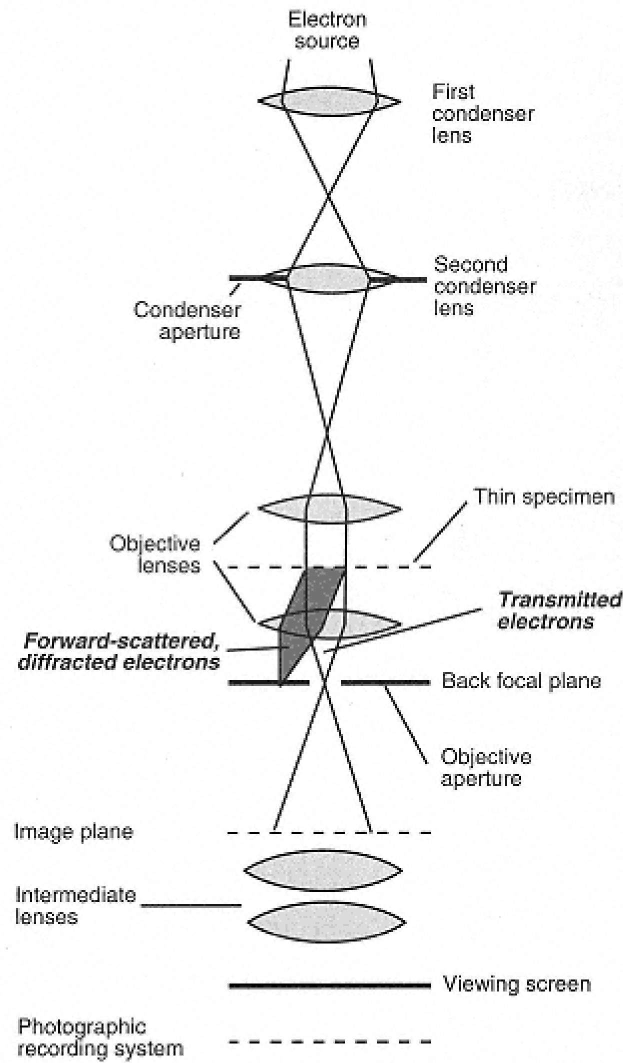

Fig. 2.7. Schematic of lenses in a transmission electron microscope. Note the dashed line indicating one group of diffracted electrons that converge in the back focal plane of the objective lens [43].

diffraction cannot be used to determine the quantity of a particular chemical that has been identified.

If a beam of electrons strikes a crystalline structure at an appropriate angle (so called Bragg angle) the electrons will be diffracted or "reflected" from the lattice planes. The reflection follows Bragg's law of diffraction. Some of the electrons that enter the lattice at the proper angle will be reflected by the various lattice planes in the same direction and at the same angle to come to focus in the back focal plane. This generates the diffraction pattern. In the case of an amorphous specimen, the electron beam that enters the specimen is diffracted in multiple directions and at various angles so that the electrons are unable to converge into a discrete spot and form a diffuse ring pattern instead. With a crystalline specimen, in order to obtain the proper Bragg angle, it is necessary to orient the specimen very precisely by tilting and rotating it relative to the electron beam until the diffraction pattern is obtained.

2.4 Transient thermo-reflectance method

The TTR measurement for through-plane thermal conductivity of thin film was performed using a new compact TTR system developed in the NETSL at SMU. The basic principle of the transient thermal reflectance method is to heat a sample by laser irradiation and probe the changes in the surface reflectivity of the heated material. The source of energy in the TTR method is normally provided by a pulsed laser with short pulse duration. During each pulse, a given volume below the sample surface heats up

due to the absorbed laser light energy. The depth of the volumetric heating is determined by the optical penetration depth, which is a function of laser wavelength and surface material properties. After each laser pulse, the sample cools down to the initial ambient temperature. During this process, a probing CW laser light reflected from the sample surface at the heating spot center is collected on a photodetector (1 ns maximum rise time) that reads the instantaneous surface reflectivity, as shown in Fig.. 2.8.

The TTR system uses the fact that the relative change in the temperature of the surface material is linearly proportional with the relative change in the reflectivity within a wide but finite temperature range:

$$\frac{\Delta T}{T} = \frac{\Delta R}{R} \tag{2.11}$$

where T is the temperature and R is the reflectivity of the materials. The changes in surface reflectivity, are then recorded by an oscilloscope (at rates of up to 5 GS). The above-mentioned principle has been experimentally and analytically proven by Qiu and Tien [12, 13], Burzo *et al.*[11, 14, 15] and Komarov *et al.*[15].

The result of the experiment is a transient normalized temperature response, which represents the overall heat transfer behavior of the layers of materials including the unknown material under test. To extract the thermal conductivity from the recorded temperature response, an identical mathematical representation of the corresponding

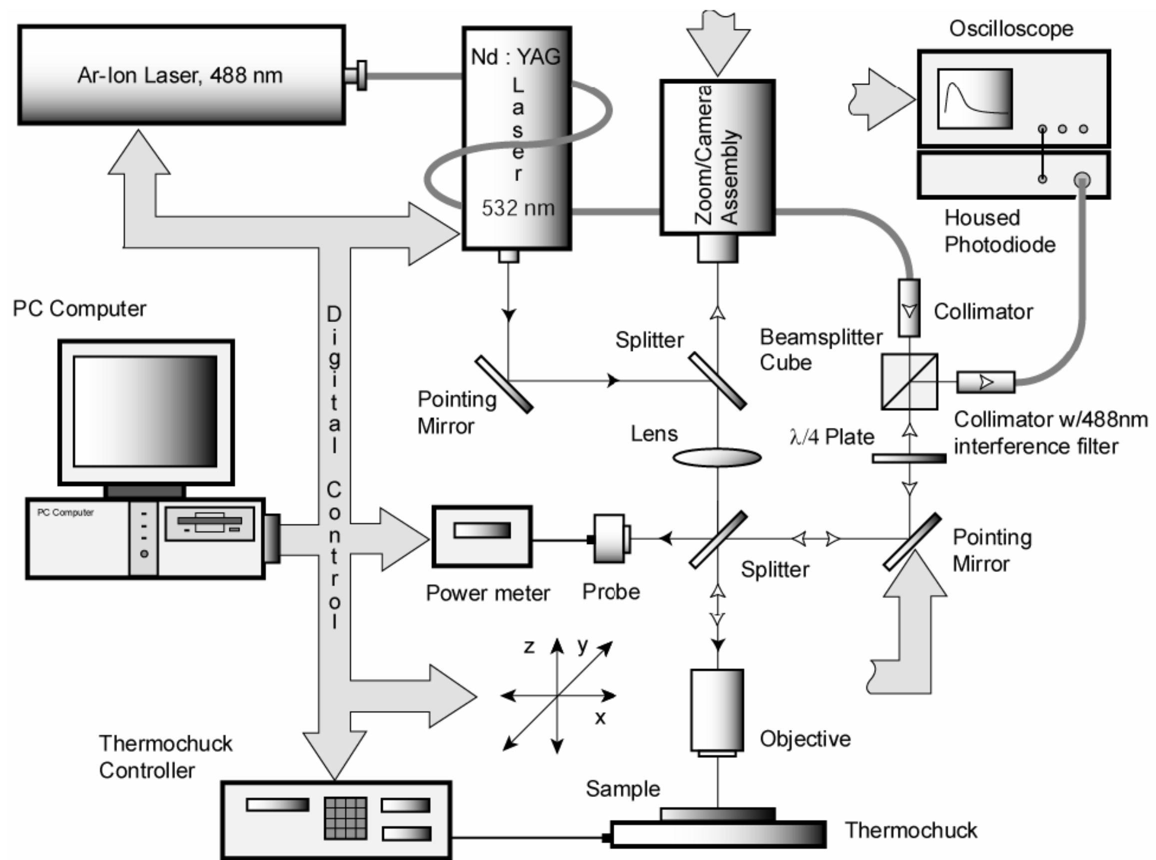

Fig. 2.8 Schematic of the Transient Thermo-Reflectance (TTR) system in NETSL at SMU by Burzo *et al*.[44]

physical measurement problem is solved numerically with guessed thermal properties with the intention of matching the experimental and numerical transient normalized temperature responses. A mathematical optimization technique makes it possible to systematically vary the desired unknown properties and compare each resulting numerically-obtained response to the reference experimental data until the error between them is minimized in the RMS sense. The final numerical solution hence yields the desired unknown parameters, which represent the best fit to the actual thermal properties of the physical sample.

By using a two-parameter optimization technique, the method described in this work yields not only the thermal conductivity of the material under test but also the interface resistance between this material and the absorption layer on top of it. The transient heat transfer in the TTR method can be described by the use of the heat equation, as follows:

$$\rho C_p \left(\frac{\partial T}{\partial t} \right) = \nabla (K \nabla T) + \dot{Q}_{ab} \tag{2.12}$$

where ρ is the mass density of the material, C_p is its specific heat, t is the time, K is its thermal conductivity, and $\dot{Q}_{ab}$ is the heat source created by absorption of the laser light energy. The TTR system developed by the NETSL was designed to perform through-plane only or both through-plane and in-plane thermal properties measurements. In order to be able to measure both the through-plane and in-plane thermal properties the two-

dimensional heat transfer is used. In this case, the heat transfer inside the sample under test is governed by the 2D heat equation in polar coordinates and can be written as follows:

$$\left(\frac{\partial T}{\partial t}\right) = \alpha(T)\left(\frac{\partial^2 T}{\partial r^2} + \frac{1}{r}\frac{\partial T}{\partial r} + \frac{\partial^2 T}{\partial z^2}\right) + \frac{1}{\rho C_p}\dot{Q}(r,z,t) \tag{2.13}$$

where r and z are dimensionless coordinates and α is the thermal diffusivity of the material, which is $\alpha = K/(\rho C_p)$. The heat source, $\dot{Q}$, was introduced as follows:

$$\dot{Q}_{(r,z,t)} = I(t)(1-R)\gamma e^{-\gamma z} \tag{2.14}$$

where γ is the absorption coefficient of the top layer, and $I(t)$ is a Gaussian temporal distribution as follows:

$$I(t) = \frac{2F}{\tau\sqrt{\pi}} e^{-4\left(\frac{t-t_0}{\tau}\right)^2} \tag{2.15}$$

where F is the fluence of laser irradiation, τ is the duration of the heating laser pulse which is 6.1 ns, and t_0 = 7 ns is the time at which the intensity reaches its maximum value.

In this study, the one-dimensional TTR measuring approach can be used, since the purpose of this study was to measure the through-plane thermal conductivity of films. It is worth mentioning that the dimension of the probing spot is close to two orders of magnitude smaller than the heating laser spot, thus assuring the applicability of the one-dimensional approach. As a result, the heated sample under test can be treated as a semi-infinite solid for the one-dimensional problem. The diameter of the heated spot (YAG Laser) is 185 µm, while the probing spot is around 2.5 µm, which is small enough to make $\frac{\partial T}{\partial r} \approx 0$ in the probing spot area. Thus, the one-dimensional heat equation is induced from the 2D Eq. (2.13) as follows:

$$\left(\frac{\partial T}{\partial t}\right) = \alpha\left(\frac{\partial^2 T}{\partial z^2}\right) + \frac{1}{\rho C_p}\dot{Q}_{ab}(z,t) \tag{2.16}$$

The first boundary condition is an adiabatic boundary condition at the top of the sample as follows:

$$\left(\frac{\partial T}{\partial t}\right) = 0 \text{, at } z = 0 \tag{2.17}$$

since the time scale of the TTR is in the nanosecond range, natural convection and conduction from the sample to the surrounding medium (air) can be neglected.

The second boundary condition is an isothermal boundary condition at the bottom of the sample as follows:

$$T = T_{chuck}\text{ , at } z = \infty \tag{2.18}$$

because the sample is located on a thermo-chuck that keeps the temperature constant at T_{chuck}. Initially, since the materials are at ambient temperature, the initial condition is written as follows:

$$T = T_{ambient}\text{ , at } t = 0 \tag{2.19}$$

During the heating and cooling process, the instantaneous surface reflectivity is acquired by the probing CW laser light reflected from the sample surface at the center of the heated spot, and then the thermal diffusivity of the material is extracted by solving the one-dimensional inverse heat Eq. (2.16) based on Eq. (2.11) as shown by Burzo et al.[45]. This was accomplished by first numerically simulating the transient heating caused by the laser pulse and then fitting the experimental results with the computed data in the TTR system.

2.5 Measurement uncertainty of TTR method

The estimation of uncertainty values was based on the analysis developed by Kline and McClintock [46] with a confidence level of 95% (or 20:1 odds) or 90%. The method was based on the uncertainties in the primary measurements, such as the thickness measurements of the films and the Au layer, and then, the uncertainty for the thickness of each layer was considered for the uncertainty of thermal conductivity in the TTR measurement.

In the TTR measurements, M.G. Burzo [47] presented an uncertainty analysis for numerical procedures and experimental work because the uncertainties caused by the numerical procedures are attributed to the uncertainties in the process of matching the experimental temperature transient response with the numerical solution of the heat equation.

Total uncertainty, W_k, for thermal conductivity measurement was presented as follows:

$$W_k = W_{total} = \frac{W_\theta}{\Omega_K} \tag{2.20}$$

where W_θ is the uncertainty in the transient normalized surface temperature response (θ) and Ω_K is responsivity for thermal conductivity K from the responsivity of the transient temperature response as follows:

$$W_{\theta} = \sqrt{(W_{num})^2 + (W_{\exp})^2} \quad (2.21)$$

$$\Omega_V = V \frac{\partial \theta}{\partial V} \quad (2.22)$$

where V is one of the following variables: thermal conductivity K, thickness of the layer h, imaginary part of the refractive index of the top layer k, real part of the refractive index of the top layer n, or the thermal capacitance ρC_p.

Thus, Ω_K is calculated numerically from Eq. (2.22), and the other responsivities of the temperature response for the variables ($\Omega_{\rho Cp}$ and Ω_h) are also calculated from the Eq. (2.22). Thus, the numerically based uncertainties W_{num} and experimentally based uncertainty W_{exp} are estimated for W_{θ}.

The uncertainty of the matching procedure W_{num} was estimated by calculating the standard deviation between the experimental and numerical transient temperature responses in the effective time range in each TTR measurement. The experimental uncertainty W_{exp} is calculated as follows:

$$W_{\exp} = \sqrt{(W_{TTR})^2 + (\Omega_h W_h)^2 + (\Omega_K W_K)^2 + \left(\Omega_{\rho C_p} W_{\rho C_p}\right)^2 + (\Omega_n W_n)^2 + (\Omega_k W_k)^2} \quad (2.23)$$

Each sample was tested using the TTR method in at least three different locations within 1×3 mm on the sample. At each location, the heating laser was pulsed 1000 times for samples. The standard deviation of the obtained transient responses versus time was calculated for the different locations in a sample. Thus, the uncertainty W_{TTR} was estimated from the time-averaged standard deviation.

2.6 Four-point probe method

The electrical resistivity of thin films is measured by the four-point probe (FPP) technique. The four-point probe technique is a good method for measuring thin films resistivity and its main advantage is of getting an absolute measurement without recourse to calibrated standards. Moreover, it is simpler compared to an easy to do two point probe measurement where the interpretation of the data is far difficult. The explanation of such a difficulty is because in a two-point probe arrangement, each probe serves as a current and a voltage probe. Then a total resistance RT between the probes is given by Eq (2.24) with its major contributors R_p, R_c, R_{sp} and R_f , where R_c and R_{sp} are assumed to be identical for the two contacts. The contact resistance (R_c) is the results from the mechanical metal probe contacting the thin film, the spreading resistance (R_{sp}) is the resistance encountered by the current when it flows from the small probe to the thin film and thin film to the probe. The value of R_p can be measured by shorting the two probes but the values of R_c and R_{sp} can't be measured or calculated for a mechanical

probe, so the resistivity can't be extracted from the total resistance obtained by two point probe measurements.

$$R_T = \frac{V}{I} = 2R_p + 2R_c + 2R_{sp} + R_f \quad (2.24)$$

R_p: probe resistance

R_c: contact resistance at metal probe/thin film contact

R_{sp}: spreading resistance under each probe

R_f: the thin film resistance

The four-point probe technique is an electrical impedance measuring technique that uses separate pairs of current-carrying and voltage-sensing electrodes to make more accurate measurements than traditional two-point probe method. Two probes carry the electrical current and the other two probes measure the voltage difference between them. Four-point probe method is also known as Kelvin method, after William Thomson, Lord Kelvin, who invented the Kelvin bridge in 1861 to measure very low resistances. The four-point probe technique was adapted for the semiconductor industry in 1954 by Valdes[48]. The probes generally are collinear, in line, and with equal space between probes as shown in Fig. 2.9, but other alternative configurations are possible. The use of four probes presents an important advantage over two probes measurements.

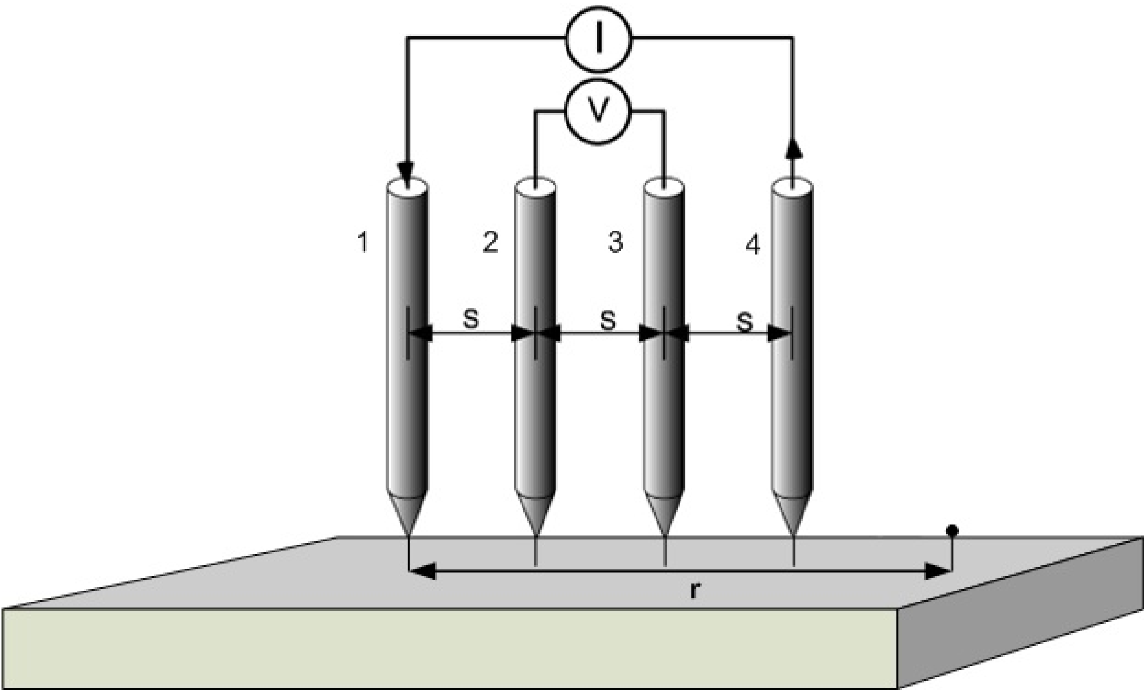

Fig. 2.9 A collinear four-point probe array

Although the two probes carrying current still have contact and spreading resistance, the same is not true for the other two probes, which draws no current at all or have high impedance that draws very little current. The parasitic resistances R_p, R_c, and R_{sp} in the two voltage probes are negligible small because of the very small current flowing through them. These four-point contact measurement techniques are known as the Kelvin techniques.

In order to derive the four-point probe resistivity expression the following considerations are taking into account: (a) a current I is entering through probe 1 and leaving through probe 4 as shown in Fig. 2.9, (b) the potential V at a distance r from an electrode carrying a current I in a material of resistivity is given by the relationship

$$V = \frac{\rho I}{2\pi r} \tag{2.25}$$

For probes resting in a semi-infinite medium as in Fig. 2.9 with current entering through probe 1 and leaving probe 4, the voltage V_0 measured with respect to a zero reference potential is,

$$V_0 = \frac{\rho I}{2\pi}\left(\frac{1}{r_1} - \frac{1}{r_2}\right) \tag{2.26}$$

where r1 and r4 are the distances from probes 1 and 4, respectively. The minus sign accounts for the current leaving probe 4. For most four-point probes the space, s and the voltage between probes 2 and 3 is given by the expression:

$$V = V_2 - V_3 = \frac{\rho I}{2\pi s} \quad (2.27)$$

and the resistivity given by,

$$\rho = 2\pi s\left(\frac{V}{I}\right) \quad (2.28)$$

Thin film samples are not semi-infinite in either the lateral or the vertical dimensions; therefore, the mentioned resistivity equation must be corrected for finite geometries with a factor F. The factor F must account for correcting location of the probe near samples edges, sample thickness, sample diameter, probe placement and sample temperature.

CHAPTER III

EPITAXIAL TaN/TiN NANOLAYERS WITH UNIQUE ELECTRICAL AND RADIATION TOLERANCE PROPERTIES

3.1 Overview

A multifunctional ceramic coating serves as effective diffusion barrier. The effect of interfaces on materials radiation tolerance properties has been investigated for nanolayered TaN/TiN films with two individual layer thicknesses of 2/16 nm and 5/20 nm prepared by pulsed laser deposition. Evolution of the microstructure and hardness of the multilayer films were examined on the specimens before and after He ion-implantation to a fluence of 4×10^{16} cm^{-2} at 12keV and 50 keV. The nanolayer samples did not show any obvious hardness reduction after ion-irradiation but He bubbles were observed at the interfaces in the TaN/TiN 2/16 nm specimen. The reduced modulus decreased after ion-irradiation. This study indicates that the nanolayer interfaces of TiN and TaN have superior radiation tolerance properties. In this multilayer, the size effect was dominant on resistivity rather than interface effect. Grain size affected on both of epitaxial cubic phase and polycrystalline TaN/TiN, and it increased the resistivity due to grain boundary scattering in the thin thickness regime. The findings are important for a wide range of applications using nitride-based ceramic materials in microelectronic diffusion barrier as well as radiation tolerance materials.

3.2 Introduction

As the microelectronics continue being scaling down to submicron dimensions, it creates a continuous demand for better interconnects and diffusion barriers. The possibility of materials interdiffusion and reaction in multilayer thin film assemblies increases with decreasing device dimensions, because the proximity of layers of different materials and the microstructural defects exist in these layers become important. Diffusion barrier layers can be used to effectively reduce or prevent such materials reactions. Various metal nitrides have been proven to perform extremely well as barriers layers.

The performance of TiN and TaN as diffusion barriers and radiation tolerance materials have recently been studied [49, 50]. Compared with TiN, TaN has higher thermal stability, relatively denser interstitial structure, and thickness advantages that fulfill the requirements for next generation ultra-large-scale integration devices. At the beginning of the 21st century, the rapid growing market needs accelerated the development of integrated circuits (IC) with increasing speed and more functionality. The main goal until these days is to increase devices density per chip, thus requiring a shrinkage of the feature size of every individual device and enhancing the overall metallization scheme to minimize interconnect wire-length distribution [51].

In addition, nitrides are considered to be one of the advanced nuclear fuel forms for waste storage and can act as effective diffusion barriers to minimize fuel-cladding interactions [4, 5]. Ion irradiation-induced amorphization in ceramics has been

previously reported as one primary damage mechanism in ceramics [6]. For the case of homogeneous amorphization, progressive defect accumulation, such as accumulation of point defects, causes amorphization after a critical defect concentration level. This model is usually applied in light-ion irradiation for which separated point defects are dominant. For the case of heterogeneous amorphization, it is a complicated process involving creation of individual collision cascades, overlap of collision cascades, and nucleation and growth of the amorphous domains [6].

In nanocrystalline or nanolayered metallic systems, enhanced radiation tolerance properties have been reported both experimentally and theoretically. For example, microstructural changes caused by helium ion-irradiation in several multilayer systems, including immiscible Cu/Nb [16], Cu/V [7], and miscible Al/Nb [17], and Fe/W [8], have been systematically studied. Certain type of immiscible interfaces, such as Cu/V, could significantly enhance the ion-irradiation tolerance of metallic materials compared with their bulk counterparts. Dramatic reductions of swelling, bubble density, lattice expansion and radiation hardening are observed in Cu/V multilayers, wherein interface act as effective sinks to absorb radiation induced point defects and promote the annihilation of opposite type of defects (Frenkel pairs), and consequently reduce the overall point defect density in the multilayers [7, 8, 16, 18]. In nitride ceramic materials, nanocrystalline TiN coatings [5] have been previously demonstrated with enhanced radiation tolerance, in which grain boundaries act as effective sinks for defect accumulation and annihilation. Reducing grain sizes increases the areas of grain

boundaries, which are defect sinks, and thus leads to significantly enhanced radiation tolerance.

In this work, we investigated the interfacial effects on the ion-irradiation tolerance of nitride ceramics by synthesizing a series of epitaxial cubic TaN/TiN nanolayer with two different layer thicknesses, i.e., 2/16 nm and 5/20 nm, for 12 keV and 50 keV He ion implantation. In addition, by varying the nanolayer thickness and the number of interface, electrical resistivity measurements were conducted on epitaxial cubic phase and polycrystalline TaN/TiN nanolayers to explore the defect nature at nanolayer interfaces.

3.3 Experimental details

TaN/TiN multilayer thin films were deposited by pulsed laser deposition technique in an ultrahigh vacuum chamber with a KrF excimer laser (Lambda Physik Compex Pro 205, λ = 248 nm, 10 Hz). Laser beam was focused to obtain an energy density of approximately 7 $J \cdot cm^{-2}$ at 45° angle of incidence. TaN and TiN targets were hot-pressed stoichiometric TaN and TiN obtained from Plasma Materials Inc. The multilayer films were deposited at a typical growth rate of 0.4 Å/pulse for TaN layer and for 0.6 Å/pulse for TiN layer with a base pressure of approximately 10^{-7} Torr and deposition temperature of 700 °C. Prior to film deposition, the Si (001) substrates were cleaned in acetone and methanol followed by etching in hydrofluoric acid to remove native silicon oxide layer on surface.

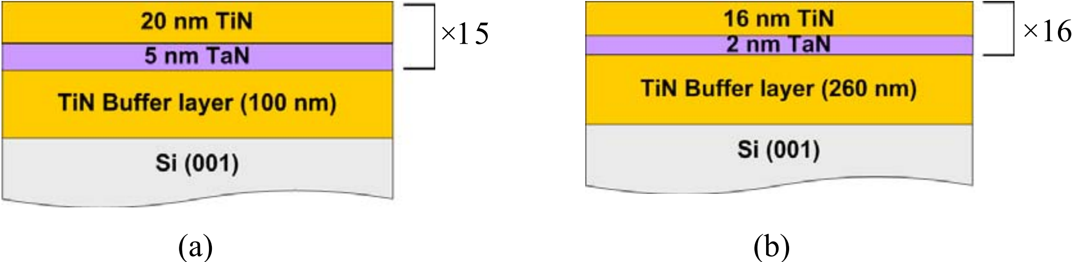

Fig. 3.1 Schematic of prepared TiN/TaN nanolayer film with different nanolayer thickness for radiation tolerance experiment

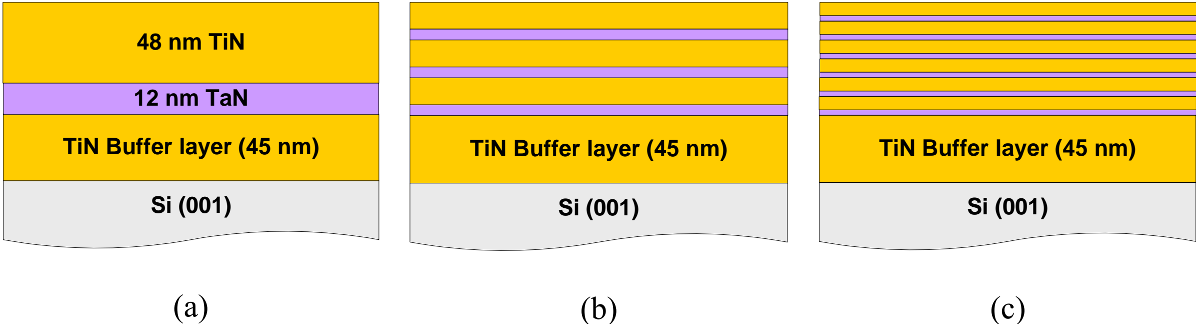

Fig. 3.2 Schematic of prepared TiN/TaN nanolayer film with different number of interface and nanolayer thickness for electrical resistivity measurement

A computer-controlled 6-target exchangeable target carousel was used to precisely control the growth of nanolayer samples. A TiN buffer layer was first deposited on silicon substrates to grow epitaxial metastable cubic TaN/TiN nanolayers. The two set of TaN/TiN nanolayer films were deposited with individual layer thickness h: one set consists of 20 nm thick TiN and 5 nm thick TaN nanolayers (as total 500 nm with buffer layer) and consist of 15 nm thick TiN and 2 nm thick TaN (as total 530 nm with buffer layer) as shown in Fig. 3.1. This set of samples is to study the interface effects on radiation tolerance properties. The other set of samples consists of TaN/TiN multilayer with various numbers of interfaces for size and interface effect on electrical resistivity as shown in Fig. 3.2. The radiation test samples were then irradiated at room temperature with He ions to a high fluence of 4×10^{16} cm^{-2} at 50 keV for TaN/TiN (20/5 nm) and at 12 keV for TaN/TiN (16/2 nm). Microstructural evolution of the irradiated films was characterized by cross-section transmission electron microscopy (XTEM) and high resolution TEM (HRTEM) using a JEOL-3000F and JEOL 2010 analytical electron microscope with resolution of 0.18 nm and 0.23nm, respectively.

Hardness of all films was measured with a Hysitron Tribo-nanoindenter. The measurement was performed using a standard Berkovich diamond tip under a constant load mode with load varied from 2000 to 3200 μN. In order to minimize any substrate effect on hardness measurements, the penetration depth was controlled to be approximately 20 % (~100 nm) of total film thickness. Hardness and elastic modulus was calculated based on an average of at least sixteen indentation experiments per indentation depth. A plateau is typically observed in the hardness vs. indentation depth

plot and the plateau value is chosen as the average hardness of the films. Electrical resistivity of the TaN/TiN films with various numbers of interfaces were measured and compared

3.4 Results and discussion

The damage profiles in single layer TiN and TaN caused by He ion irradiation were simulated at 12 keV and 50 keV with the fluence of 4.0×10^{16} cm^{-2} by using SRIM 2008 [52]. The peak damage depth in TiN and TaN for 12 keV H^+ wih fluence of 4.0×10^{16} cm^{-2} are 45 nm and 25 nm, respectively, as shown in Fig. 3.3. When the energy increases to 50 keV, the damage depths are 190 nm and 120 nm for TiN and TaN, respectively, as shown in Fig. 3.4. Comparing the multilayer thickness, the damage peaks are expected to be located within the stack of TaN/TiN nanolayer. Thus, the interface effect on radiation tolerance is studied in the TaN/TiN multilayer region, not in the TiN buffer layer.

As-deposited and ion-irradiated specimens were examined by XTEM, STEM, and EDX to study the microstructure evolution due to ion irradiation. Figure 3.5 shows the low magnification XTEM images of 5/20 nm TaN/TiN multilayered film before ion-irradiation. In the multilayer region, the dark contrast is TaN and relatively bright contrast is TiN with ~100 nm thick TiN buffer layer on Si(001) substrate.

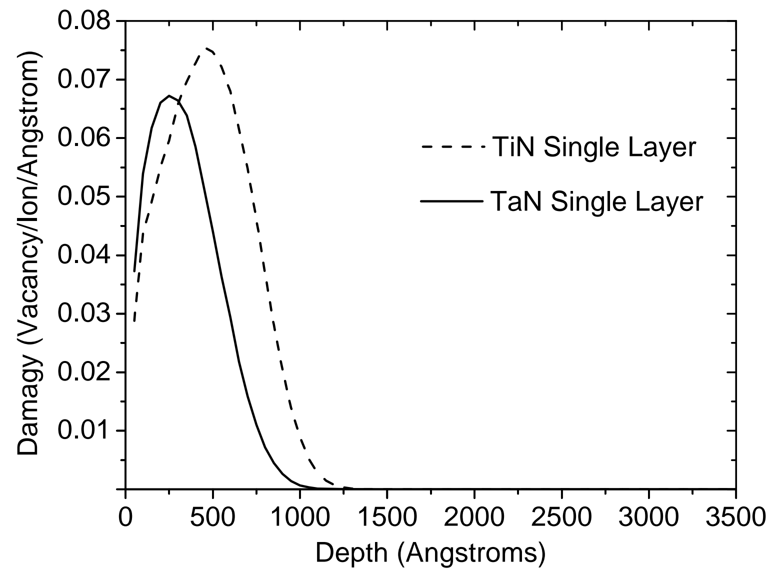

Fig. 3.3 SRIM calculation: comparison of damage profile for TiN/TaN 16/2 nm multilayer, TiN, and TaN single layers by 12 keV He^+ ion implantation

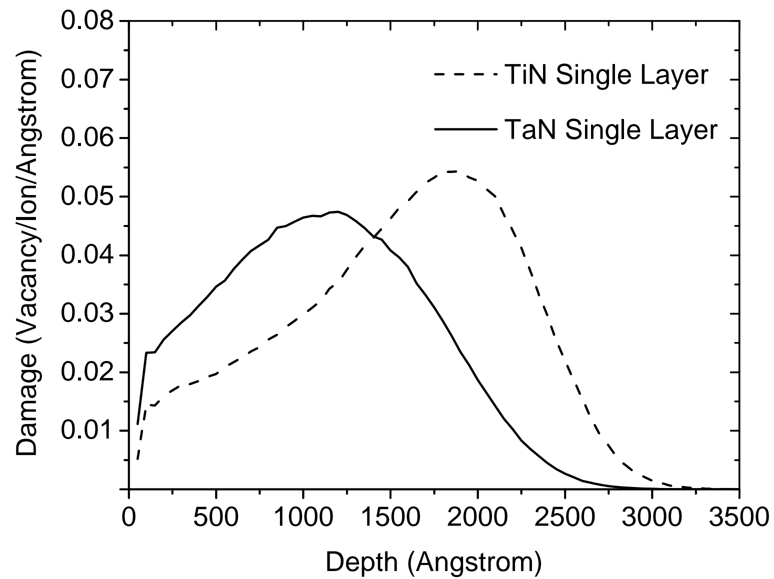

Fig. 3.4 SRIM calculation: comparison of damage profile for TiN/TaN 20/5 nm multilayer, TiN, and TaN single layers by 50 KeV He^+ ion implantation

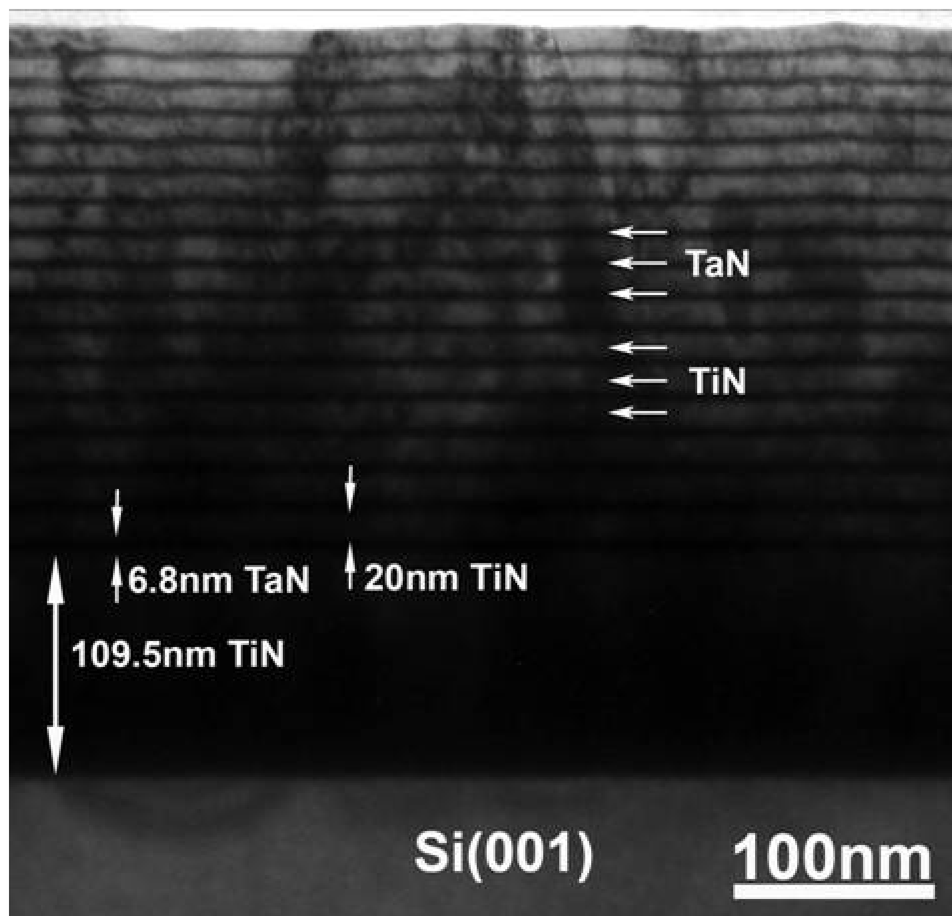

Fig. 3.5 TEM image of TiN/TaN (20/5nm) multilayer as-deposited

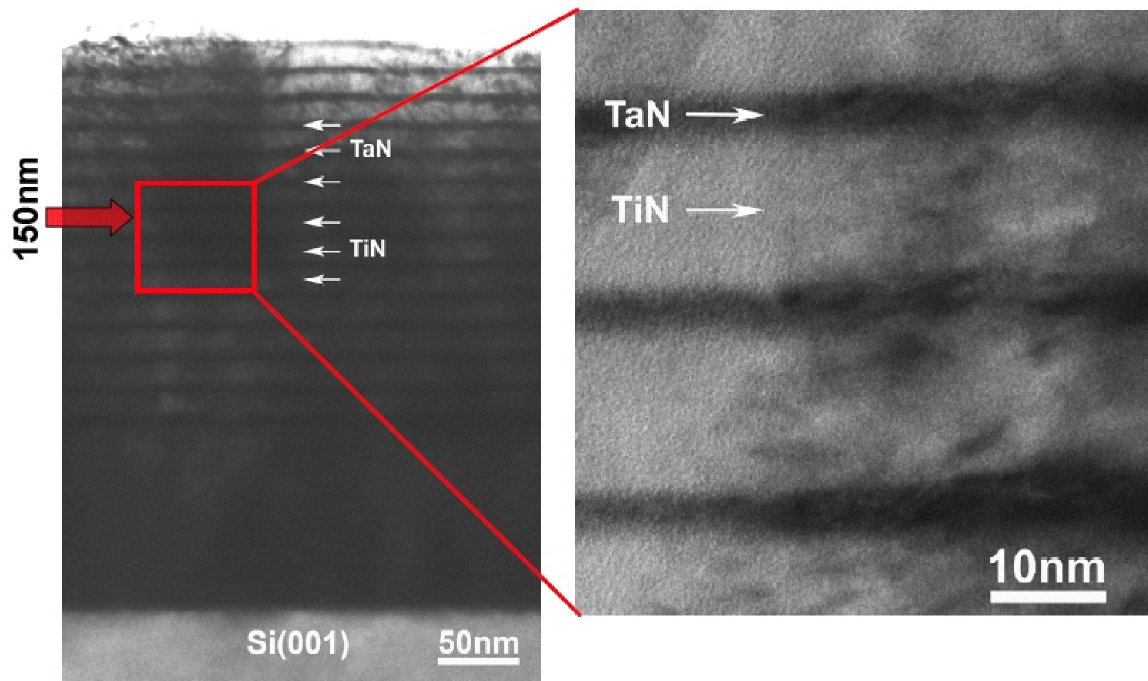

Fig. 3.6 TEM image of TiN/TaN multilayer after ion implantation (50keV)

After ion-irradiation, the images of TaN/TiN nanolayer films are shown in Fig. 3.6. The TaN and TiN can be clearly distinguished as dark and bright contrast layers uniformly grown on top of each other. No obvious intermixing was observed in the irradiated TaN 5 nm / TiN 20 nm specimen. In addition, detailed HRTEM study was conducted at the peak damage area where it is approximately down to 150 nm from the top surface. The interface is clear and no damage is observed in the area for the 5/20 nm TaN/TiN specimen at 50 keV.

However, the other sample (16 nm/2 nm) showed that He bubbles were observed along the layer interfaces. Due to He^+ irradiation with the fluence of 4.0×10^{16} cm^{-2} at 12 keV on 2/16 nm TaN/TiN, the He accumulation is observed at the layer interfaces where it is approximately down to 50 nm from the top surface as shown in Fig. 3.7. The straight and immiscible TaN/TiN interfaces could act as effective defects sinks and accumulate a large amount of vacancies and interstitials. In the high-resolution image of the area, the brightest contrast is observed at the interfaces between TiN and TaN nanolayers, which is possibly due to the high density He bubbles. As shown in the selected diffraction pattern, however, the TaN/TiN nanolayer is still cubic phase after ion irradiation without severe radiation damage on the crystal lattices.

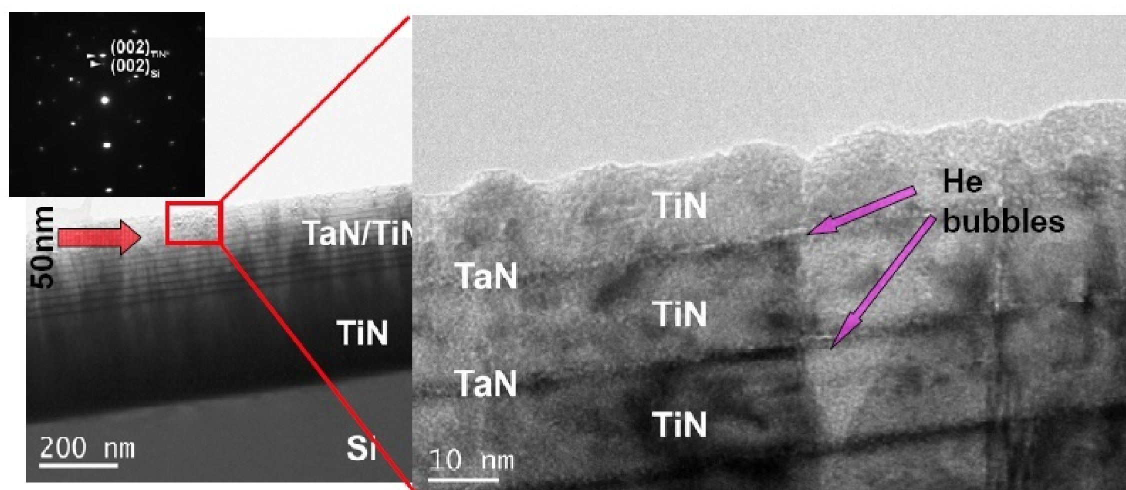

Fig. 3.7 TaN/TiN (16/2nm) nanolayer after ion irradiation: TEM examination suggests that the crystalline structure of the nanolayer structure remains after 12keV He, $4x10^{16}/cm^2$. Some He accumulation is observed at the layer interfaces.

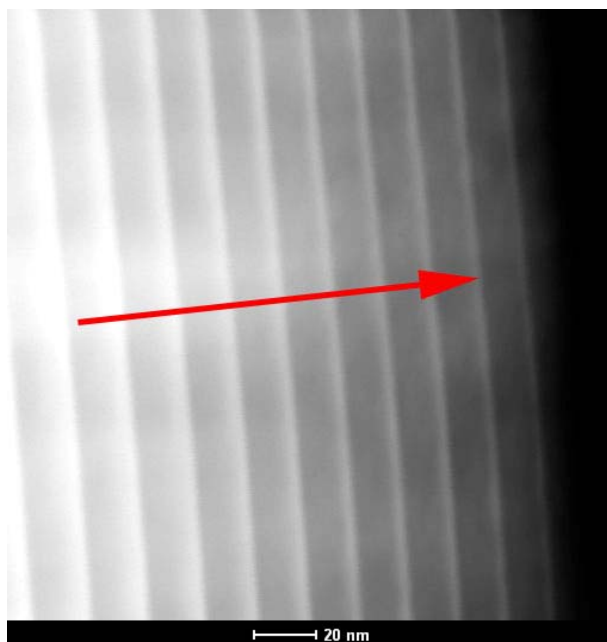

(a)

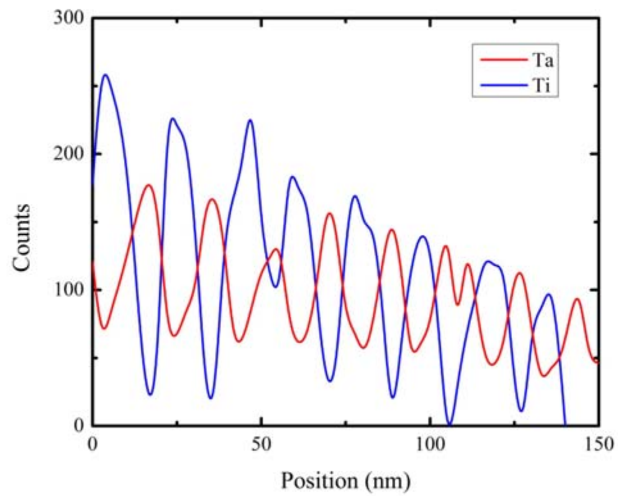

(b)

Fig. 3.8 STEM image (a) of 2/16 nm TaN/TiN and EDX analysis (b) after ion irradiation with 12 keV

The TaN/TiN interfaces remain chemically abrupt and can keep acting as effective sinks for defect accumulation and annihilation in the ion-irradiation process. It was confirmed by STEM and EDX study on the ion-irradiated 2/16 nm TaN/TiN specimen. STEM in high angle annular dark field (HAAD) mode is also called Z-contrast. The contrast is proportional to $Z^{1.7}$. As shown in Fig. 3.8 (a), the relatively bright thin layer is the TaN nanolayer and slightly darker thick layer is TiN nanolayer in the STEM image. No obvious layer mixing is observed after the ion irradiation. A detailed EDX line scan was conducted on the cross-sectional area following the direction of the red arrow marked in Fig. 3.8 (a).

The elemental composition variation of Ta and Ti is plotted in red and blue, respectively, in Fig. 3.8 (b). Following the scanning direction, the signal intensity decreases due to the TEM sample foil thickness decreases at the foil edge. Based on its periodic oscillation of the Ti and Ta signal, we can conclude that the TaN and TiN nanolayers still have distinguished interfaces and robust chemical bonding after ion-irradiation. This suggests that nanolayer structures posses a better ion irradiation tolerance property than single layer samples. The following mechanical property measurement further confirm the enhanced radiation tolerance of the nanolayer samples.

Radiation induced hardening was reported in metals [53-55], whereas hardness reduction (i.e., softening) was observed sometimes in single phase ceramic materials after ion-irradiation [56-58]. Hardness reduction in ceramics may be caused by amorphization or defect formation such as porosity due to ion irradiation. Hardness of each specimen as-deposited and ion-irradiated was in Fig. 3.9.

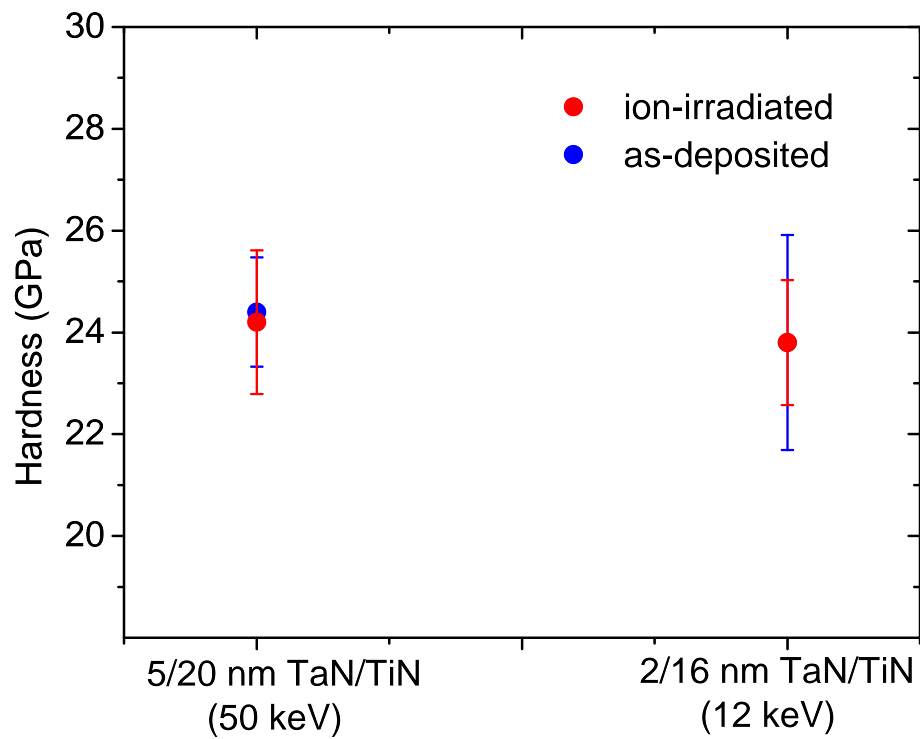

Fig. 3.9 Hardness of TaN/TiN specimens as-deposited and ion-irradiated with 50 keV and 12 keV He^+

The hardness of 5/20 nm TaN/TiN showed 24.4 GPa and 24.2 GPa for as-deposited and ion-irradiated by 50 keV He ion, respectively. That of 2/16 nm TaN/TiN was 23.8 GPa and 23.8 GPa with relatively high standard deviation for as-deposited and ion-irradiated by 12 keV He ion, respectively. Even if we observed the He bubbles in the interfaces, the hardness was almost constant. However, reduced modulus was reduced from 242.9 GPa to 174.3 GPa in the 2/16 TaN/TiN after ion-radiation. It is mainly due to the He bubble in the interfaces and slight damages in the thin nanolayer.

In nanocrystalline TiN after ion irradiation, no obvious amorphization was observed and the hardness reduced in the region near the top surface. We have previously reported that the damage within nanocrystalline TiN film appears to be recovered well possibly due to the annihilation process through grain boundaries. The high hardness of ion-irradiated TiN suggests a good radiation-tolerance property [5]. All TaN_x phases can be simply described as close-packed arrangements of Ta atoms, with the smaller N atoms inserted into interstitial sites. Therefore the resulting structure has significantly higher resistance to diffusion. Higher bonding energy and density of TaN than TiN make the TaN/TiN interfaces stable. The nanolayer samples show suppression of radiation damage which indicates that the nanolayer interface effectively assists the defect annihilation.

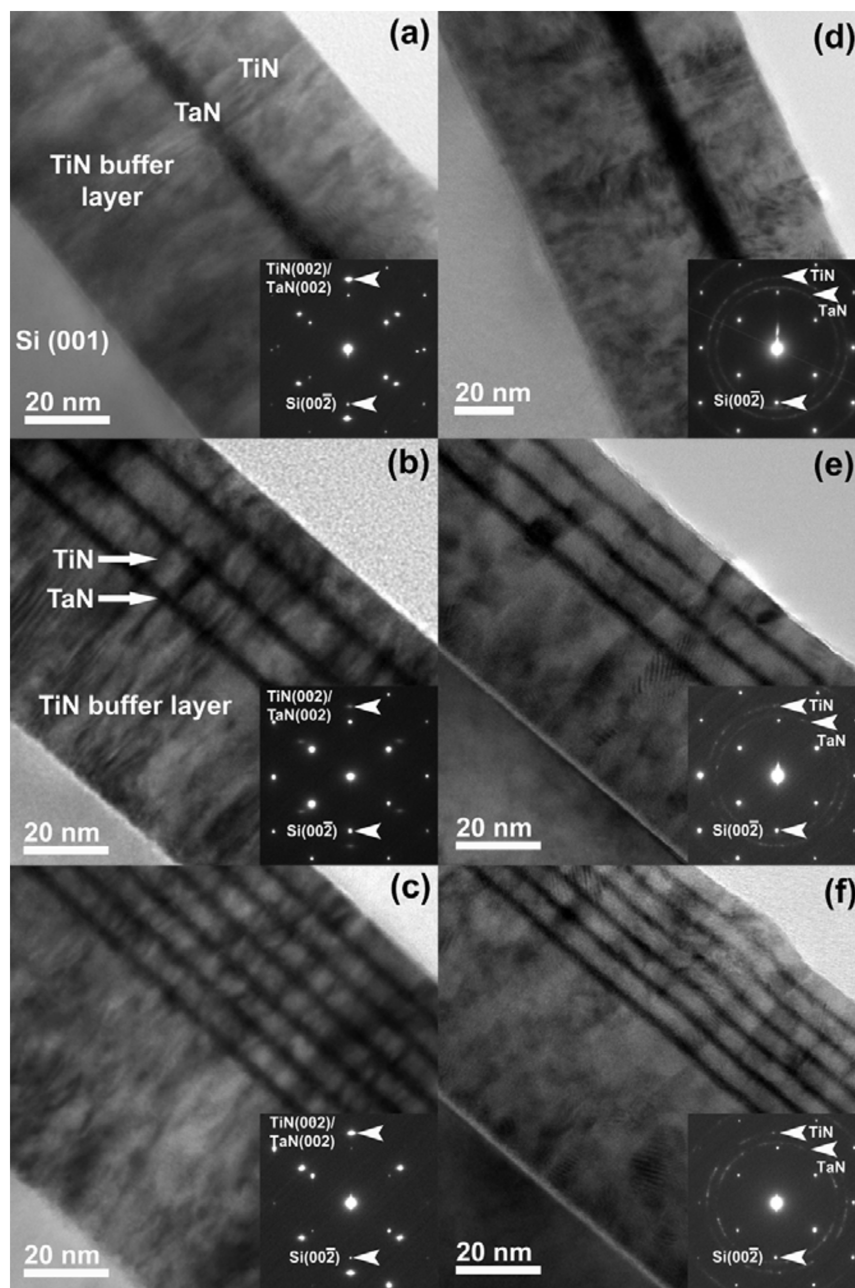

Fig. 3.10 Cross-sectional TEM images with selected diffraction patterns of TaN/TiN nanolayers with various thicknesses and interfaces between TaN and TiN layers on TiN Buffer layer: epitaxial cubic phase TaN/TiN (a), (b), and (c) and poly-crystalline TaN/TiN (d), (e), and (f)

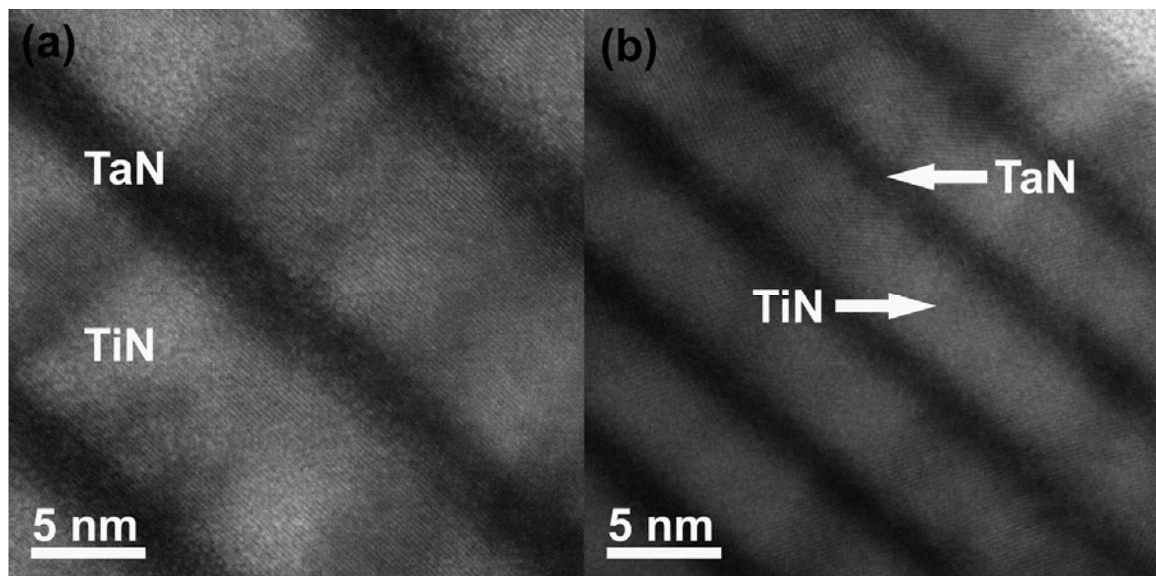

Fig. 3.11 High resolution cross-sectional TEM images of epitaxial 4nm and polycrystalline 2nm thick TaN specimens in TaN/TiN

The other set of samples that have various interfaces from two to twelve between TaN and TiN was studied for size and interface effect on electrical resistivity. Figure 3.10 shows XTEM images for specimens, which have 2, 6, and 12 interfaces with various nanolayer thicknesses corresponding to the same total thickness. In order to compare the crystal phase effect on resistivity as well as size and interface effect, two sets of samples were prepared at 700 °C and room temperature. The deposition temperature induced epitaxial cubic phase TaN/TiN and polycrystalline TaN/TiN nanolayers as shown in Fig. 3.10. The dark contrast layer is TaN and bright one is TiN layer. When the samples were fabricated, approximately 45 nm TiN was deposited on all area of substrates for buffer layer to initiate the epitaxial growth of TiN/TaN nanolayers. Then, the TaN/TiN nanolayer was deposited on the buffer layer after covering half-surface area with cleaned silicon wafer as shadow-mask. The SAD patterns of the high temperature deposited samples shows cubic structure in both of TaN and TiN nanolayers. As the diffraction ring implies, however, the samples deposited at room temperature had the expected polycrystalline structure in TaN and TiN nanolayers. Detailed HRTEM study compared the microstructures as shown in Fig. 3.11. The epitaxial growth of each nanolayer at high temperature sample is shown in Fig. 3.11(a) and it is evidently distinguished from the room-temperature deposited sample in Fig. 3.11(b). Thus, these samples are enough to compare microstructure effect on electrical resistivity in TaN/TiN nanolayers.

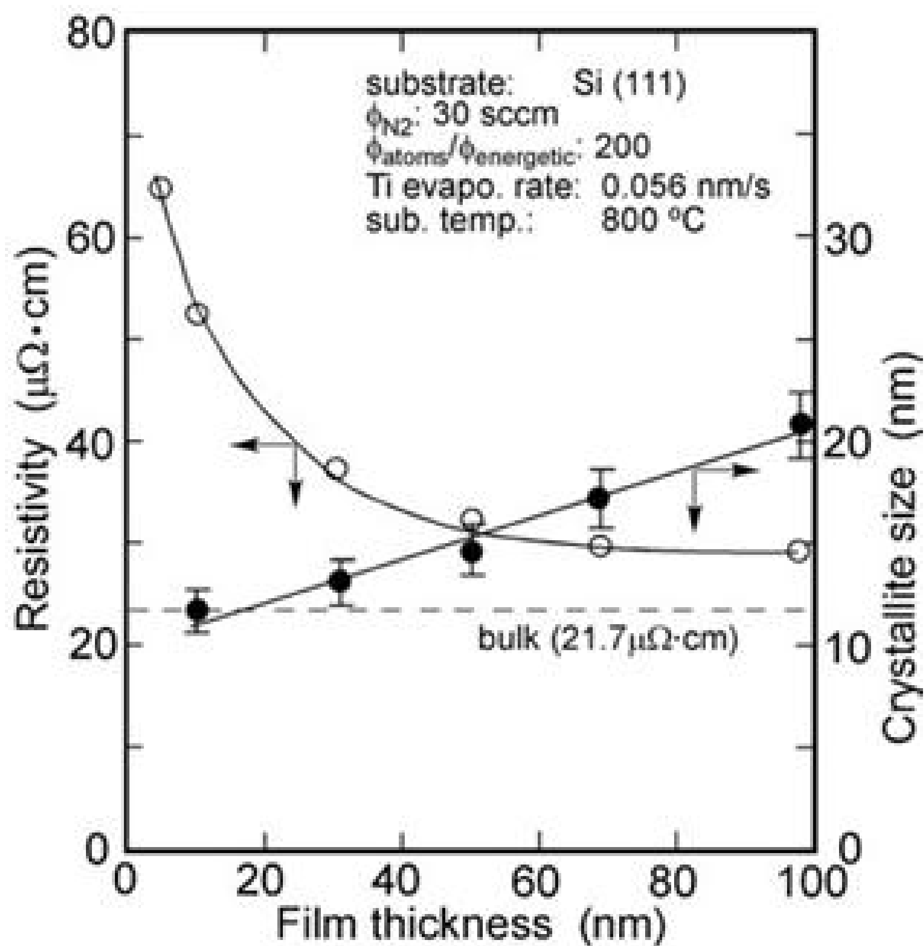

Fig. 3.12 Resistivity as a function of film thickness on TiN films deposited at 800 °C [59]

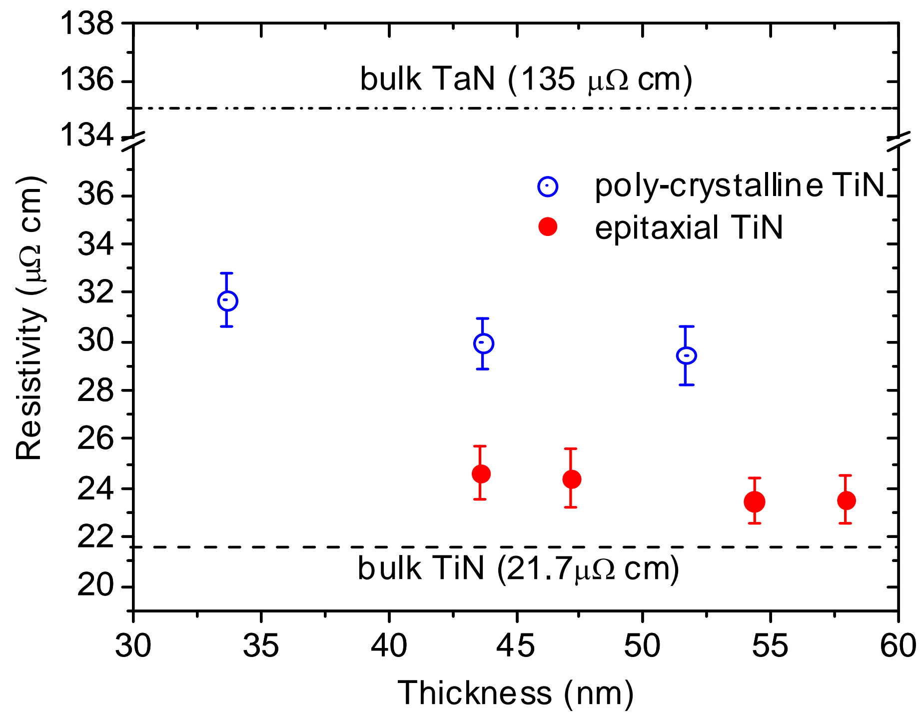

Fig. 3.13 Measured resistivity on epitaxial cubic phase and polycrystalline TiN single layers with various thicknesses

During TEM study, the thicknesses of all layers in samples were measured for resistivity calculation. Yokota et al. reported the size effect for surface boundary and grain boundary on resistivity of TiN thin film as shown in Fig. 3.12 [59]. Their results is used to compare size effect on resistivity of TiN single layer and TaN/TiN multilayer in this study. Applying four-point probe method on TiN layer, the sheet resistance of TiN single layers were measured with various thickness, then the resistivity was calculated as shown in Fig. 3.13. Comparing the bulk TiN [59], both of epitaxial and polycrystalline TiN thin films showed size effect on resistivity in the thickness regime. The resistivity of epitaxial TiN has 23.55, 23.47, 24.41, and 24.65 μΩ·cm for 57.9, 54.3, 47.2, and 43.6 nm single layers, respectively. Decreasing film thickness the resistivity gradually increased due to surface boundary scattering of electron. With the surface boundary scattering, polycrystalline TiN added grain size effect on the resistivity. Thus, the polycrystalline TiN thin film showed higher resistivity than epitaxial cubic phase TiN film, such as 29.47, 29.92, and 31.75 μΩ·cm for 51.7, 43.6, and 33.6 nm single layer, respectively. Meanwhile, TaN has different phase depending on substrate. All multilayer samples have TiN seed layer, so it is not available to compare resistivity of TaN single layer to that of TaN on TiN seed layer.

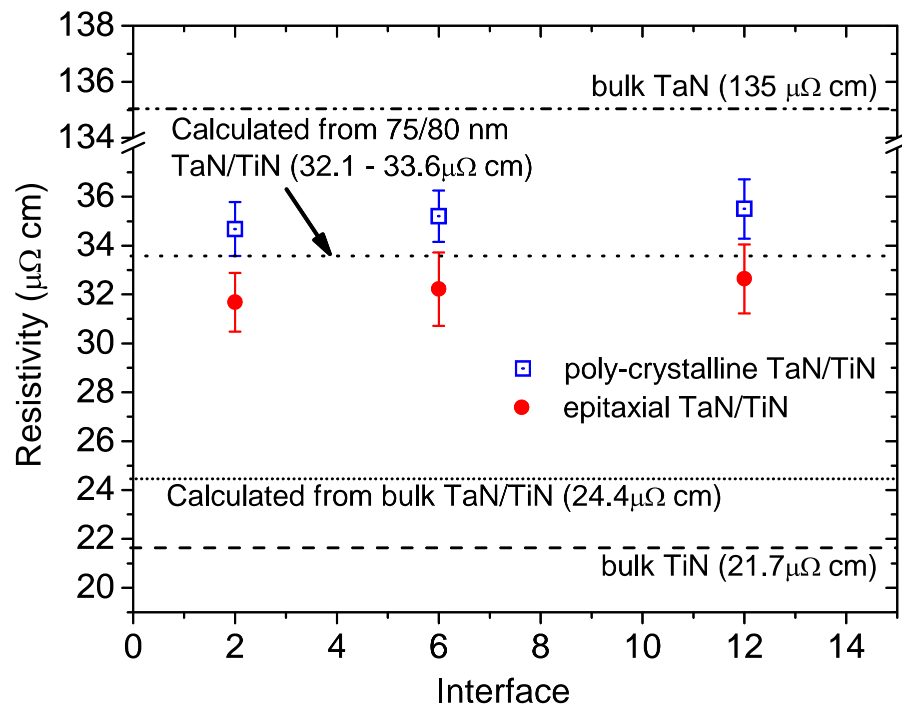

Fig. 3.14 Measured resistivity on epitaxial cubic phase and polycrystalline TaN/TiN nanolayers with various number of interface

Figure 3.14 shows the measured resistivity from sheet resistance on the multilayer film and calculated resistivity from other researcher's results [59, 60]. The measured resistivity is 32.64, 32.22, and 31.69 μΩ·cm for 12, 6, and 2 interfaces in epitaxial cubic phase, respectively. Polycrystalline TaN/TiN has higher values as 35.50, 35.21, and 34.68 μΩ·cm for 12, 6, and 2 interfaces, respectively. Comparing with the calculated resistivity from bulk values (TiN: 21.7 μΩ·cm and TaN: 135 μΩ·cm), the measured resistivity is much higher than that due to size effect. According to previous results from Yokota *et al*.[59] and Shen *et al*.[60], the size effect on resistivity is dominant in the thickness regime, and the resistivity significantly increased from bulk values for both of TaN and TiN. Recalculated resistivity from the size effected results [59, 60] are higher than that of epitaxial film and slightly lower than polycrystalline films.

3.5 Summary

Epitaxial cubic phase and polycrystalline TaN/TiN multilayer films could be deposited on TiN seed layer by PLD method. TEM and nanoindentation study of the ion-irradiated TaN/TiN multilayer films showed better ion-irradiation tolerance properties than single layers. The nanolayer samples did not show hardness reduction after ion-irradiation but He bubbles were observed in the interfaces in 2/16 nm TaN/TiN specimens. It caused the reduced modulus decreased after ion-irradiation. This study indicates that the metastable interface and composition of robust TiN and TaN nanolayer

achieved the good radiation tolerance properties in nanolayer systems. In this multilayer, the size effect was dominant on resistivity rather than interface effect. Grain size affected on both of epitaxial cubic phase and polycrystalline TaN/TiN, and it increased the resistivity due to grain boundary scattering in the thin thickness regime.

CHAPTER IV

HIGHLY TEXTURED AND EPITAXIAL AlN/TiN NANOLAYERS WITH ENHANCED RADIATION TOLERANCE PROPERTIES

4.1 Overview

The effect of interfaces on materials radiation tolerance has been investigated for nanolayered TiN/AlN films, with individual layer thickness varied from 5 nm to 50 nm and prepared by pulsed laser deposition. Evolution of the microstructure and hardness of the multilayer films were examined on the specimens before and after He ion-implantation to a fluence of 4×10^{16} cm^{-2} at 50 keV. The suppression of amorphization in AlN layers and the reduction of radiation-induced softening were observed in all nanolayer films. Radiation tolerance was found to be size dependent and the layer thickness leading to the highest radiation tolerance was 10 nm. The study shows that radiation tolerance can be manipulated by changing interfaces and layer thickness. The findings are important for a wide range of applications using nitride-based ceramic materials in harsh environments.

4.2 Introduction

Ion-irradiation tolerance properties in ceramics have attracted extensive research interests because ceramics have many envisioned applications in advanced nuclear

reactors [61]. Recently, nitrides are considered to be one of the advanced nuclear fuel forms for waste storage and can act as effective diffusion barriers to minimize fuel-cladding interactions [4, 5]. Ion irradiation-induced amorphization in ceramics has been previously reported as one primary degradation phenomenon in ceramics [6]. For the case of homogeneous amorphization, progressive defect accumulation, such as accumulation of point defects, causes amorphization after a critical defect concentration level. This model is usually applied in light-ion irradiation for which separated point defects are dominant. For the case of heterogeneous amorphization, it is a complicated process involving creation of individual collision cascades, overlap of collision cascades, and nucleation and growth of the amorphous domains [6].

Enhanced radiation tolerance in nanocrystalline or nanolayered metallic systems have been reported both experimentally and theoretically. For example, microstructural changes caused by helium ion-irradiation in several multilayer systems, including immiscible Cu/Nb [16], Cu/V [7], and miscible Al/Nb [17], and Fe/W [8], have been systematically studied. It was reported that certain type of immiscible interfaces, such as Cu/V, could significantly enhance ion-irradiation tolerance of metallic materials compared with bulk counterpart. Dramatic reductions of swelling, bubble density, lattice expansion and radiation hardening are observed in Cu/V multilayers, wherein interface act as effective sinks to absorb radiation induced point defects and promote the annihilation of opposite type of defects (Frenkel pairs), and consequently reduce the overall point defect density in the multilayers [7, 8, 16, 18].

Despite the fact that the ion irradiation damage has been studied in several nanolayered metallic systems, similar studies on nanostructured or nanolayered ceramics [5, 9, 10] are scarce. We have previously reported enhanced radiation tolerance in nanocrystalline TiN coatings [5], in which grain boundaries act as effective sinks for defect accumulation and annihilation. Reducing grain sizes increases the areas of grain boundaries, which are defect sinks, and thus leads to significantly enhanced radiation tolerance. On the other hand, Shen *et al*. [62], reported that nanocrystalline structures may enhance [63] or reduce [64-66] radiation tolerance depending on ceramic systems. These studies suggest that the interface characteristics also play an important role in the overall radiation tolerance properties in ceramics.

In this work, we investigated the interfacial effects on the ion-irradiation tolerance of nitride ceramics by synthesizing a series of TiN/AlN nanolayer with individual layer thickness varying from 5 to 50 nm. By varying the nanolayer thickness we controlled the interfacial density in the system, which made it possible to systematically explore the interfacial and nanolayer thickness effects. TiN was selected as it has good radiation tolerance [5], a high melting point of 2950 ^{o}C, a hardness of ~33 GPa [67] in thin film form, high corrosion resistance, and excellent adhesion on a variety of steel substrates. AlN has superior thermal stability and high oxidation resistance. AlN film has lower hardness (~24 GPa) [67] than TiN film and is suspected to be more susceptible to irradiation damage than TiN. A detailed mechanical testing and microstructural study before and after ion irradiation were conducted to characterize defects and interfacial microstructures as a function of layer thickness.

4.3 Experimental details

TiN and AlN single layers and TiN/AlN multilayer thin films were deposited by pulsed laser deposition technique in an ultrahigh vacuum chamber with a KrF excimer laser (Lambda Physik Compex Pro 205, λ = 248 nm, 10 Hz). Laser beam was focused to obtain an energy density of approximately 6 $J \cdot cm^{-2}$ at 45° angle of incidence. TiN and AlN targets were hot-pressed stoichiometric TiN and AlN obtained from Plasma Materials Inc. The single layer and multilayer films were deposited at a typical growth rate of 0.6 Å/pulse for TiN layer and for 1.0 Å/pulse for AlN layer with a base pressure of approximately 10^{-7} Torr and deposition temperature of 700 °C. Prior to film deposition, the Si (001) substrates were cleaned in acetone and methanol followed by etching in hydrofluoric acid to remove natural silicon oxide layer on surface.

A computer-controlled 6-target exchangeable target carousel was used to precisely control the growth of nanolayer samples. A 100 nm-thick TiN layer was first deposited on silicon substrates as a buffer layer to initiate the high quality growth of TiN/AlN nanolayers. Then the TiN/AlN nanolayer films were deposited with identical individual layer thickness, h, of 5, 10 20, and 50 nm, while keeping the total film thickness to be 500 nm (including the 100 nm TiN buffer layer and the outermost layer was TiN).

All samples were then irradiated at room temperature with He ions to a high fluence of 4×10^{16} cm^{-2} at 50 keV. Microstructural evolution of the irradiated films was characterized by cross-section transmission electron microscopy (XTEM) and high

resolution TEM (HRTEM) using a JEOL-3000F and JEOL 2010 analytical electron microscope with resolution of 0.18 nm and 0.23nm, respectively.

Hardness of all films was measured with a Hysitron Tribo-nanoindenter. The measurement was performed using a standard Berkovich diamond tip under a constant load mode with load varied from 2000 to 3200 μN. In order to minimize any substrate effect on hardness measurements, the penetration depth was controlled to be less than 20 % (~100nm) of total film thickness. Hardness and elastic modulus are calculated based on an average of at least nine indentation experiments per indentation depth. A plateau is typically observed in the hardness vs. indentation depth plot and the plateau value is chosen as the average hardness of the films.

4.4 Results and discussion

Figure 4.1 shows the simulated damage profiles in single layer TiN and AlN caused by 50 keV He ion irradiation to a fluence of 4.0×10^{16} cm^{-2} by using SRIM 2008 [52]. The peak damage for the TiN and AlN single layer cases is ~ 4.3 dpa at 190 nm and 3.9 dpa at 280 nm in depth, respectively.

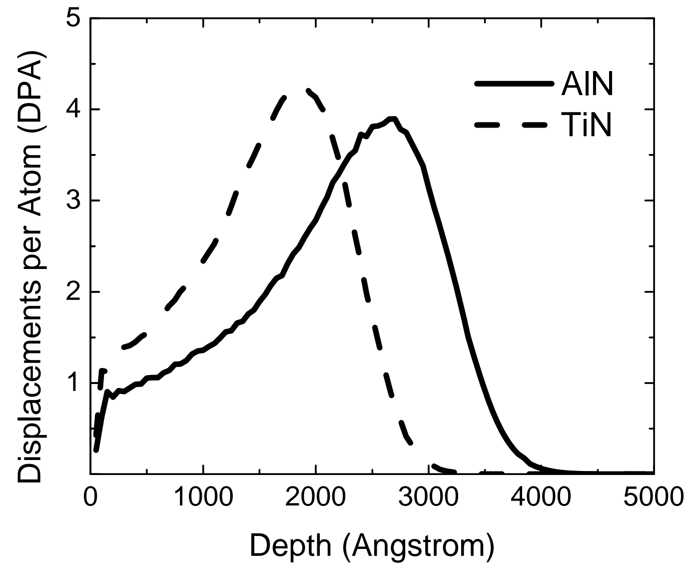

Fig. 4.1 SRIM simulation provides a guideline for the ion radiation experiment and compares damage vs. depth after ion implantation of 50 keV He ion for TiN and AlN single layers.

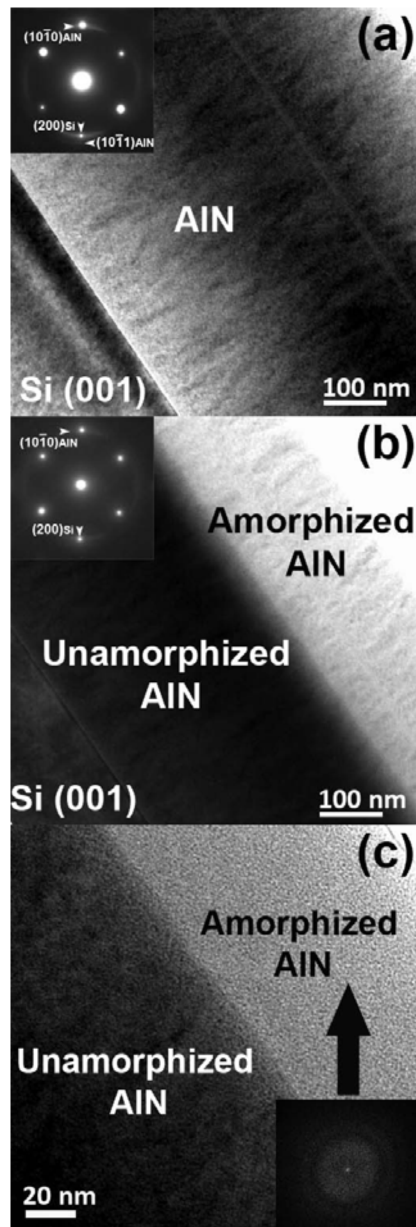

Fig. 4.2 Low magnification XTEM micrographs and selected area diffraction (SAD) patterns of AlN single layer films for (a) as-deposited and (b) ion-irradiated with He^+ 50 keV ions at a dose of $4x10^{16}$ cm^{-2}, and (c) HRTEM image and FFT of the amorphized regime in AlN single layer film after radiation.

As-deposited and ion-irradiated specimens were examined by XTEM to study the microstructure evolution due to ion irradiation. Figure 4.2(a) and 4.2(b) show the low magnification XTEM images of an AlN single layer film before and after ion-irradiation, respectively. It is evident that the as-deposited AlN film was highly textured nanocrystalline throughout the film thickness, whereas a layer with bright contrast was observed in the ion-irradiated AlN film from surface to ~ 280 nm into the films in the Fig. 4.2(b). The thickness of this radiated region coincides with the peak damage position predicted by SRIM calculation. HRTEM reveals that the damage layer has an amorphous structure, separated from the unirradiated nanocrystalline AlN with a clear interface as shown in Fig. 4.2(c). The Fast Fourier Transform (FFT) of the high resolution image of Fig. 4.2(c) in the bright contrast area shows diffuse ring pattern which further confirms the amorphous structure.

XTEM images with selected area diffraction (SAD) pattern of TiN/AlN nanolayer films are shown in Fig. 4.3 (h = 20 nm) and Fig. 4.4 (h = 5 nm) for as-deposited (4.3a and 4.4a) and ion-irradiated (4.3b and 4.4b) specimens, respectively. The TiN and AlN can be clearly distinguished as dark and bright contrast layers uniformly grown on top of each other. No obvious intermixing was observed in irradiated TiN 20 nm / AlN 20 nm (referred to as TiN/AlN 20 nm thereafter) specimen, and TiN/AlN 10 nm sample (not shown here). However, in the TiN/AlN 5 nm nanolayer sample, several regions close to the sample surface show signs of intermixing as shown in Fig. 4.4(b), but diffused diffraction rings (an indication of amorphization) were not observed in all radiated nanolayers.

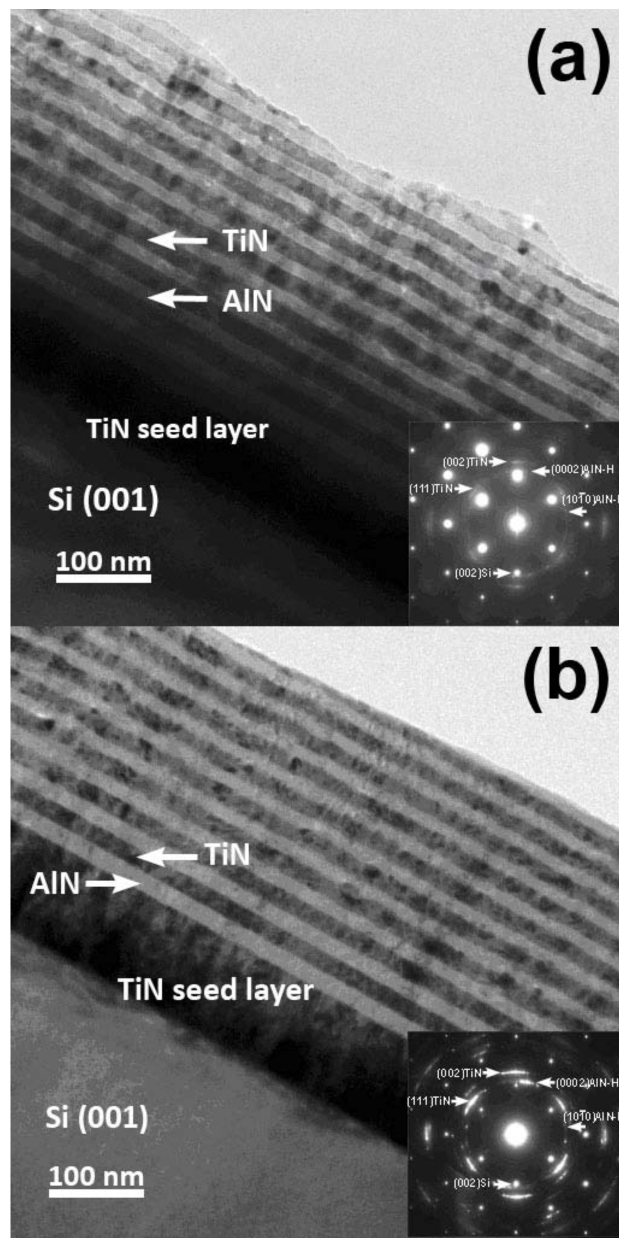

Fig. 4.3 Low magnification XTEM micrographs and SAD patterns of TiN/AlN 20/20 nm sample: (a) as-deposited and (b) ion-implanted with He^+ 50 keV ions at a dose of $4x10^{16}$ cm^{-2}

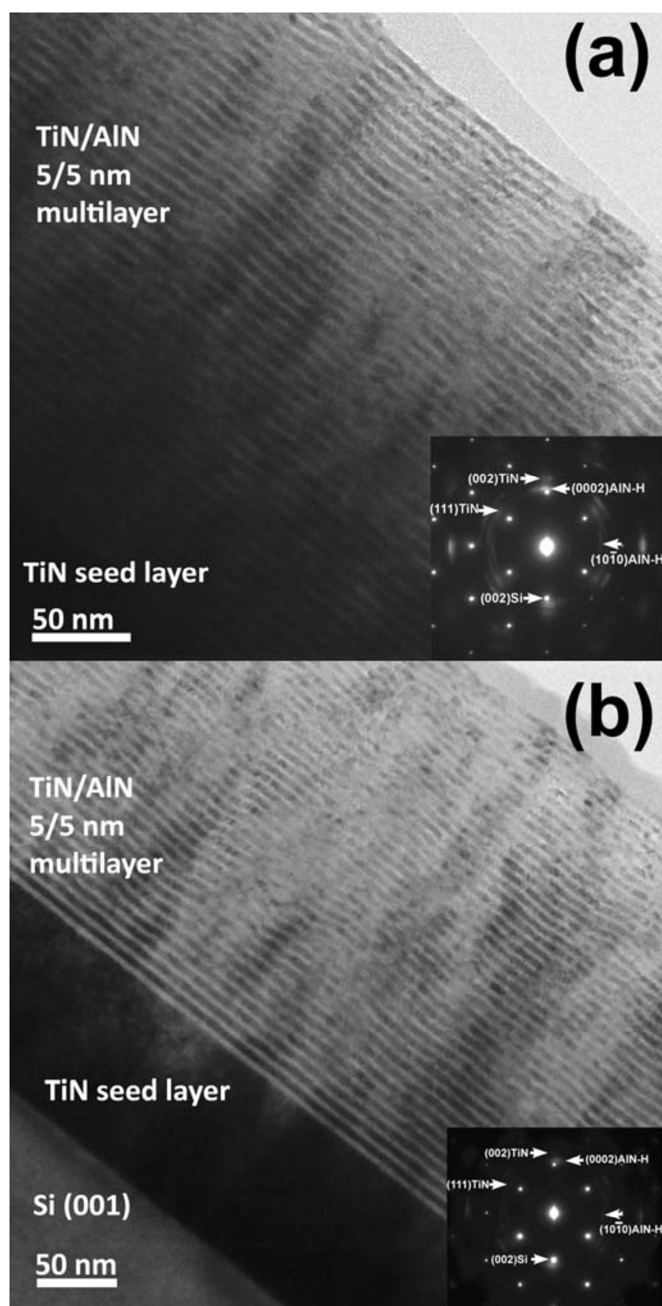

Fig. 4.4 Low magnification XTEM micrographs and SAD patterns of TiN/AlN 5/5 nm sample: (a) as-deposited and (b) ion-implanted with He^+ 50 keV ions at a dose of $4x10^{16}$ cm^{-2}

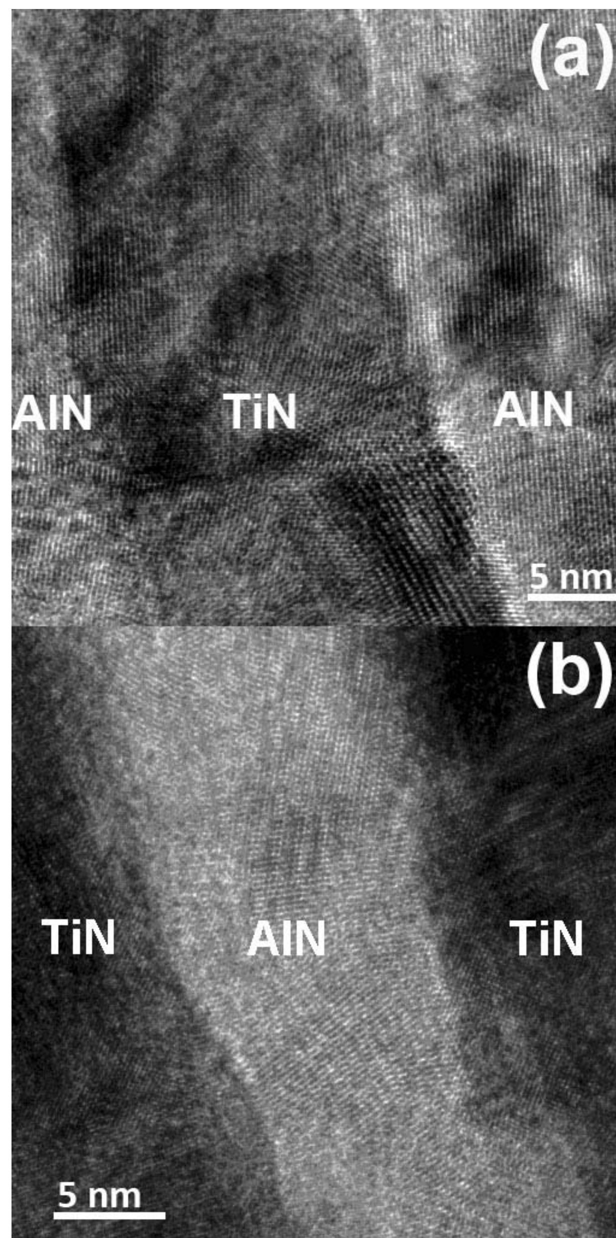

Fig. 4.5 HRTEM micrographs and SAD patterns of TiN/AlN 20/20 nm sample: (a) as-deposited and (b) ion-irradiated with He^{+} 50 keV ions at a dose of $4x10^{16}$ cm^{-2}

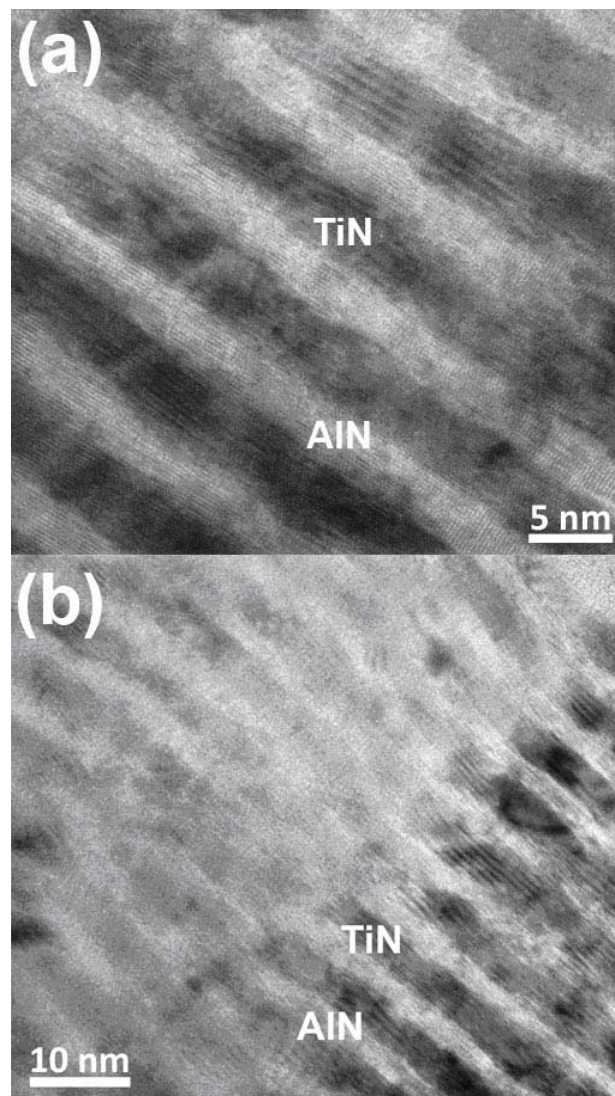

Fig. 4.6 High resolution cross-section TEM micrographs and SAD patterns of TiN/AlN 5/5 nm sample: (a) as-deposited and (b) ion-irradiated with He^+ 50 keV ions at a dose of $4x10^{16}$ cm^{-2}

Detailed HRTEM study was conducted on all the samples at the peak damage regime before and after ion irradiation. Two typical examples are shown in Fig. 4.5 (h = 20 nm) and Fig. 4.6 (h = 5 nm) for as-deposited of 4.5(a) and 4.6(a), and ion-irradiated of 4.5(b) and 4.6(b) specimens. One important observation is that for nanolayers with h greater than 5 nm, AlN remains its predominantly crystalline structure after ion-irradiation. This can be confirmed from the clear crystalline lattices of AlN in the irradiated TiN/AlN 20 nm nanolayers as shown in Fig. 4.5(b). However, certain regions of the irradiated TiN/AlN 5 nm nanolayers showed intermixing along interfaces as shown in Fig. 4.6(b). This suggests that the ion irradiation damage can cause interlayer mixing and the effect of interface might be reduced when layer thickness decreases to a certain level. For the cases of 10 nm and 20 nm samples, the interfaces remain chemically abrupt and can keep acting as effective sinks for defect accumulation and annihilation in the ion-irradiation process.

Hardness vs. indentation depth was plotted for all the single and multilayer films before and after ion-irradiation in Fig. 4.7(a) and (b), respectively. The hardness of all as-deposited specimens approached a constant value at indentation depth deeper than 60 nm as shown in Fig. 4.7(a). Respective average hardnesses of as-deposited TiN and AlN single layers were 31.0 GPa and 23.8 GPa, and similar to previous reports [67]. The hardnesses of TiN/AlN nanolayers are, in general, close to the rule-of-mixture hardness values, ~ 27.4 GPa, with the exception that TiN/AlN 50 nm has a slightly lower hardness of 25.9 GPa.

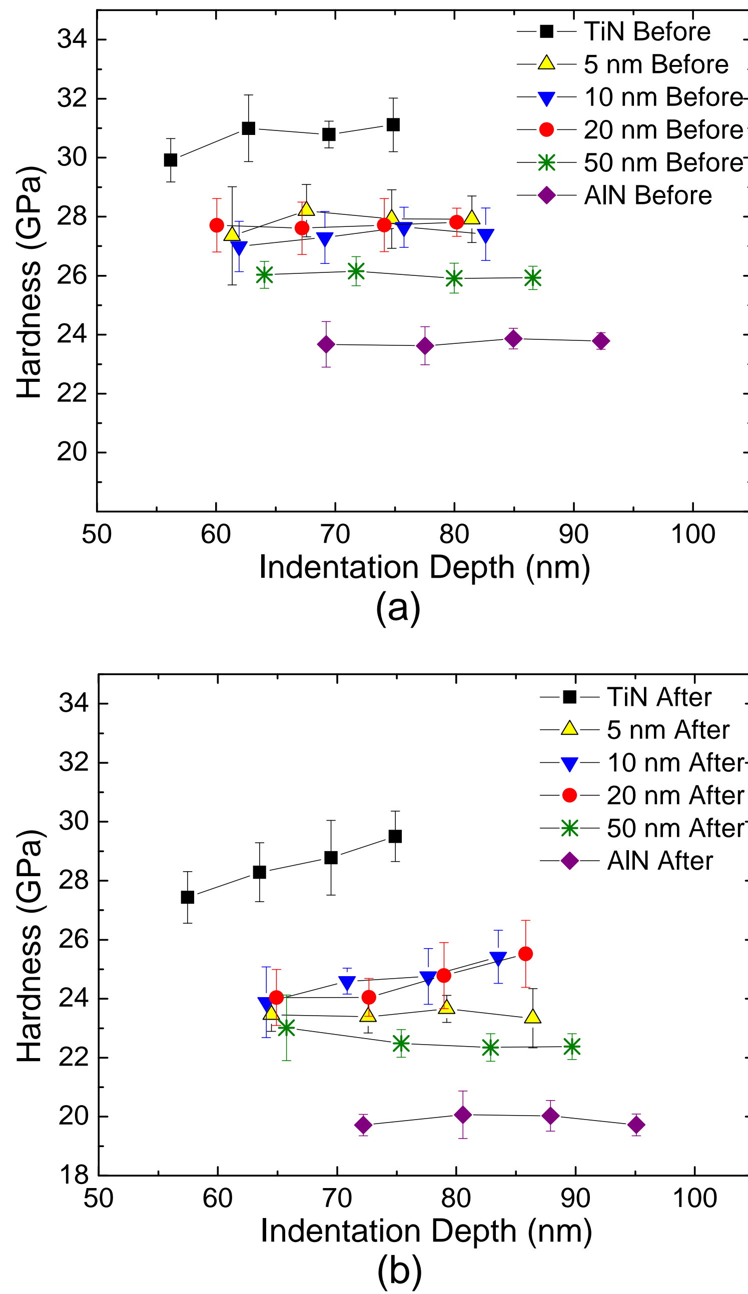

Fig. 4.7 Hardness vs. indentation depth for (a) as-deposited and (b) ion-irradiated TiN and AlN single layer and TiN/AlN multilayer films

Hardness of the irradiated TiN and AlN single layers is both lower than as-deposited films, as shown in Fig. 4.7(b). The TiN single layer film showed an upward dependence of hardness vs. indentation depth, and its hardness reached 29.5 GPa at 75 nm indentation depth, ~ 5 % lower than as-deposied films. However, the ion-irradiated AlN single layer specimen had a relatively constant hardness of 19.7 GPa regardless of indentation depth up to 95 nm. The hardness reduction in AlN films is approximately 17 % compared to the as-deposited film. The rule-of-mixture hardness calculated from irradiated single layer TiN and AlN. It indicates that the radiation damage has reached much deeper than the indentation depth (95 nm) inside of the AlN single layer. This result is consistent with the simulated damage profiles in Fig. 4.1 and the XTEM observation of radiation-induced amorphization in AlN film as shown in Fig. 4.2 while in TiN no obvious amorphization was observed [5].

Hardness reduction was observed, in Fig. 4.7(b), in all multilayers after ion irradiation. However, the depth dependent hardness variation shows different trands. First, when h = 10 and 20 nm, film hardness increased with indentation depth, a trend similar to that of radiated TiN film. On the contrary, the ion-irradiated TiN/AlN 5 and 50 nm nanolayer specimens followed the trend of the irradiated AlN film, i.e., insignificant depth dependent hardness.

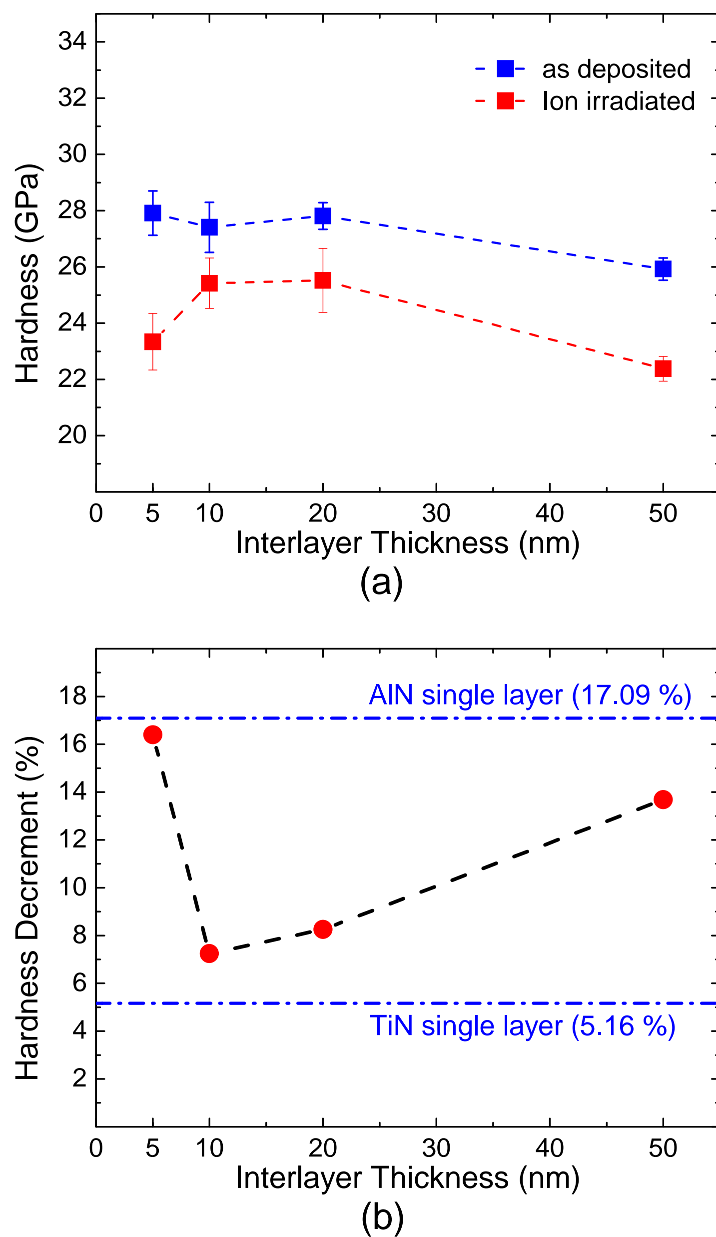

Fig. 4.8 (a) Averaged hardness vs. nanolayer thickness for as-deposited and ion-irradiated TiN/AlN nanolayer films and (b) Hardness decrement vs. nanolayer thickness for all nanolayer samples with dashed lines indicating the hardness reduction for single layer AlN and TiN samples

Layer thickness dependent hardness values are plotted in Fig. 4.8(a), and the hardness reductions in percentage (%) are shown in Fig. 4.8 (b). Because of the upward hardness trend with increasing indentation depth in some of specimens, the hardness comparison for all specimens was based on the data measured at the maximum indentation depth. Hardness of all multilayers reduced after radiation. Radiation softening in TiN/AlN 10 and 20 nm nanolayers is less significant than rule-of-mixture softening, whereas more softening is observed when h = 5 and 50 nm. As shown in Fig. 4.8(b), the hardness reductions for 5 and 50 nm samples are around 16.4 % and 13.7 %, respectively, approaching that of irradiated AlN single layers. Meanwhile, the respective hardness reductions for both 10 and 20 nm samples, ~ 7.3 % and 8.3 %, are very close to irradiated TiN single layers. The magnitude of radiation softening initially decreased with decreasing h, but a reversal occurs when h = 5 nm, whereas radiation softening is greater than the hardness reduction of 10.2 %, calculated from the rule of mixture irradiated TiN and AlN single layers.

In nanocrystalline TiN after ion irradiation, no obvious amorphization was observed and the hardness reduced in the region near the top surface. We have previously reported that the damage within nanocrystalline TiN film appears to be recovered well possibly due to the annihilation process through grain boundaries. The high hardness of ion-irradiated TiN suggests a good radiation-tolerance property [5]. It is possible that the Ti-N bonding is much stronger than the Al-N bonding therefore the loss of nitrogen [68] in TiN might not be as severe as that in AlN at the same dose range.

Heavy ion irradiation in single-crystal wurtzite AlN epilayers [69] and neutron irradiation in bulk AlN [70] has been previously studied and reported as relatively stable structure without easy amorphization by heavy ion irradiation. A possible dynamic annealing mechanism was observed by Kucheyev *et al.*[69] in the single-crystal AlN film after heavy ion irradiation at the fluence of 4.0×10^{16} cm^{-2} with 300 keV Au ion irradiation. However, we observed amorphization in polycrystalline AlN films after He ion irradiation with a dpa of ~4 at the peak damage region, which corresponds to a fluence of 4.0×10^{16}. The difference can be explained by the fact that the AlN thin films processed by PLD might be slightly N deficient, i.e., some N-vacancies exist in the films. This might lead to different amorphization threshold fluences. Another explanation comes from the role of gas atoms in defect annealing. For gas ions, e.g., He^{+}, it prefers to decorate open volume defects. The preferential trapping of He atoms with vacancies is believed to stabilize vacancies, and make the energy barrier for interstitial-vacancy recombination much higher. Also, the promoted bubble/void formation in gas ion irradiation further decreases the point defect recombination rate due to preferential trapping of vacancies toward voids. We believe that it is necessary to systematically study the ion specie dependence of AlN amorphization and the threshold fluency for amorphization cannot be simply normalized by dpa under different ion irradiation conditions.

Radiation induced hardening was reported in metals [53-55], whereas hardness reduction (i.e., softening) was observed sometimes in single phase ceramic materials after ion-irradiation [56-58]. Hardness reduction in ceramics may be caused by

amorphization or defect formation such as porosity due to ion irradiation. In addition, possible replacement of vacancies by radiated ions may also affect the hardness as a function of ion species, ion dose, and ion damage peak position. Milosavljevic *et al.*[9] reported a dose dependence in hardness, i.e., reduction then followed by a hardness increase as the Ar ion dose increased up to 4×10^{16} cm^{-2} (200 keV Ar ion) in AlN/TiN nanolayers. It was reported that the hardness increase was due to radiation indeed Ti migration into AlN layers. We conducted a thorough nanoindentation study in the sample regions shallower than the peak damage regions for all the single layer and multilayer samples. Amorphization and hardness reduction were observed in AlN single layer specimen, while the embedded AlN nanolayers in TiN/AlN multilayer systems was clearly not amorphized and the hardness reduction was mediated depending on nanolayer thickness. No obvious nanolyer mixing was observed in the 10 nm- and 20 nm-samples. The nanoindentation result is consistent with the TEM observation and gives a quantitative evaluation on the nanolayer interface effects in the overall defect generation and annihilation process.

All nanolayer samples show suppression of amorphization in AlN layers which indicates that the nanolayer interface effectively assists defect annihilation. However this interface effect varies as a function of nanolayer thickness, i.e., the size dependence. The optimum thickness range is 10-20 nm as samples show the least hardness reduction in this regime. In this thickness regime, it is highly possible that the interstitials and vacancies generated during ion bombardment can diffuse to nearby interface regime and recombine more effectively at the interface boundaries, i.e., annihilate with each other at

the interfaces. As the nanolayer thickness increases, the samples have less number of interfaces in the system and the interfacial effect becomes less significant, e.g., the hardness decrement in 50 nm-nanolayer sample is approaching that of the single AlN sample. However, the 5 nm sample is an exception. This sample has the highest density of interfaces compared to the other nanolayer samples. Nevertheless, the hardness results and HRTEM study (Fig. 4.6) showed more severe radiation damage in the 5 nm sample than the 10 nm-, 20 nm- and 50 nm-samples. This suggests an optimum nanolayer thickness (h) range exists for different materials, e.g., for TiN/AlN nanolayers, 10-20 nm each layer tends to show the best radiation tolerance property. We believe that at this thickness range, the vacancies and interstitials generated in AlN and TiN possibly have a similar order of the displacement (d), and thus can easily reach to the nanolayer interface and annihilate at the interface regions. As nanolayer thickness decreases to 5 nm, the ion bombardment induced interlayer mixing becomes an issue as the vacancies and interstitial displacement d becomes larger than the nanolayer thickness h. For example, Al interstitials generated in AlN layer can reach beyond the first immediate interface and can diffuse into TiN layers. As the interface get less sharp, the interface effects will reduce. The interfaces in AlN/TiN system indeed act as effective sinks for defect accumulation and annihilation process within its optimum thickness regime where d is close to h.

4.5 Summary

TEM and nanoindentation study of the ion-irradiated TiN/AlN multilayer films showed better ion-irradiation tolerance properties than single layer AlN where an obvious suppression of amorphization in AlN observed in all the nanolayer samples. The nanolayer samples showed the best ion-irradiation tolerance in 10 nm and 20 nm nanolayer specimens, most likely because the vacancies and interstitial displacement *d* is very close to the nanolayer thickness and defects can reach to the nanolayer interfaces and annihilate effectively. Compared with the 10 nm and 20 nm samples, both 50 nm- and 5 nm-nanolayer samples show less ion-irradiation tolerance due to less number of nanolayer interfaces and less stable interfaces, respectively. This study indicates that stable interfaces substantially reduce the ion-irradiation-induced damage, and there is an optimum nanolayer thickness range (i.e., size dependence) for nanolayer samples achieving the best radiation tolerance properties in nanolayer systems. Such optimum thickness range might vary depending on materials.

CHAPTER V

EXPERIMENTAL INVESTIGATION OF SIZE EFFECT AND PHASE INFLUENCE ON THERMAL PROPERTY OF TiN/AlN/TiN NANOLAYERS

5.1 Overview

TiN thin films and TiN/AlN/TiN system were prepared with various thicknesses and epitaxial cubic and polycrystalline phase structures by PLD method. Microstructure and thermal transport properties of the films have been experimentally investigated for crystal phase and size effects in the TiN single layer and the embedded AlN layer in tri-layered TiN/AlN/TiN films. The through-plane intrinsic thermal conductivity K_{int} was significantly decreased from 9.6 $Wm^{-1}K^{-1}$ at 41 nm down to 6.0 $Wm^{-1}K^{-1}$ at 9 nm thick epitaxial TiN film by surface boundary scattering of heat carrier. In addition, polycrystalline TiN film showed thermal conductivity drop that is from 8.0 $Wm^{-1}K^{-1}$ at 38 nm down to 4.6 $Wm^{-1}K^{-1}$ at 9 nm, which is influenced by additional grain boundary scattering of carrier.

Depending on phase of the embedded AlN by cladding TiN, the epitaxial cubic AlN showed higher effective thermal conductivity than that of polycrystalline AlN in the thickness ranged from 10 nm down to 2 nm. The result shows that grain boundary scattering of phonon and the phase of structure effect on thermal conductivity are still dominant in the ultra-thin nanolayer regime as well as the surface boundary scattering of phonon. The embedded epitaxial cubic AlN experienced the suppressed size effect,

which reduces the amount of decrease in through-plane thermal conductivity. The minimum effective thermal conductivity of the embedded cubic AlN with 2 nm thickness was higher than that of single layered cubic AlN reported reported and the embedded polycrystalline AlN showed more decrease than cubic AlN in the effective thermal conductivity.

5.2 Introduction

Titanium nitride and aluminum nitride coatings have been widely applied and studied as high temperature diffusion barrier for silicon devices in microelectronics, wear resistant coatings in turbine blade materials, and materials for future high temperature nuclear reactors [71-73]. In order to enhance mechanical property such as excellent hardness, superlattice is one of artificially engineered protective coatings. However, since material properties of ultra-thin films can vary dramatically from their bulk value due to the dimension of the film, one may expect to the altered thermophysical properties for thin films. The superlattice feature is not only for the enhanced mechanical property, but also for controllable thermal properties, such as thermal management or heat removal for thermoelectric device or high-power applications.

AlN/TiN multilayer is one of the most promising systems due to high hardness, enhanced radiation tolerance, and thermal stability [31, 74]. Depending on layer thickness and microstructure, the boundary scattering and grain scattering of heat carrier

have been studied as the subject of intense experimental and theoretical investigations during the past twenty years [20, 22, 75-79]. Kuo *et al.*[80] measured thermal conductivity of AlN single layer on various substrates and compared microstructure effect on thermal conductivity without size effect. Single layered AlN and TiN films also have been studied for thermal conductivity with various thicknesses down to ~100 nm [81, 82]. In micro regime of thermal transport property, however, the size effect is dominant for heat carrier scattering, such as surface boundary scattering that reduces mean free path of carrier significantly, and ultra-thin film (~10 nm or less) is necessary to be investigated especially in superlattices [76, 83].

In the multilayer film, the thermal conductivity of the embedded layer has not only the classical size effect such as diffusive boundary scattering but also the effect of partial phonon spatial confinement due to the partial reflections and transmissions of lattice waves at the layer boundary with dissimilar elastic properties. Zou *et al.*[12] theoretically described that the effect of partial phonon confinement leads to a higher thermal conductivity of the embedded GaN layer in an AlN/GaN/AlN heterostructure than that in a single GaN thin film with the same total structure thickness. Costescu' group measured thermal conductance of interfaces between epitaxial TiN and single crystal oxides, such as TiN/MgO(001), TiN/MgO(111), and TiN/Al_2O_3(0001) at temperatures between 79.4 and 294 K by applying the time-domain thermoreflectance (TDTR) method [23]. They did not observe significant differences in the thermal conductance for the three TiN interfaces. In particular, the 8% in-plane lattice mismatch between TiN(111) and Al_2O_3(0001), and the interface stacking faults in the

TiN/MgO(111) and TiN/Al_2O_3 samples, did not modify the thermal transport significantly. Interfacial point defects and misfit dislocations may not significantly affect thermal boundary conductance [23].

In this study, we present experimental investigation of the thermo-physical property, which is the effective thermal conductivity of the embedded AlN nanolayer in TiN/AlN/TiN system and the intrinsic thermal conductivity of TiN nanolayer with size effect and microstructure effect. The thickness of embedded AlN nanolayer was varied from 8 nm to 2 nm within the system. In addition, TiN ultra-thin films were studied for intrinsic thermal conductivity in various thicknesses. AlN can be grown in two crystal phases such as cubic and hexagonal, which are zinc-blende structure and wurtzite structure, respectively. With high and room temperature deposition condition the epitaxial cubic phase and poly crystalline phase AlN nanolayers were prepared and studied for microstructure effect on the effective thermal conductivity.

A detailed microstructural study was conducted to characterize crystal phases and interfacial microstructures of AlN and TiN nanolayers. Then, the through-plane intrinsic thermal conductivity of TiN and effective thermal conductivity of AlN nanolayers were measured by using a non-contact, non-invasive, in-situ Transient Thermo-Reflectance (TTR) laser based technique.

5.3 Experimental details

TiN/AlN/TiN films were prepared with the PLD method for thermo-physical property measurement with two parameters; one is thickness of AlN layer and the other is microstructure of nanolayer. The thicknesses of embedded AlN layers are approximately 2, 4 and 8 nm between 10 - 15 nm TiN layers. The TiN/AlN/TiN nanolayer was deposited on 25 nm TiN buffer layer as shown in Fig. 5.1(c) and the deposition temperatures were 700 °C and room temperature to fabricate cubic structure and polycrystalline microstructures of the films, respectively. The TiN/TiN and AlN/TiN samples in Fig. 5.1(a) and (b) were fabricated to measure the intrinsic thermal conductivity of TiN layer and the effective thermal conductivity of AlN and TiN layers.

Microstructure of the films was studied XTEM and HRTEM, and then gold layer was deposited on the films by using sputter system to apply TTR method for thermal property measurement. The optical properties of the gold layer were measured by using Gaertner Ellipsometer. A Dektak^{3}ST profilometer was employed to measure the thickness of the sputter-coated Au layers on the films by using the created step in the layer. An Au/silicon substrate sample was used to measure ρC_p of the Au layer. These geometry and optical properties were used in the numerical simulation of the transient temperature response to get thermal conductivity of a layer.

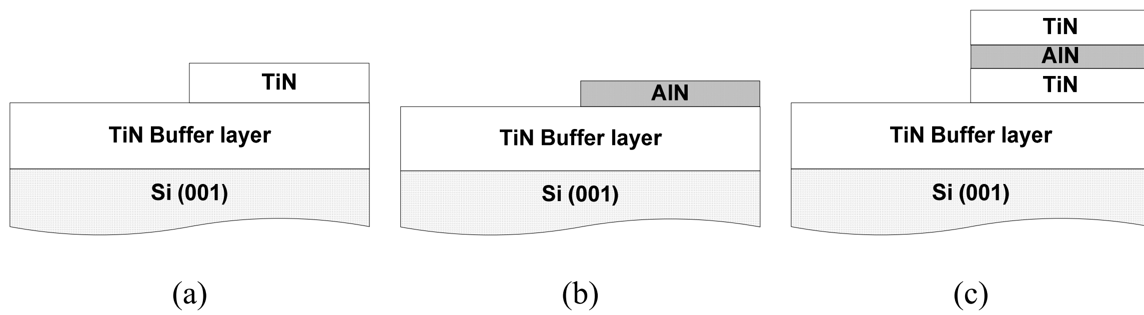

Fig. 5.1 Schematic cross-section of sample with applied TTR measurement: (a) TiN single layer, (b) AlN single layer, and (c) embeded AlN layer with various thicknesses between TiN layers on TiN Buffer layer

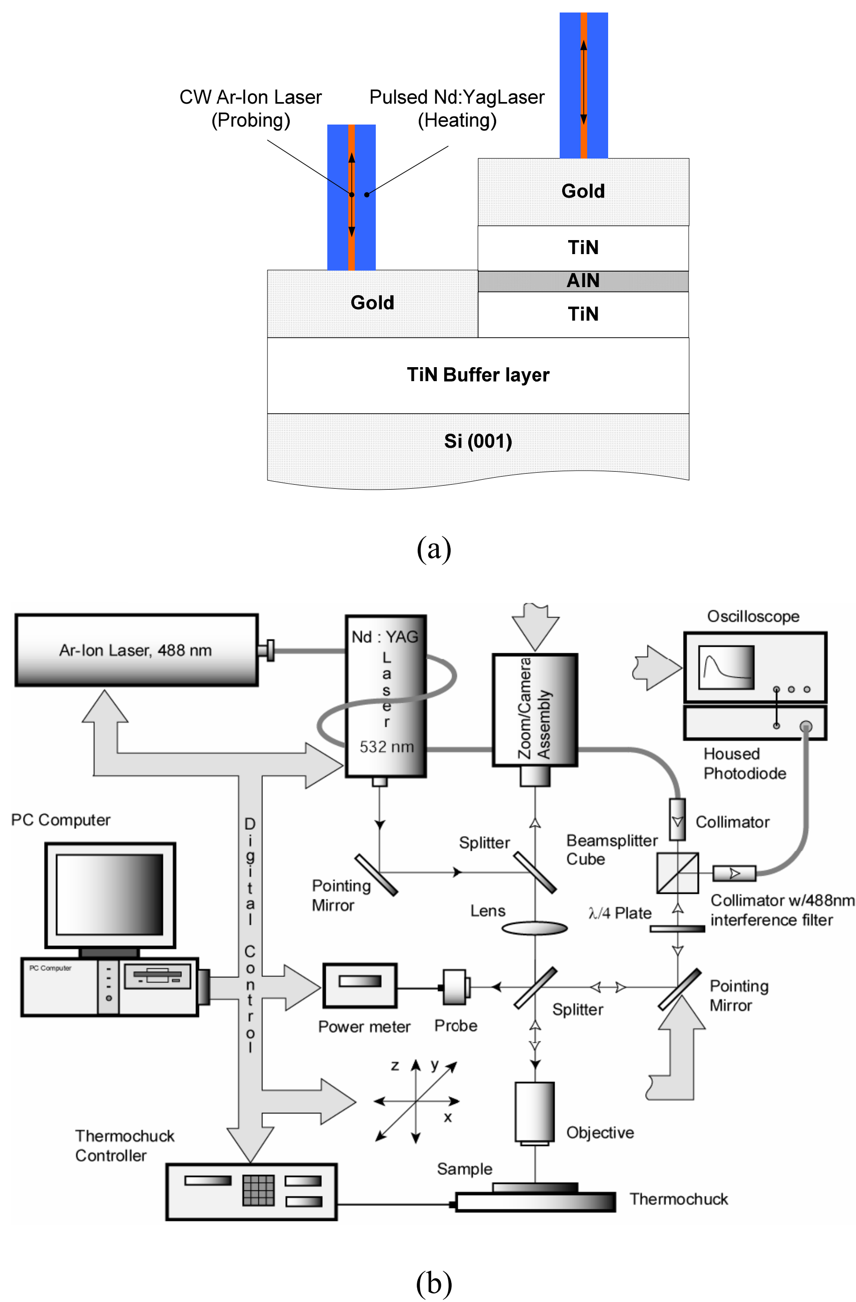

(b)

Fig. 5.2 (a) Schematic of gold deposited TiN/AlN/TiN sample to apply TTR method and (b) Schematic of the Transient Thermo-Reflectance (TTR) System in NETSL at SMU by Burzo et al.[44]

The TiN/AlN/TiN samples were tested using the TTR setup (Fig. 5.2) to find the transient surface temperature for thermal conductivity. First, intrinsic thermal conductivities of TiN depending on the layer thickness and the microstructure were measured on TiN single layer areas of samples, and then effective thermal conductivities of the embedded AlN layer were measured depending on the layer's thickness and also the microstructure as shown in Fig. 5.2(a).

Figure 5.2(a) depicts schematically the heating and probing beams on a sample used in the Transient Thermo-Reflectance system of Fig. 5.2(b). In the system built in the Nanoscale Eletro-Thermal Sciences Laboratory at SMU, the heating source is an Nd: YAG laser, that is pulsed at 30 Hz with a wavelength of 532 nm, maximum output pulse energy of 0.5 mJ/pulse, and a pulse-width of 6.1 ns. The probing light source is a CW Ar-Ion laser with a wavelength of 488 nm in a single-mode irradiation and maximum output of 25 mW. The amount of heating energy used from the heating source was 25.71 μJ/pulse which was measured directly by a power meter and the fluence was 957 J m^{-2} for the samples measured.

Next, the acquired TTR temperature response is matched by the solution of the heat equation by varying the thermal resistance caused by the film, R_{th}. It should be mentioned that the TTR technique measures the thermal diffusivity of the material rather than the thermal resistance of the film. Therefore, the thermal capacitance and the film thickness are important values to reduce uncertainty of total thermal resistance.

5.4 Results and discussion

All fabricated samples were examined by XTEM to study the microstructure and to measure each layer thickness. Depending on deposition temperature, 700 °C and room temperature, the structure was evidently different from each other. At high temperature, both of TiN and AlN had cubic structure, but the structures were polycrystalline at room temperature deposition.

XTEM images with selected area diffraction (SAD) pattern of TiN/AlN/TiN nanolayer films are shown in Fig. 5.3 for high temperature deposition (a,b, and c) and room-temperature deposition (d, e, and f) specimens. The dark contrast layer is TiN and bright one is AlN layer. When the samples were fabricated, approximately 25 nm TiN was deposited on all area of substrate. Then, the TiN/AlN/TiN nanolayer was deposited on the buffer layer after covering half-surface area with cleaned silicon wafer as shadow-mask. It is hard to distinguish the interface between TiN buffer layer and TiN nanolayer in high temperature, and moreover the SAD patterns of the high temperature deposited samples shows cubic structure in both of TiN and AlN nanolayers. As the diffraction ring implies, however, the samples deposited at room temperature had the expected polycrystalline structure in TiN and AlN nanolayers as shown in Fig. 5.3. The thermal conductivity of cubic AlN would be higher than that of hexagonal AlN because cubic phase has fewer number of optical phonon branches. Thus, these samples are enough to compare microstructure effect on thermal conductivity in TiN and the embedded AlN nanolayers.

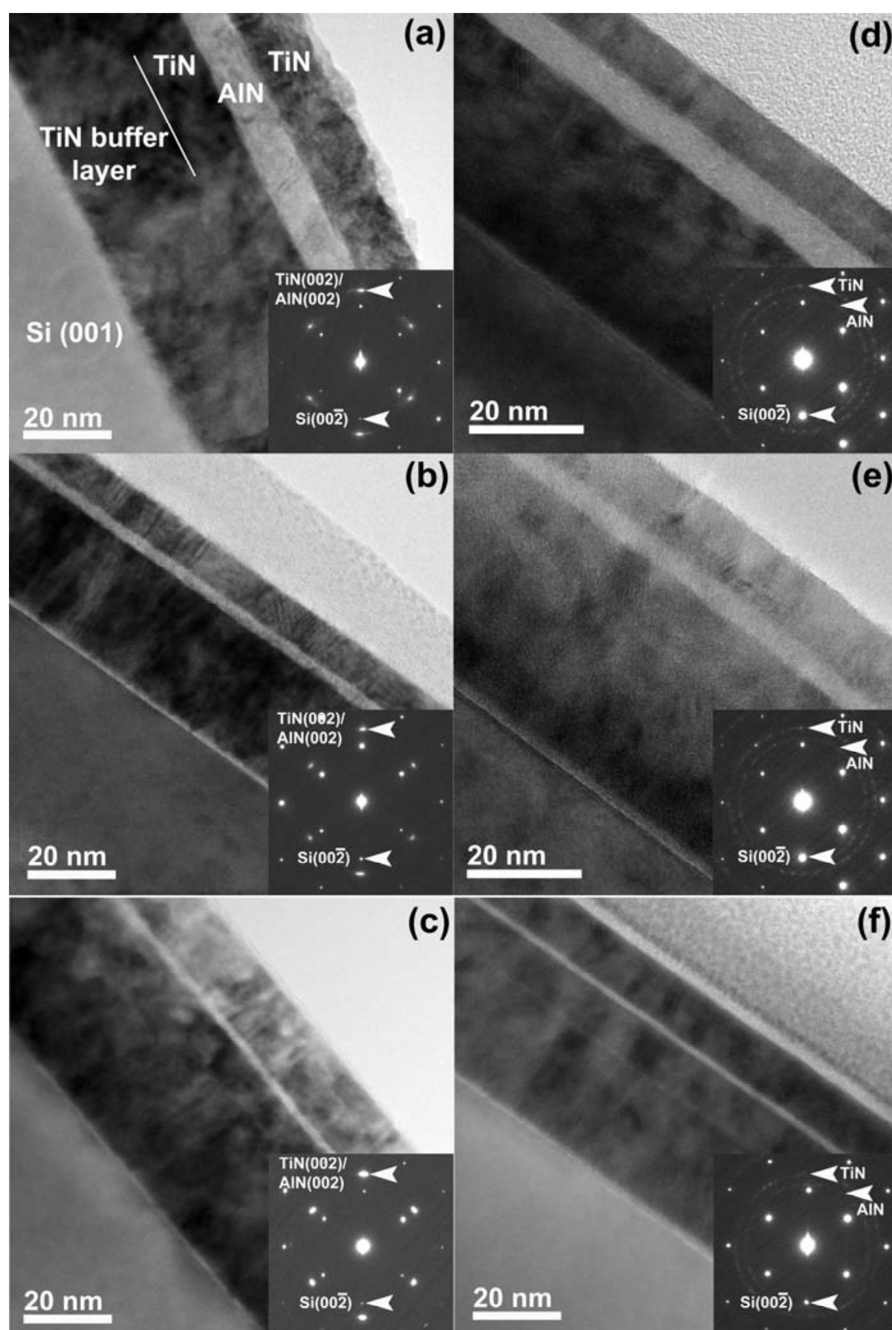

Fig. 5.3 Cross-sectional TEM images with selected diffraction patterns of embeded AlN layer with various thicknesses (8 nm, 4 nm, and 2 nm) between TiN layers on TiN Buffer layer: Embedded epitaxial cubic AlN (a, b, and c) and poly-crystalline AlN (d, e, and f) in TiN layers

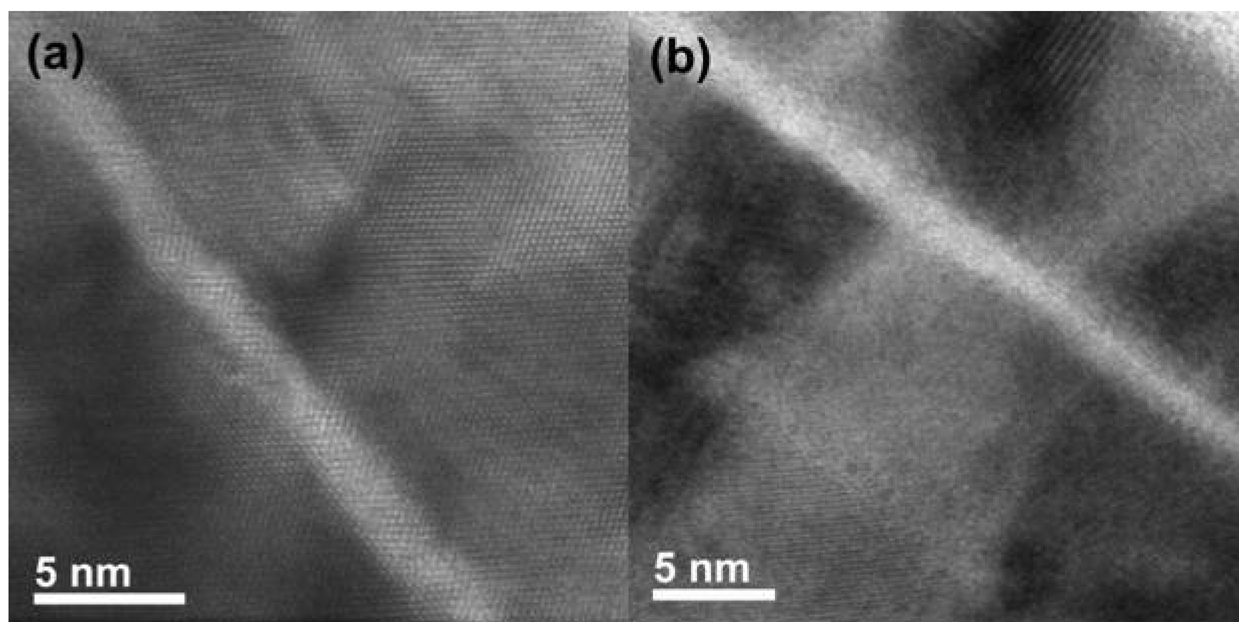

Fig. 5.4 HR TEM images of 2 nm (a) epitaxial cubic AlN and (b) polycrystalline AlN layers

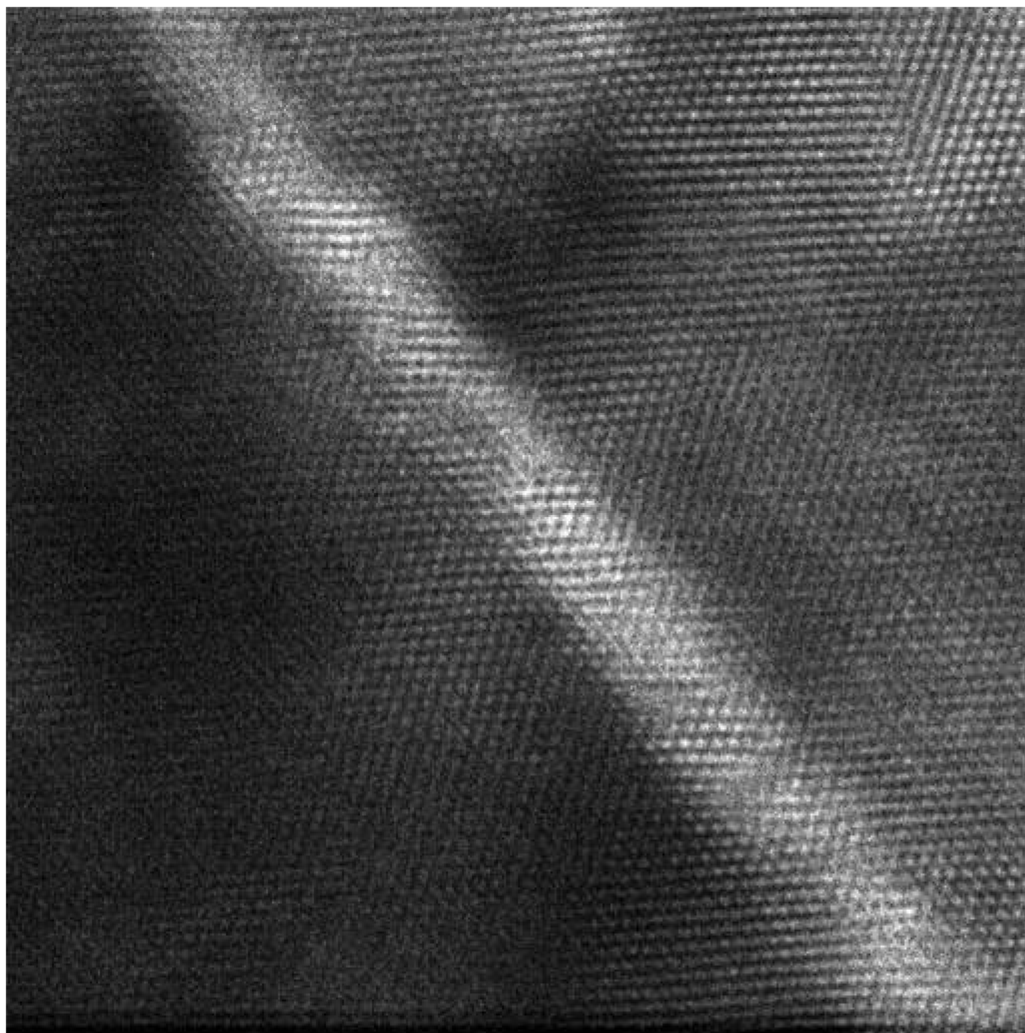

Fig. 5.5 HR TEM images of 2 nm epitaxial cubic AlN layer that noise filtered by Fast Fourier Transform (FFT)

Detailed HRTEM study compared the microstructures as shown in Fig. 5.4. The epitaxial growth of each nanolayer at high temperature sample is shown in Fig. 5.4 (a) and it is evidently distinguished from the room-temperature deposited sample, Fig. 5.4 (b). The high temperature deposited films showed epitaxial growth of TiN and AlN nanolayers with cubic structure. Using Fast Fourier Transform (FFT) on the higher resolution image of the epitaxial TiN/AlN/TiN layer, it shows the epitaxially grown lattices in the embedded AlN and the interfaces of the 2 nm cubic AlN layer as shown in Fig. 5.5.

During TEM study, the thicknesses of all layers in samples were measured. To measure the effective thermal conductivity of the embedded AlN nanolayer, it is needed to measure intrinsic thermal conductivity of TiN single layer with various thicknesses before studying the multilayer. Experimental investigations for the size effect on thermophysical properties in dielectric or metallic materials have been reported in micro- and nano-size regime [22, 75]. Because heat carriers such as electrons and phonons in metallic and dielectric materials, respectively, are influenced by the "size effect" in micro-scale dimensions, the boundary scattering of carrier is dominant in sub-100 nm thickness. In addition, all TiN nanolayer thicknesses in the multilayer systems are less than 50 nm, thus the intrinsic thermal conductivity of TiN nanolayer was measured on various thick TiN single layer samples that ranged from 41 nm to 9 nm. In order to apply TTR method, the properties of top gold layer were studied as Table 5.1.

Table 5.1 Thermal and optical properties of the Au layer deposited on samples

K ($Wm^{-1}K^{-1}$)	ρC_p ($Jm^{-3}K^{-1}$)	α (m^2s^{-1})	k	h (m)	Δ_L (m)	δ_H (m)
315	2.31×10^{6}	1.36×10^{-4}	2.45	$0.6 - 0.7\times10^{-6}$	1.73×10^{-8}	0.91×10^{-6}

The mass density and specific heat of silicon, TiN, AlN and gold are well known in bulk dimensions. However, thermal capacitance ρC_p of the deposited gold may be various depending on deposition condition and method. Thus, the ρC_p of gold layer on silicon wafer was measured by TTR system and the value was used for the other samples in TTR system. The measured average ρCp for the Au layer was 2.31×10^{6} J m^{-3} K^{-1} and it was utilized for all TTR measurements of all the samples in this work.

Using the above properties for the Au layer, the light penetration depth, (ΔL), and heat propagation depth, δH, were calculated as follows:

$$\Delta_L = \frac{\lambda}{4\pi k} \tag{5.1}$$

$$\delta_H = (\alpha\,\tau)^{\frac{1}{2}} \tag{5.2}$$

where λ is the wavelength of the laser, δ_H is the heat propagation depth during the heating pulse, and τ is the pulse width of the heating laser. Thus, the light penetration depth and the heat penetration depth can be compared with the thickness of the top Au

layer, which is the absorption layer for the heating laser. The light penetration depth and the heat propagation depth caused by the pulsed laser were calculated as of 17.3 nm and 940 nm for the deposited Au layer, respectively as shown in Table 5.1. The thickness of Au layers in the samples are ranged between 600 nm and 700 nm that are enough for the pulsed heat to propagate into the top TiN/AlN/TiN layers with considering the heat propagation depth (940 nm) in Au layer.

According to a previous work by Burzo *et al.*[84] and Komarov and Raad [85], the heat penetration depth in the absorption layer should be comparable to the specified layer thickness range as defined by the nondimensional thickness, H:

$$H = \frac{h}{\sqrt{\alpha\tau}} = \frac{h}{\delta_H} = \frac{1}{\sqrt{Fo}} \tag{5.3}$$

where F_o is the Fourier number defined as $F_o=\alpha\tau/h2$. The terms “thermally thin”, “thermally thick”, and “transition regime” were defined and it was shown that the responsivity of the TTR measurements for measuring the thermal conductivity of the underlying bulk silicon dioxide ($K \approx 1.4$ W m^{-1} K^{-1}) and bulk silicon sample ($K \approx 148$ W m^{-1} K^{-1}) is sufficiently high within the thickness of the absorption layer that is the transition regime ($0.4 \leq H \leq 2$), and more widely, in the regime ($0.1 \leq H \leq 2$) [84, 86].

On the other hand, thicker layers ($H \geq 2$) would hide the influence of thermal properties of any underlying material. As results, it was chosen to deposit Au layers with thickness ranging between 400 nm and 800 nm onto the all films. The thickness of the

deposited Au film, h, was within the intervals $\Delta L << h < \delta H$ and $0.66 \leq H \leq 0.77$. Although the thermal conductivity of TiN or AlN film may be less than that of silicon dioxide by approximately one order of magnitude due to the size effect, the nondimensional thickness of Au layer in the range $0.66 \leq H \leq 0.77$ corresponds to a sufficiently high responsivity for measuring the thermal conductivity of the embedded AlN layer and each single films.

The thermal conductivity was measured at three different locations in the immediate vicinity of the area measured for the gold thickness, and was measured twenty times at each position. Each of the twenty measurements in a given position consisted of 1000 shots using the heating laser and each TTR measurement was performed using the probing laser for a single heating shot. On the other hand, each of the twenty averaged values in a position was an average of the 1000 TTR measurements. Thus, one position had a total of twenty average values for the 20×1000 heating shots in the TTR measurement. The dimensions for the heating and probing spot, using a 20× objective lens, (YAG Laser) were 185 μm and 2.5 μm, respectively, thus the ratio of spot diameters was 74. This value ensures that the 1-D heat equation, Eq. (2.16)

$$\left(\frac{\partial T}{\partial t}\right) = \alpha\left(\frac{\partial^2 T}{\partial z^2}\right) + \frac{1}{\rho C_p}\dot{Q}_{ab}(z,t) \tag{2.16}$$

assumption can be used instead of the 2-D expression, Eq. (2.13).

$$\left(\frac{\partial T}{\partial t}\right) = \alpha(T)\left(\frac{\partial^2 T}{\partial r^2} + \frac{1}{r}\frac{\partial T}{\partial r} + \frac{\partial^2 T}{\partial z^2}\right) + \frac{1}{\rho C_p}\dot{Q}_{ab(r,z,t)} \qquad (2.13)$$

where r and z are dimensionless coordinates and α is the thermal diffusivity of the material, which is $\alpha = K/(\rho C_p)$.

Finally, the samples, which consisted of an Au layer and TiN/AlN/TiN nanolayer and each TiN nanolayer deposited on the silicon wafers, were tested using the TTR experimental system. These measurements used the unknown parameters, namely, the intrinsic thermal conductivity (K_{int}) of the TiN film, the effective thermal conductivity (K_{eff}) and an interface thermal resistance (R_{I1}) between the Au layer and the film.

Table 5.2 is the properties that used to measure the intrinsic thermal conductivity of TiN films by TTR method. Two unknown values, K_{int} and R_{I1}, were measured for all TiN samples. Once the transient TTR temperature response was obtained from measuring the relative change in the reflectivity of the samples, the data was fitted with the numerically obtained transient temperature signal. The numerical simulation of the transient temperature response was computed from the solution of the heat equation by using the thermo-physical properties of the materials composing the samples.

Table 5.2 Properties of the samples utilized in the TTR system

Materials	ρCp ($Jm^{-3}\,K^{-1}$)	K ($Wm^{-1}K^{-1}$)	n	k	h (Å)	R_I ($10^{-8}\,m^2KW^{-1}$)
Si Substrate	1.63×10^6	148	–	–	4,800,000	negligible
TiN	3.14×10^6	unknown†	–	–	measured data*	0.1 (R_{I2})
Au	2.31×10^6	315	0.467	2.45	measured data**	unknown (R_{I1})†

* measured film thickness by TEM study

** measured gold layer thickness by Dektak3ST profiler

† value that will be measured by TTR system

The interface thermal resistance R_{I2} between TiN layer and silicon substrate was 0.1×10^{-8} $m^2\,KW^{-1}$ and the interface thermal resistance R_{I1} between TiN and gold layer was up to 1.7×10^{-8} $m^2\,KW^{-1}$ that is relatively high interface resistance. It is because the contact adhesion is not good between TiN and gold. The intrinsic thermal conductivity of TiN depending on layer thickness is shown in Fig. 5.6. The maximum thermal conductivities are 9.62 W $m^{-1}K^{-1}$ and 8.01 W $m^{-1}K^{-1}$ at 41 nm thick epitaxial TiN and at 38 nm polycrystalline TiN, respectively. These values are continuously decreased down to 5.97 W $m^{-1}K^{-1}$ and 4.59 W $m^{-1}K^{-1}$ at 9 nm thick epitaxial TiN and polycrystalline TiN, respectively, with decreasing thickness. The estimation of uncertainty values was based

on the analysis developed by Kline and McClintock [46] with a confidence level of 90% (or 20:1 odds). The method was based on the uncertainties in the primary measurements, such as the thickness measurements of the film and the Au layer, and then, the uncertainty for the thickness of each layer was considered for the uncertainty of thermal conductivity in the TTR measurement

It is well known that a bulk TiN has intrinsic thermal conductivity as of 28.84 W $m^{-1}K^{-1}$ at room temperature [87]. Comparing bulk TiN the thin film of TiN had obvious thickness dependence on intrinsic thermal conductivity property. The K_{int} was decreased with decreasing the layer thickness that ranged from 40 nm to 9 nm for both of epitaxial crystalline and polycrystalline TiN films. It must be due to the "size effect" in the thin film. Thermal conductivity of 300 nm thick TiN film was reported as 15 W $m^{-1}K^{-1}$ at room temperature by using 3ω method [88] and it was 15.16 W $m^{-1}K^{-1}$ in our measurement at 282 nm thick TiN film by using TTR method.

In addition, the K_{int} of polycrystalline TiN was lower than that of epitaxial TiN in that range. The smaller grain size in polycrystalline TiN induces carrier scattering that results in lower thermal conductivity. As shown in Fig. 5.6, the difference of K_{int} between epitaxial- and poly-crystalline structures is almost constant in that range. It means that the grain boundary effect on carrier scattering is still significant as well as surface boundary scattering in the thickness range. The grain size is always larger than the mean free path of the energy carriers, such as phonons and electrons.

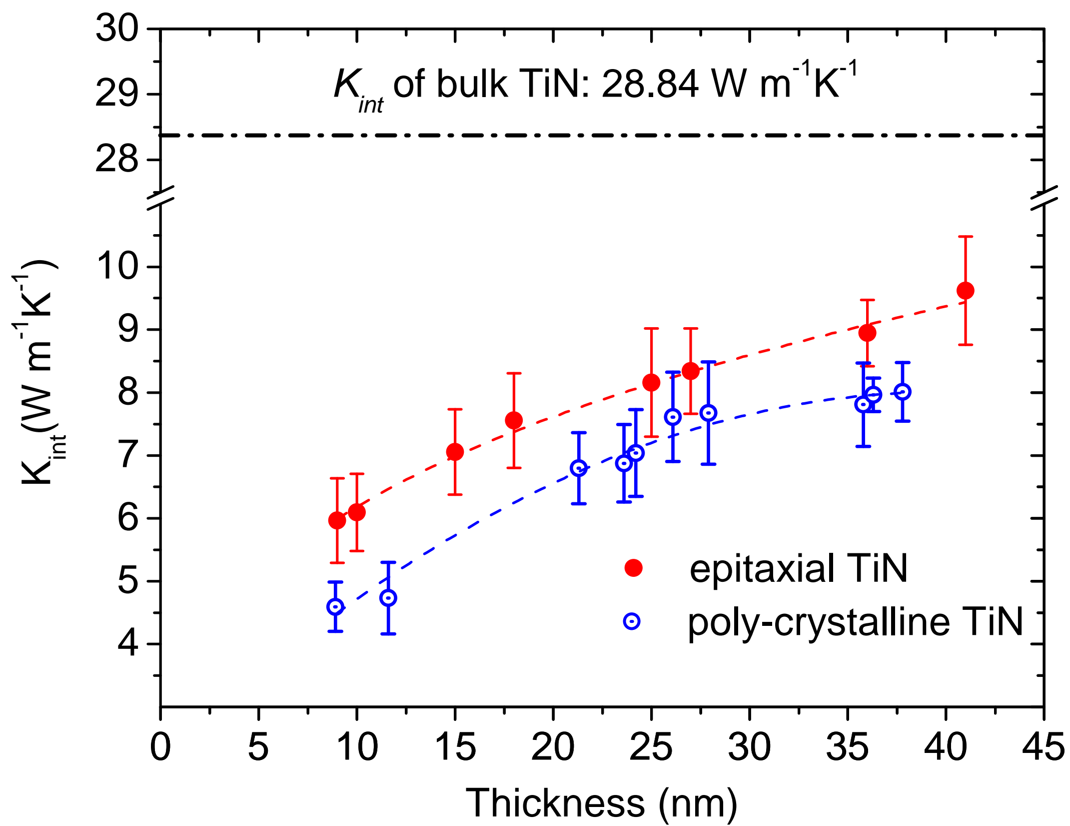

Fig. 5.6 Measured intrinsic thermal conductivities (K_{int}) of TiN single layers depending on thickness and crystal structure

Feng *et al.* reported that the electron carrier grain-boundary scattering exhibits a substantial contribution to the size effect in metal films, such as gold, copper, and aluminum films [79]. In addition, there is influence of phonon on thermal conductivity in metals even if the portion is relatively small in metal. In a single-crystalline copper film, they showed that lattice contribution to the total thermal conductivity is much smaller than electron [78]. However, TiN (over 20 μm thickness) film has high elastic modulus as 320 GPa [89] with relatively high longitudinal acoustic velocity as 9580 m/s, which is much higher than copper [78, 90]. Thus, the lattice contribution to thermal conductivity in TiN film would be higher than that in the metal material.

The measured intrinsic thermal conductivity at each thickness were used in TTR method to measure effective thermal conductivity of the embedded AlN layers. The effective thermal conductivity includes interface thermal resistance between AlN and the clamped TiN layers; however, the interface resistance is very small amount comparing with the both of TiN and AlN layers especially in the epitaxial film. Properties of each layers that used in TTR system for the embedded AlN layer are shown in Table 5.3.

The two unknown values, K_{eff} and R_{I1}, of the embedded AlN layer were measured on three TiN/AlN/TiN samples of each high temperature and room temperature deposited samples. The two interface thermal resistances between AlN and TiN layers are included in the effective thermal conductivity of AlN by ignoring the separated interface resistances, and the unknown K of AlN was measured as the effective thermal conductivity. The other layer thicknesses and intrinsic thermal conductivity of TiN layers were measured in previous step.

Table 5.3 Properties of the samples utilized to measure thermal property of the embedded AlN by TTR system

Materials	ρCp ($Jm^{-3} K^{-1}$)	K ($Wm^{-1}K^{-1}$)	n	k	h (Å)	R_I (10^{-8} m^2KW^{-1})
Si Substrate	1.63×10^6	148	–	–	4,800,000	negligible
TiN	3.14×10^6	measured data ***	–	–	measured data*	0.1 (R_{I2})
AlN	2.42×10^6	unknown†	–	–	measured data*	negligible
TiN	3.14×10^6	measured data ***	–	–	measured data*	negligible
Au	2.31×10^6	315	0.467	2.45	measured data**	unknown (R_{I1})†

* measured film thickness by TEM study

** measured gold layer thickness by Dektak3ST profiler

*** value that was measured by TTR system

† value that will be measured by TTR system

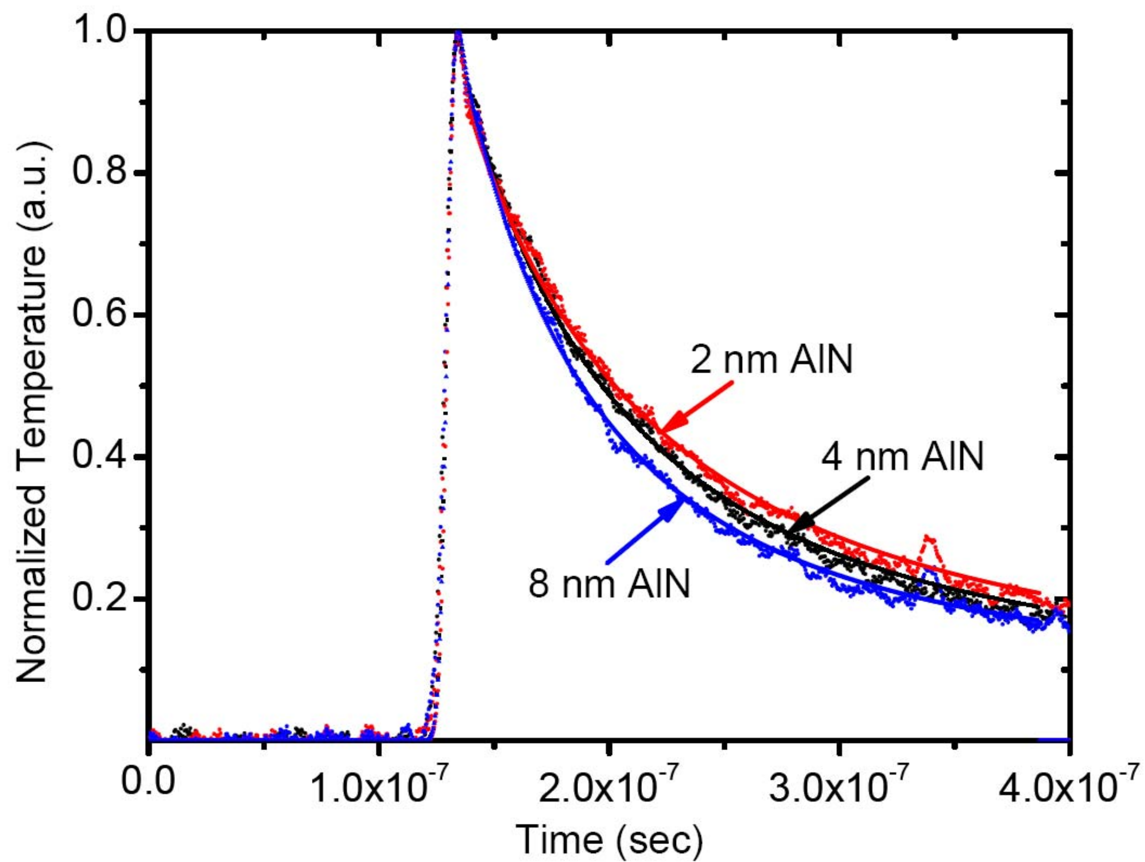

Fig. 5.7 Normalized TTR response and the matched numerical response within 1.5% error for embedded AlN layers: 1.8 nm, 2.8 nm, and 8.8 nm epitaxial cubic AlN layers

The normalized TTR temperature responses obtained for the embedded AlN layer in three high temperature deposited TiN/AlN/TiN samples are shown in Fig. 5.7. Each TTR response curve consists of 1000 transient temperature responses as normalized temperature versus time. The maximum normalized temperatures in the samples were detected at 134 – 135 ns and the top Au layers started to cool after that time-period. The three samples, which have the embedded AlN layer with thickness as 1.8 nm, 2.8 nm and 8.8 nm, showed indistinguishable slope during the cooling process. Meanwhile, an apparent change of the normalized temperature response was found in the samples. For instance, the ultra-thin (1.8 nm) AlN layer sample showed slower temperature reduction than that of the other samples in the cooling process. The matched numerical temperature response to each experimental response of the three samples were obtained by varying the material thermal diffusivity in the numerical simulation until the numerical curve fits the experimental result within a 1.5% error.

The measured effective thermal conductivities of AlN layers were plotted for both of epitaxil and poly-crystalline sample as shown in Fig. 5.8. As the film thickness decreased, a decrease in the through-plane effective thermal conductivity was observed for both of crystalline samples. The average value reached 1.70 W m^{-1} K^{-1} at a thickness of 1.8 nm and 0.78 W m^{-1} K^{-1} at a thickness of 1.4 nm in epitaxial and poly-crystalline embedded AlN layers, respectively.

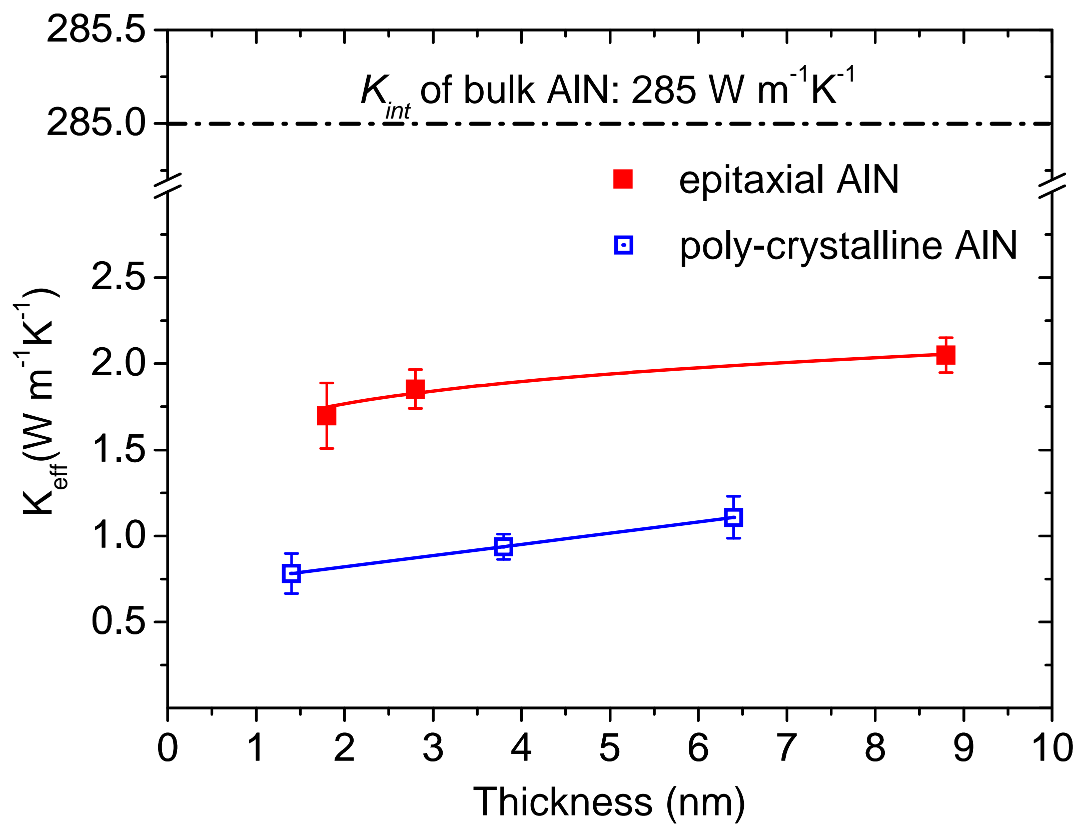

Fig. 5.8 Effective thermal conductivity (K_{eff}) of embedded AlN layers depending on layer thickness and crystal structures

As shown in Fig. 5.8, the epitaxial AlN has cubic phase and the measured effective thermal conductivity is higher than poly-crystalline AlN, which has mainly hexagonal phase in the thickness range. Depending on the phase, the crystalline AlN has higher thermal conductivity due to the longer mean free path of phonon[91, 92]. The embedded epitaxial cubic AlN has 2.05 $Wm^{-1}K^{-1}$, 1.85 $Wm^{-1}K^{-1}$, and 1.70 $Wm^{-1}K^{-1}$ at 8.8 nm, 2.8 nm, and 1.8 nm, respectively, and the polycrystalline AlN has 1.11 $Wm^{-1}K^{-1}$, 0.94 $Wm^{-1}K^{-1}$, and 0.78 $Wm^{-1}K^{-1}$ at 6.4 nm, 3.8 nm, and 1.4 nm, respectively. The error bar shows uncertainty based on a confidence level of 90%. These measured values include two interface thermal resistances between the embedded AlN and the cladding TiN layers (top and bottom). Polycrystalline AlN has much lower K_{eff} than that of epitaxial AlN in the thickness range similar to epitaxial and polycrystalline TiN film. There would be two main influences, which are crystal phase and grain size of film and interface thermal resistance.

Based on the kinetic theory K=1/3 (C υ λ) and acoustic phonon branches, it was theoretically reported that the lattice thermal conductivity K of cubic AlN will have approximately 2.7 times that of hexagonal AlN at room temperature and above [91]. This result clearly suggests that AlN would be a far better high thermal conductivity material when grown in its cubic phase than in its hexagonal phase. Thermal conductivity of AlN has been studied at various temperature with comparing different grain-sized AlN [13, 91-93]. AlShaikhi *et al*.[91] theoretically predicted that at room temperature and above, the average phonon mean-free path for the cubic-AlN (zinc-blende phase) is approximately four times that for the hexagonal-AlN (wurtzite phase).

In addition, the reported high thermal conductivity of AlN is 319 $Wm^{-1}K^{-1}$ at room temperature as bulk sized pure AlN [32]. Watari *et al.* measured the thermal conductivity of high purity single crystal AlN (bulk sized) at temperatures between 4 and 1000 K and the value at 300K was 285 $Wm^{-1}K^{-1}$ and the calculated average phonon–phonon scattering distance is about 70 nm at 300K [13]. However, depending on the crystal phase it is also reported as 30.1 $Wm^{-1}K^{-1}$ in bulk AlN [87].

In thin films, the reported thermal conductivity values of thin AlN films were typically orders of magnitude lower than the corresponding bulk materials. Kuo *et al.*[80] measured the intrinsic thermal conductivity of AlN thin films on various substrates including Si(111) and Si(001) substrates. The textured film thickness was 1 μm on all substrates and the thermal conductivity was 0.48-0.82 $Wm^{-1}K^{-1}$, 1.5 $Wm^{-1}K^{-1}$, 25.2 $Wm^{-1}K^{-1}$ and on Si(111), Si(001), and Al_2O_3(1T02), respectively. The substrate decides structure phase of deposited film such as hexagonal phase of AlN on Si(111). Even if including the two interface resistances of AlN and TiN layers, their measured K_{int} of AlN on Si substrates is lower than K_{eff} of the embedded epitaxial cubic AlN on TiN layer in this study. There would be the grain-size effect as well as structural phase effect on the phonon scattering due to it would not a single crystalline. On the contrary, the K_{int} of AlN on Al_2O_3 is much higher than that of the epitaxial cubic AlN that measured in this study. It must be due to the surface boundary scattering of phonon by the different thickness.

As shown in Fig. 5.8, the through-plane K_{eff} of polycrystalline AlN decreased faster than that of epitaxial cubic AlN layer with decreasing layer thickness. The

polycrystalline AlN has approximately a K_{eff} reduction rate of 0.13 $Wm^{-1}K^{-1}$ /nm, which is 29% reduction of K_{eff} during decreasing thickness from 6.4 nm to 1.4 nm. On the other hand, the embedded epitaxial cubic phased AlN showed a K_{eff} reduction rate of 0.05 $Wm^{-1}K^{-1}$ /nm only, which is 17% reduction of K_{eff} during decreasing thickness from 8.8 nm to 1.8 nm. We did not observe increased K_{eff} in that thickness range; however, the decreasing slop of K_{eff} in the epitaxial cubic AlN is almost constant within the range from 8.8 nm to 2.8 nm. The K_{eff} of the epitaxial cubic AlN is even higher than K_{int} of AlN single layered films, which have 1 µm [80] or 200 nm [81] thick layers.

It would be lattice confinement effect on thermal conductivity by cladding TiN layers [12]. Choi *et al.*[81] studied the sized effect on thermal conductivity of AlN thin film with varying the thickness in the range from 200 nm to 2000 nm at room temperature deposition. Their measured thermal conductivity of the AlN thin film decreases rapidly as the film thickness decreased, such as 1.83 $Wm^{-1}K^{-1}$ and 32.3 $Wm^{-1}K^{-1}$ at 200 nm and 500 nm, respectively [81]. They used Si(001) substrate for the AlN layers, thus the deposited AlN would be hexagonal phase or polycrystalline.

Considering one interface between AlN and TiN layers, the effective thermal conductivity of AlN on TiN layer was measured on AlN/TiN samples that were deposited at 700 °C and room temperature on Si(001). The K_{eff} that includes one interface resistance were 1.96 $Wm^{-1}K^{-1}$ on epitaxial AlN and 1.51 $Wm^{-1}K^{-1}$ on polycrystalline AlN at 3.8 nm and at 5.5 nm. Comparing with the plots in Fig. 5.8, these values are higher than the each plots of the embedded epitaxial and polycrystalline AlN. It means that the intrinsic thermal conductivity K_{int} of the embedded AlN is higher than

K_{eff} of the AlN and the interface resistance in polycrystalline is also higher than epitaxial growth. For the more study, it is needed to study the intrinsic thermal conductivity of single nanolayer AlN film with the two phases of cubic and polycrystalline in the ultra-thin thickness regime.

In this study, we successfully fabricated the embedded epitaxial cubic AlN and polycrystalline AlN with cladding TiN layers. In addition, single layered epitaxial and polycrystalline TiN films with various thicknesses were prepared at 700 °C and room temperature. Microstructure and thermal transport properties of the films have been experimentally investigated for crystal phase and size effects in the TiN single layer and the three-layered TiN/AlN/TiN films. The through-plane intrinsic thermal conductivity K_{int} was significantly decreased from 9.6 $Wm^{-1}K^{-1}$ at 41 nm down to 6.0 $Wm^{-1}K^{-1}$ at 9 nm thick epitaxial TiN film by surface boundary scattering of heat carrier. In addition, polycrystalline TiN film showed thermal conductivity drop that is from 8.0 $Wm^{-1}K^{-1}$ at 38 nm down to 4.6 $Wm^{-1}K^{-1}$ at 9 nm, which is influenced by additional grain boundary scattering of carrier.

5.5 Summary

Thin TiN films and three-layered TiN/AlN/TiN nanolayers have been experimentally investigated for crystal phase and size effects on thermal property of the polycrystalline and epitaxial cubic TiN single layer and the embedded AlN layer in the films. The through-plane intrinsic thermal conductivity K_{int} was significantly decreased

from 9.6 $Wm^{-1}K^{-1}$ at 41 nm down to 6.0 $Wm^{-1}K^{-1}$ at 9 nm thick epitaxial TiN film by surface boundary scattering of heat carrier. In addition, polycrystalline TiN film showed thermal conductivity drop that is from 8.0 $Wm^{-1}K^{-1}$ at 38 nm down to 4.6 $Wm^{-1}K^{-1}$ at 9 nm, which is influenced by additional grain boundary scattering of carrier.

Depending on phase of the embedded AlN by cladding TiN, the epitaxial cubic AlN showed higher effective thermal conductivity than that of polycrystalline AlN in the thickness ranged from 10 nm down to 2 nm. The through-plane K_{eff} of polycrystalline AlN decreased faster than that of epitaxial cubic AlN layer with decreasing layer thickness. The polycrystalline AlN has approximately a K_{eff} reduction rate of 0.13 $Wm^{-1}K^{-1}$ /nm, which is 29% reduction of K_{eff} during decreasing thickness from 6.4 nm to 1.4 nm. On the other hand, the embedded epitaxial cubic phased AlN showed a K_{eff} reduction rate of 0.05 $Wm^{-1}K^{-1}$ /nm only, which is 17% reduction of K_{eff} during decreasing thickness from 8.8 nm to 1.8 nm. We did not observe increased K_{eff} in that thickness range; however, the decreasing slop of K_{eff} in the epitaxial cubic AlN is almost constant within the range from 8.8 nm to 2.8 nm.

The result shows that grain boundary scattering of phonon and the phase of structure effect on thermal conductivity are still dominant in the ultra-thin nanolayer regime as well as the surface boundary scattering of phonon. The embedded epitaxial cubic AlN experienced the suppressed size effect, which reduces the amount of decrease in through-plane thermal conductivity. The minimum effective thermal conductivity of the embedded c-AlN with 2 nm thickness was higher than that of single layered c-AlN reported. It confirms the phonon confinement effect in multilayer as well as the

importance of film thickness, interface and microstructure for material properties in nanolayers.

CHAPTER VI

TiN-BASED COATINGS FOR FUEL CLADDING TUBES

6.1 Overview

Titanium nitride that serves as effective diffusion barrier to prevent the inter-diffusion between the nuclear fuel and the cladding material was studied for HT-9 and MA957 tubes. In order to enhance the lifetime of the fuels and the reliability of the fuel claddings, we studied TiN for advanced cladding coating in nuclear reactors. The deposited TiN on the stainless steel samples were studied for hardness and adhesion after thermal cycle test. The TiN has good adhesion with the stainless steel and higher hardness than that of bulk TiN. Thermal conductivity test demonstrates that thin TiN film has compatible thermal conductivity as the MA957 and HT9 bars. The total effective thermal conductivity of TiN/HT-9 and TiN/MA957 has the same as that of tubes. In addition, the diffusion test on Ce/TiN/HT-9 suggests that TiN shows excellent material compatibility and good diffusion barrier property.

6.2 Introduction

Martensitic stainless steels, such as a HT-9 (12Cr-1MoVW), are considered to be potential candidates for the blanket and first wall structures of a fusion reactor. Alloy HT-9 can be used up to a temperature of 500°C in Pb-Bi coolant. HT-9 has a high

chromium (Cr) content of about 12%. The increased Cr content in HT-9 provides good resistance to atmospheric corrosion and resistance to degradation in many organic media, and molybdenum (Mo) enhances the localized corrosion resistance in environments containing deleterious species by preventing the breakdown of protective oxide films.

However, the fuel cladding interaction and interdiffusion with the inner fuels have been a long term problem that significantly reduces the life time of the fuels and causes a safety concerns. There are several proposed methods in preventing the fuel-cladding interactions. One way is implanting a liner inside the cladding tube. Here we propose to develop a multifunctional ceramic coating that serves as effective diffusion barrier to prevent the inter-diffusion between the nuclear fuel and the cladding material and therefore, to dramatically enhance the lifetime of the fuels and the reliability of the fuel claddings in advanced nuclear reactors. This thin coating serves multipurpose including a diffusion barrier, a sacrificial layer as well as a thermal conducting layer. Ultimately different diffusion barriers can be used for different fuel type while keeping the cladding materials the same. If implemented, this thin layer could dramatically improve the performance (i.e. life time and reliability) of the fuel structure and dramatically reduce the cost on service and exchange of the fuel structures.

Titanium nitride (TiN) coatings have found numerous applications in view of their excellent corrosion and erosion resistance, relative inertness, high sublimation temperature, high hardness and desirable optical and electronic properties. For instance, hardness and elastic modulus of TiN film had been reported as up to 33.58 GPa and 407

GPa, respectively [94]. In addition, ion irradiation effects in nanocrystalline TiN coatings as a function of grain size was reported previously and it showed that damage accumulation in the TiN films reduces as the grain size reduces with a good radiation-tolerance property of nanocrystalline TiN films [5]. In order to protect the HT-9 additionally, inner surface of HT-9 tube was considered to be coated by TiN. In this study, therefore, TiN coatings are deposited on HT-9 and MA957 stainless-steel tubes and polished bars. A systematic physical property study conducted with including surface characterization (SEM), mechanical testing, scratch test, thermal cycle test and others, is conducted the effects of the coatings on its mechanical, thermal and diffusion properties of the fuel cladding materials.

6.3 Experimental details

Depositions of TiN single layers on HT-9 and MA957 stainless steel substrates were performed in an ultrahigh vacuum chamber with a KrF excimer laser (Lambda Physik Compex Pro 205, λ = 248 nm, 10 Hz). Laser beam was focused to obtain an energy density of approximately 6 $J{\cdot}cm^{-2}$ at 45° angle of incidence. TiN targets were hot-pressed stoichiometric TiN obtained from Plasma Materials Inc.

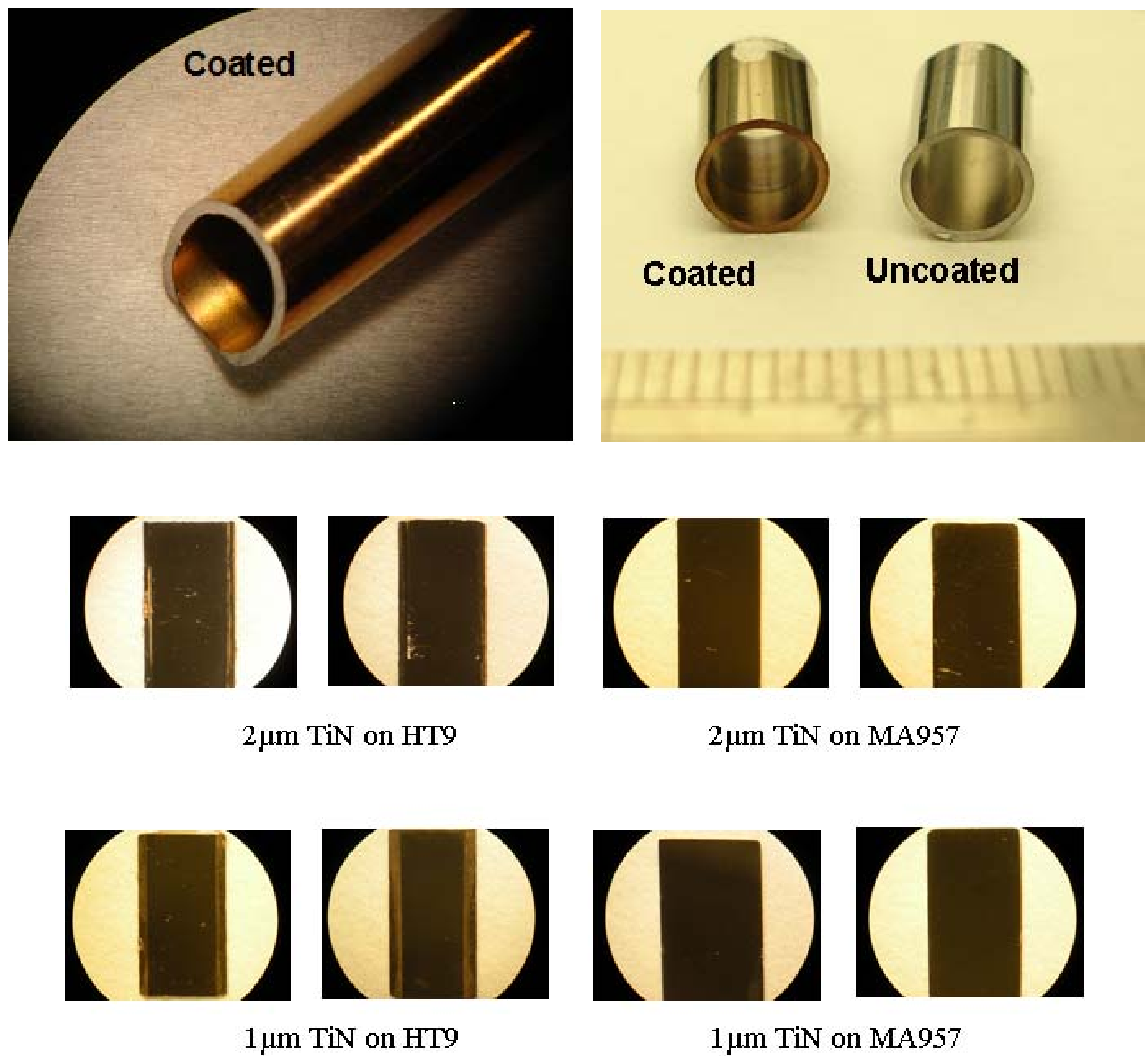

Fig. 6.1 Optical microscope images of TiN/HT-9 and TiN/MA-957 specimens showing very smooth surface of the coatings

Four sets of 1 and 2 μm-thick TiN layers were deposited on HT-9 and MA957 substrates as shown in Fig. 6.1 and one set of the samples was undergone thermal cycle test up to 520 °C from room temperature with five cycles in pressure of approximately 10^{-7} Torr. These four sets of samples were used for the following hardness measurement, scratch test, and thermal conductivity measurement.

The hardness of the as-deposited and thermal-cycle tested samples was measured using Hysitron Tribo-nanoindenter to study mechanical property variation due to thermal stress. The measurement was performed using a standard Berkovich diamond tip (included angle: 142.3°, radius of curvature: ~150 nm) under a constant load mode with load of 4000 μN. In order to minimize any substrate contribution for hardness measurements, the penetration depth was strictly controlled to less than 10 % of total film thickness. Each value and its standard deviation are calculated based on averaging of at least nine indentation experiments per indentation depth. A plateau is typically observed in the hardness vs. indentation depth plot and the plateau value is chosen as the average hardness of the films.

Adhesion of the cladding coating was tested by nano-indenter scratch method in Los Alamos National Laboratory. The applied normal loads on indenter tip were from 30 mN to 90 mN with scratch velocity of 20 μm/s and along scratch length of 500 μm. After scratch test the as-deposited and thermal stressed samples were examined by SEM in order to verify adhesion quality between TiN layers and HT-9 and MA957 substrates.

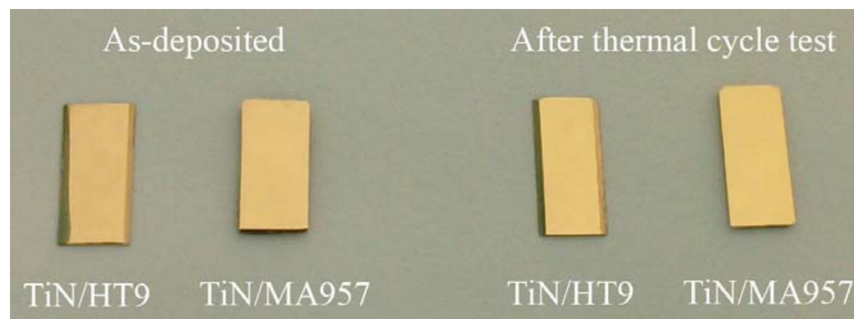

(a)

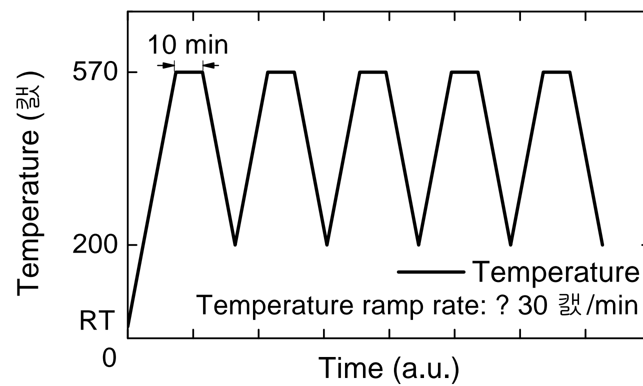

(b)

Fig. 6.2 (a) As-deposited and thermal-cycle tested TiN/HT-9 and TiN/MA957 specimens and (b) thermal cycle test: the maximum temperature is 570 °C in vacuum of 10^{-7} Torr.

The Transient Thermo-Reflectance (TTR) measurement for through-plane thermal conductivity of TiN film was performed using a new compact TTR system developed in the Nanoscale Eletro-Thermal Sciences Laboratory (NETSL) at SMU. The basic principle of the transient thermal reflectance method is to heat a sample by laser irradiation and probe the transient surface temperature by the surface reflectivity of the heated material. In the system built in the NETSL at SMU, the heating source is an Nd: YAG laser that is pulsed at 30 Hz with a wavelength of 532 nm, maximum output pulse energy of 0.5 mJ/pulse, and a pulse-width of 6.1 ns. The probing light source is a CW Ar-Ion laser with a wavelength of 488 nm in a single-mode irradiation and maximum output of 25 mW. The amount of heating energy used from the heating source was 25.71 μJ/pulse which was measured directly by a power meter and the fluence was 957 J m^{-2} for the samples measured.

6.4 Results and discussion

The stainless steel HT9, a ferritic alloy is one of the primary cladding alloys under consideration and MA957 is designed for potential applications in the nuclear industry. The TiN films were deposited at a typical growth rate of 0.6 Å/pulse for TiN layer with a base pressure of approximately 10^{-7} Torr and deposition temperature of 700 °C. Prior to film deposition, the HT-9 and MA957 tubes were cut and polished by 1 μm grid diamond paper as final step, and then cleaned in acetone and methanol. Each TiN/HT-9 and TiN/MA957 sample was used for mechanical test, scratch test, and SEM

images before and after thermal cycle test. TiN thin films were deposited on both HT-9 and MA957 tubes and on the flat polished bars after cutting and polishing the tubes as shown in Fig. 6.1. The thermal cycle test was conducted for each set of TiN/HT-9 and TiN/MA957 samples, Fig. 6.2 (a), from 200 °C to 570 °C during five-period in ultra-high vacuum of 10^{-7} Torr as shown in Fig. 6.2 (b). It is one of adhesion tests between TiN and stainless steel (HT-9 and MA957).

Leibowitz and Blomquist [95] measured thermal expansion of stainless steel HT-9, which the composition is 0.5wt% Ni, 12.0wt% Cr, 0.2wt% Mn, 1.0wt% Mo, 0.25 wt% Si, 0.5 wt% W, 0.5 wt% V, and 0.2 wt% C, with the balance Fe. They reported that HT9 shows a phase transition in the neighborhood of 1030K from typical of 316 stainless steel to similar 410 stainless steel in these properties [95]. The thermal expansion coefficient and thermal conductivity of HT-9 were known as 12.5×10^{-6} K^{-1} and 28 $Wm^{-1}K^{-1}$, respectively [96]. Comparing the properties of TiN, which has thermal expansion coefficient of 9.36×10^{-6} K^{-1} and thermal conductivity of 30 $Wm^{-1}K^{-1}$ [33, 97, 98], the adhesion within the temperature range were expected to be excellent.

SEM images of 2 μm specimens shows that there is no damage on the TiN surface after thermal cycle test with five cycles from 190°C to 570°C in vacuum (10^{-6} mbar) chamber (Fig. 6.2). The surface is very smooth without any indication of crack or delamination. Figure 6.3 and 6.4 show the low and high magnification SEM images of the TiN/HT-9 and TiN/MA-957 surface with comparing as-deposited and thermal cycle tested specimens. As shown in the Fig. 6.3 and 6.4, any delamination or peal-off was not observed in the samples after the thermal cycle test. Not only the surface, but also cross-

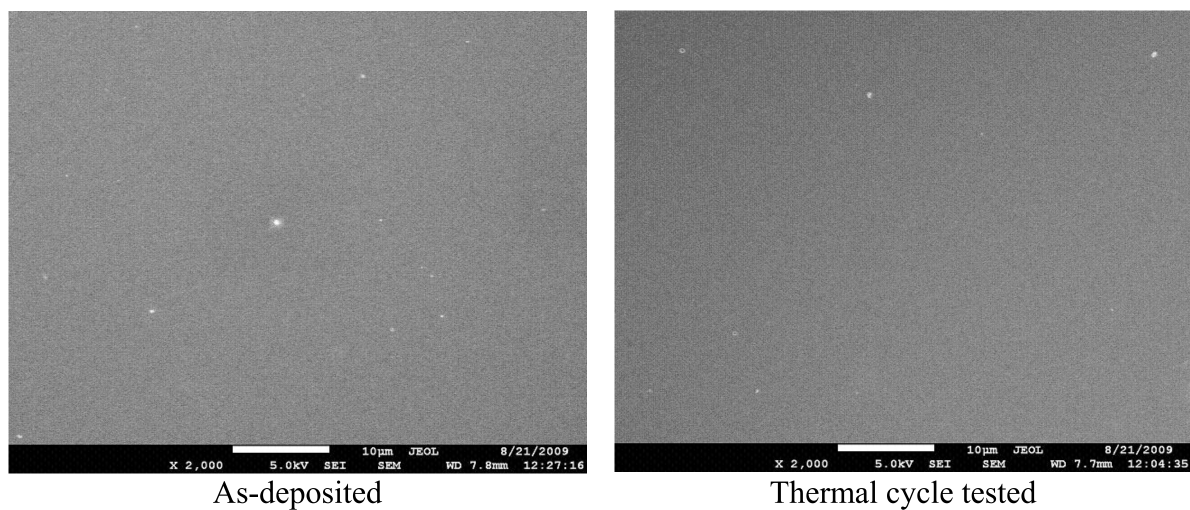

As-deposited Thermal cycle tested

Fig. 6.3 Plan-view SEM Image of 2µm TiN/HT-9 as-deposited and thermal cycle tested with low magnification

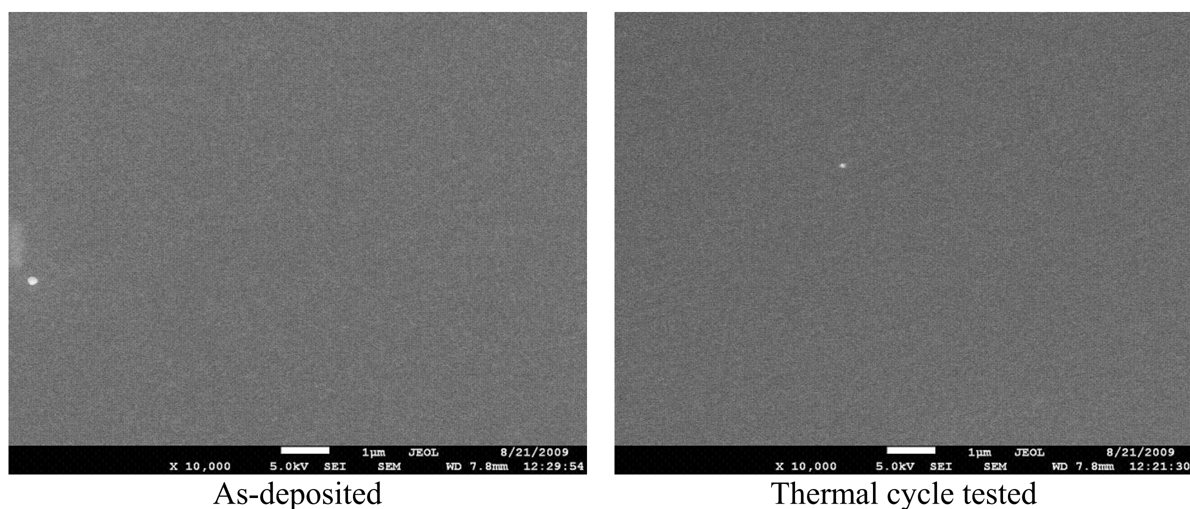

As-deposited Thermal cycle tested

Fig. 6.4 Plan-view SEM Image of 2µm TiN/MA-957 as-deposited and thermal cycle tested with high magnification

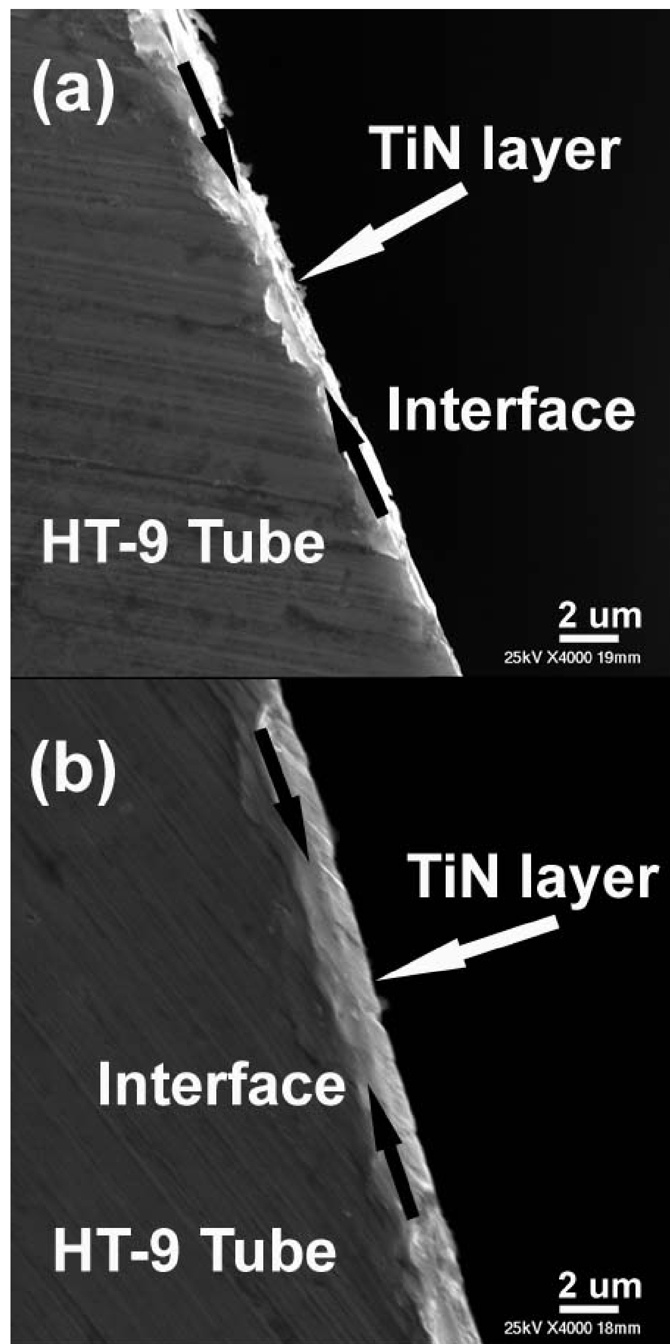

Fig. 6.5 Cross-sectional SEM images (a) before and (b) after thermal cycle tested TiN/HT-9 tube

sectional image shows good adhesion between TiN and the stainless steel substrates. The cross-sectional image on TiN deposited HT-9 tube does not show any obvious delamination of the TiN layer in the interface between the HT-9 and TiN layer as shown in Fig. 6.5. The dark arrows indicate the interface between TiN and HT-9 surface, and it is difficult to distinguish the difference before and after thermal cycle test.

The adhesion and hardness are important properties to protect the fuel cladding tubes in nuclear reactor. After the thermal cycle test, hardness was measured on the TiN coated HT-9 and MA957 specimens by nanoindentation method. Berkovich indenter tip was used for nanoindentation and maximum indentation depth was less than 100 nm with applying 4000 μN and loading rate of 300 μN/sec on 16 locations of each sample. The measured hardness is shown in Table 6.1.

Table 6.1 Hardness of TiN/HT-9 and TiN/MA-957 specimens

	TiN/HT-9				TiN/MA957			
	as-deposited		thermal cycle tested		as-deposited		thermal cycle tested	
TiN thickness	H_{ave} (GPa)	StDev	H_{ave} (GPa)	StDev	H_{ave} (GPa)	StDev	H_{ave} (GPa)	StDev
2 um	28.51	1.24	30.11	0.94	27.14	1.92	29.98	0.99
1 um	27.09	1.96	24.95	0.87	26.65	2.47	26.24	2.07

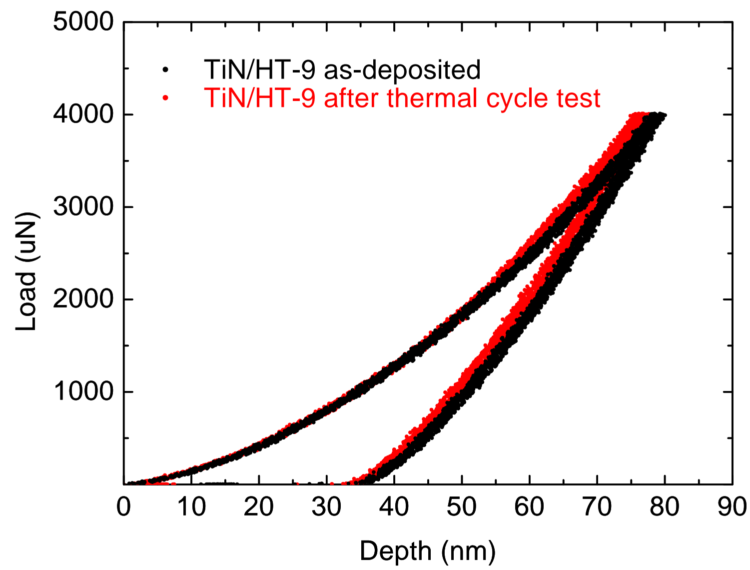

(a)

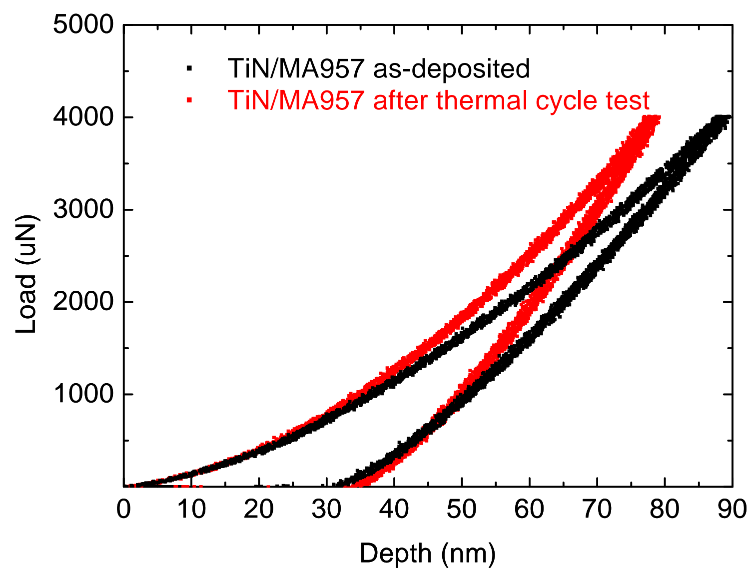

(b)

Fig. 6.6 Load vs. depth of nanoindentation measurements before and after thermal-cycle test: (a) TiN/HT-9 and (b) TiN/MA957

The averaged hardness of TiN/HT-9 is 28.51 GPa and 30.11 GPa on 2 μm thick TiN on HT-9 strips before and after thermal cycle test, respectively. TiN/MA957 also has similar hardness values as 27.14 GPa and 29.98 GPa before and after thermal cycle test, respectively. Comparing the hardness of a cubic phase TiN on Si(001) and bulk TiN, the hardness shows dependence on the crystal phase of structure, thickness of film, and surface roughness. The hardness of TiN is ~33 GPa [67] in thin cubic phase film form and bulk TiN has lower hardness as ~21 GPa [87]. Considering the polished stainless steel substrates, the measured hardness shows high mechanical quality because the surface roughness of the substrate must be higher than silicon substrate.

Measured hardness of TiN/HT-9 and TiN/MA957 shows that TiN layer is still stable and robust after the thermal cycle test. The 2 μm TiN specimens have better polished substrate surface than that of 1 μm TiN specimens. We suspect that the surface roughness of 1 μm TiN specimens resulted in the hardness measurement with increasing standard deviation on the specimen. Figure 6.6 shows the loading and unloading curves of nanoindentation performed for 2 um TiN films on HT-9 substrates and MA-957 substrates, respectively. The loading and unloading curves on TiN/HT-9 specimens shows that the hardness and modulus did not changed after thermal cycle test. In addition, it shows that there is not any delamination of deposited TiN on HT-9 substrate.

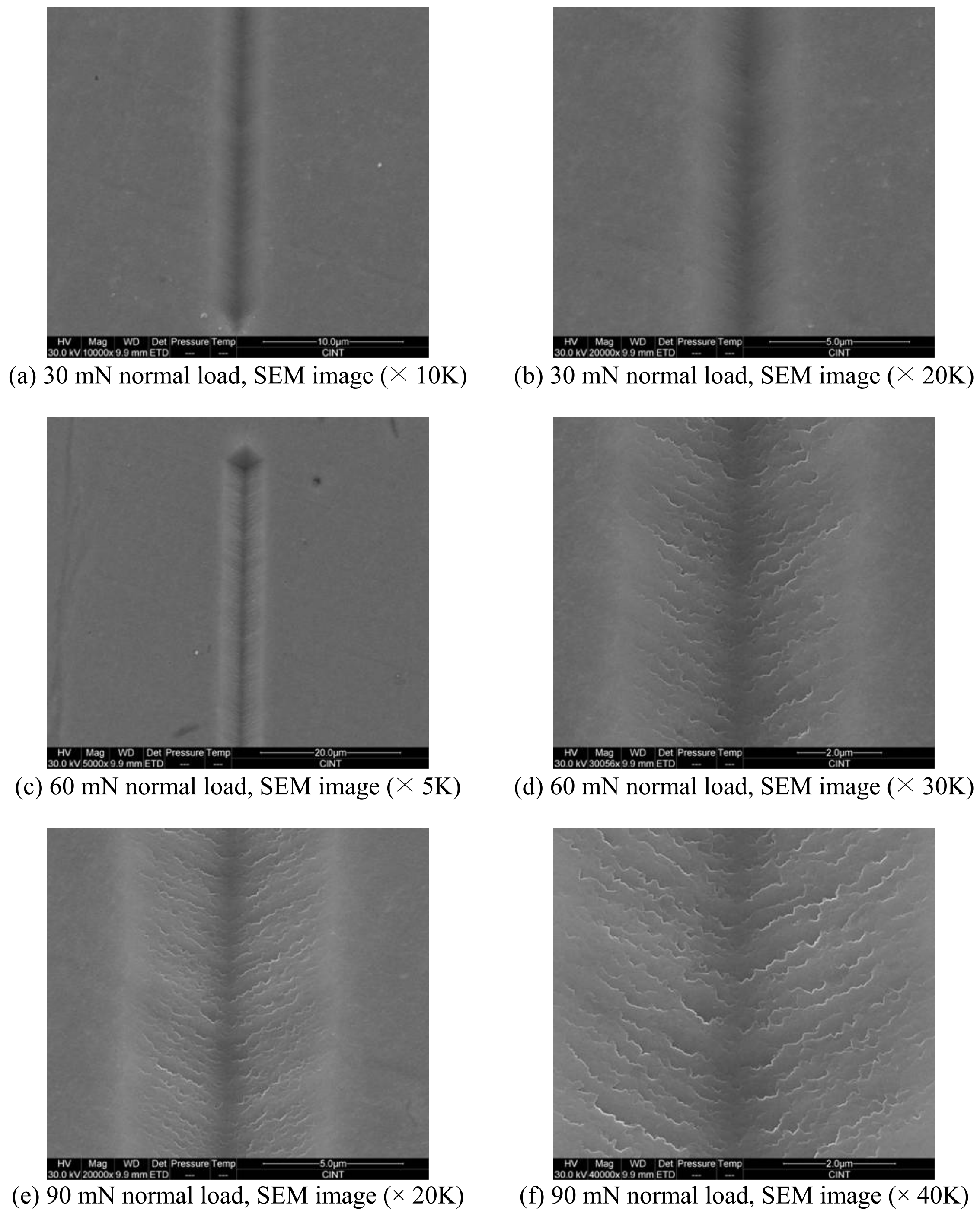

(a) 30 mN normal load, SEM image (× 10K) (b) 30 mN normal load, SEM image (× 20K)

(c) 60 mN normal load, SEM image (× 5K) (d) 60 mN normal load, SEM image (× 30K)

(e) 90 mN normal load, SEM image (× 20K) (f) 90 mN normal load, SEM image (× 40K)

Fig. 6.7 SEM image of a scratch test track on TiN/HT-9 sample after scratch test with (a, b) 30 mN, (c, d) 60 mN, and (e, f) 90 mN normal load

In the scratch adhesion test, the critical loads for cohesive failure and adhesive failure are sensitively governed by the film hardness. The wear rate decreases with increasing hardness [73]. The adhesion force of the film is defined as two critical loads: one is the critical load that required for the failure of the film itself, cohesive failure , and the other is the critical load that required for the failure of the interface between the film and the substrate, adhesive failure. In the adhesion test, it is expected that the cohesive failure and the adhesive failure will occur simultaneously if the interfacial adhesion between the film and the substrate is poor. On the other hand, the cohesive failure will take place first and then be followed by the adhesive failure if the interfacial adhesion is strong [73].

Scratch test was conducted on TiN/HT-9 strip samples that have 1 μm thickness of TiN layer. Using Nanoindenter XP three different maximum normal loads were applied and made scratch with constant scratch velocity 20 μm/s and 500 μm scratch length. The applied normal loads are 30 mN, 60 mN, and 90 mN through Berkovich indenter tip. SEM images show the track of scratch test on TiN surface in Fig. 6.7. On the TiN/HT-9 surface, increasing the normal load up to 90 mN, the depth was increased, however, any adhesive or cohesive failure was not observed and no delamination of TiN layer happened. Scratch test verified that TiN/HT-9 has good adhesion in PLD coating methods.

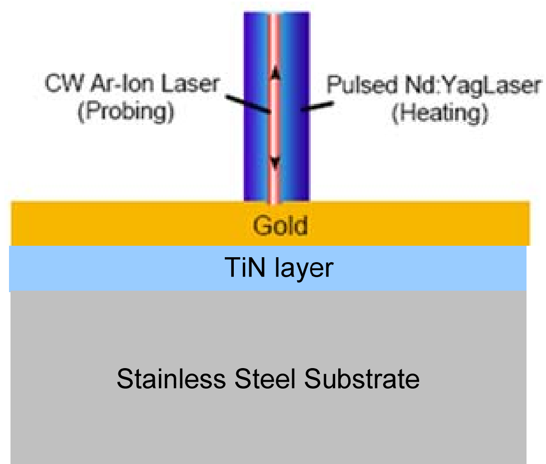

Fig. 6.8 Schematic cross-section of sample with applied TTR measurement

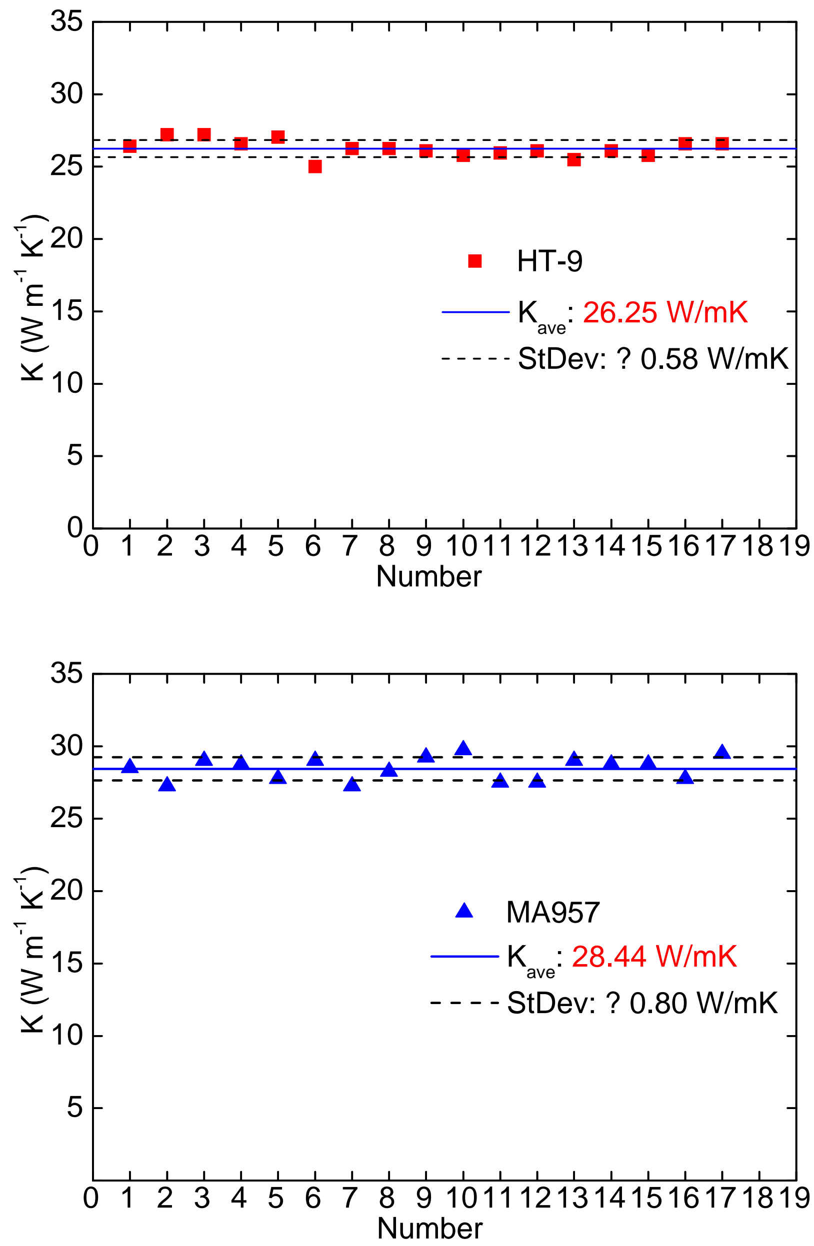

Fig. 6.9 Measured intrinsic thermal conductivity (K_{int}) of HT-9 and MA957 by TTR method

In nuclear react system thermal dissipation is one of important property for fuel cladding coating. The thickness of TiN on HT-9 or MA957 is only several micro-meter, but it is needed to verify the ability of thermal diffusivity of the TiN/HT-9 and TiN/MA957 for engineering design.

The TTR method was applied to measure the thermal conductivity of TiN layer on HT-9 and MA957 substrates. As introduced in previous Chapters, gold layer was deposited on the polished HT-9 and MA957 substrates and the TiN/HT-9 and TiN/MA957 specimens, and measured the thermal conductivity of the HT-9 and MA957 substrates and the coated TiN layers on the stainless steel substrates as shown in Fig. 6.8.

The intrinsic through-plane thermal conductivity for HT-9 and MA957 was measured first. The average value of the intrinsic thermal conductivity is 26.25 and 28.44 W $m^{-1}K^{-1}$ for HT-9 and MA957, respectively as shown in Fig. 6.9. These values are well matched with previous study by researchers [87, 95], and used to measure the thermal conductivity of TiN layers on HT-9 and MA957 substrates.

Since there must be size effect on thermal conductivity of thin film, the thickness of TiN layers were measured by using Detek profilometer. In order to apply the profilometer, these TiN layers were deposited on the substrates by using shadow mask method to make a step on the TiN layer. The measured thickness of TiN layers is 919 nm and 899 nm on HT-9 and on MA957 substrates, respectively. The measured thermal conductivity is plotted as a circle mark in Fig. 6.10.

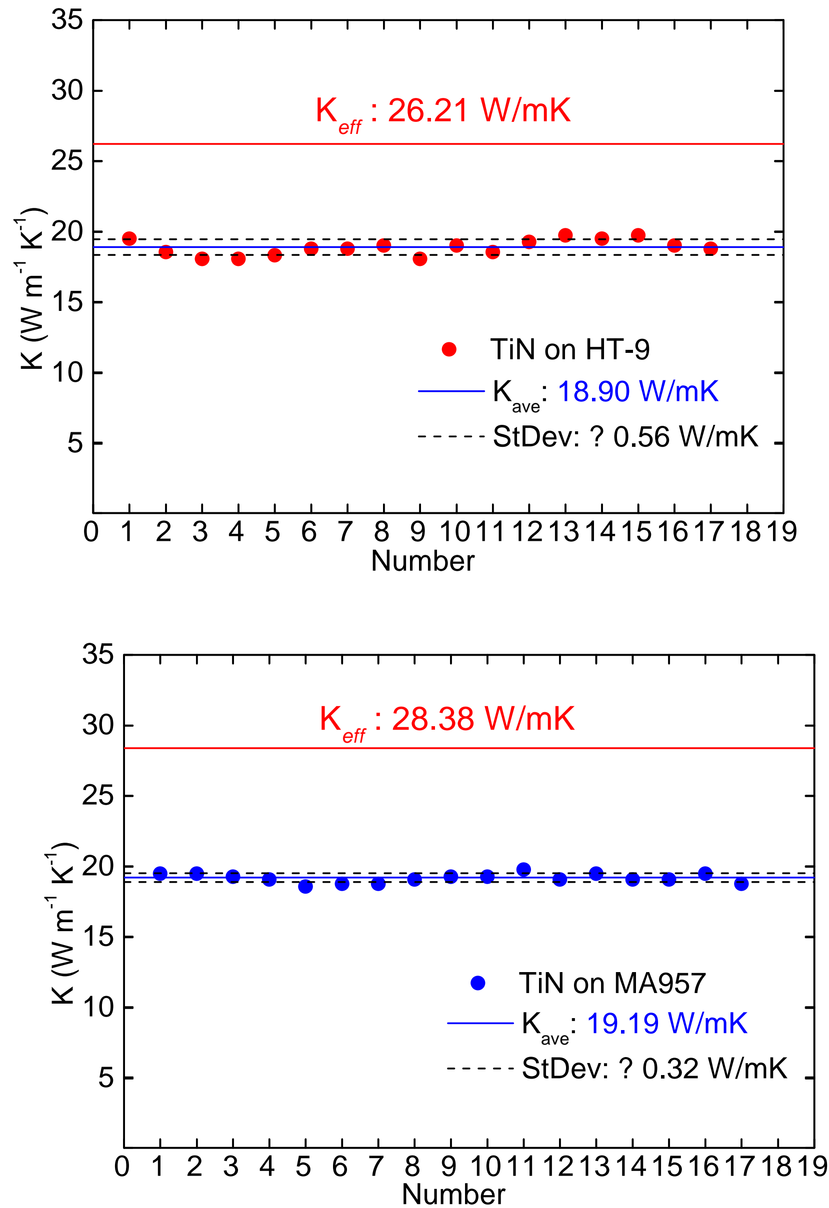

Fig. 6.10 Measured intrinsic thermal conductivity (K_{int}) of TiN on HT-9 and MA957 by TTR method and calculated effective thermal conductivity (K_{eff}) of TiN/HT9 and TiN/MA957

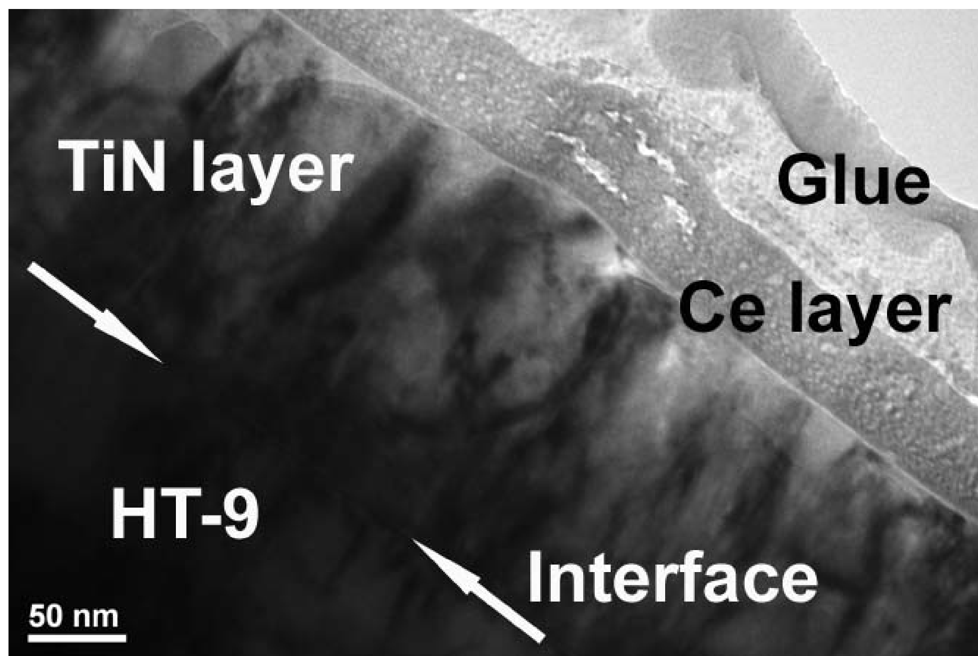

Fig. 6.11 TEM image of Ce/TiN (200 nm) /HT-9 after annealing: Ce diffusion test on TiN/HT-9 at 600 °C for 12 hours at vacuum pressure of 1×10^{-6} mbar

The thermal conductivity of TiN is 18.9 W $m^{-1}K^{-1}$ and 19.2 W $m^{-1}K^{-1}$ on the HT-9 and MA957 substrates, respectively. Then, the total effective thermal conductivity of TiN/HT-9 and TiN/MA957 was calculated for the assumed 2 μm thick TiN on HT-9 and MA957 substrates that assumed as 1 mm thick substrates for engineering design. Because the assumed TiN thickness (2 μm) is much smaller than the 1 mm thick stainless steel substrates, the total effective thermal conductivity of the designed TiN/HT-9 and TiN/MA957 is very closed to the intrinsic thermal conductivity of the stainless steel substrates, as shown in Fig. 6.10. The results mean that the ~1 μm thick TiN layer is enough for heat dissipation on both of HT-9 and MA957 tube material.

In the final step to confirm the cladding coating as TiN, diffusion test was conducted by using annealing Ce/TiN/HT-9 specimen. Titanium nitride was deposited on HT-9 substrate with thickness as ~200nm and the 50 nm Ce was deposited on the TiN layer in approximately 10^{-7} Torr vacuum chamber by PLD method. This Ce/TiN/HT-9 was annealed at 600 °C for 12 hours in 10^{-6} Torr vacuum chamber. After diffusion test, the cross-section area was studied by TEM and it is shown in Fig. 6.11. The bright arrows indicate the interface between TiN layer and HT-9 surface. On the TiN layer, the deposited Ce is shown and the interfaces between Ce and TiN are very clean without any indication of interfacial reactions and interdiffusions after annealing at 600 ^{o}C for 12 hours.

6.5 Summary

Titanium nitride that serves as effective diffusion barrier to prevent the inter-diffusion between the nuclear fuel and the cladding material was studied for HT-9 and MA957 tubes to enhance the lifetime of the fuels and the reliability of the fuel claddings in advanced nuclear reactors. The deposited TiN on the stainless steel samples were studied for hardness and adhesion after thermal cycle test. The TiN has good adhesion with the stainless steel and higher hardness than that of bulk TiN. Thermal conductivity test demonstrates that thin TiN film has compatible thermal conductivity as the MA957 and HT9 bars. The total effective thermal conductivity of TiN/HT-9 and TiN/MA957 has the same as that of tubes. In addition, the diffusion test on Ce/TiN/HT-9 suggests that TiN shows excellent material compatibility and good diffusion barrier property.

CHAPTER VII

SUMMARY AND CONCLUSIONS

In order to enhance the material property, superlattices is one of artificially engineered protective coatings, such as AlN/TiN and TaN/TiN multilayered films. The nitride based materials studies and presented in this dissertation are the transition metals nitrides such as TiN, TaN and AlN, either as a single film layer or a multilayer structure. In this study, the interface and size effects as well as crystal phase influence on radiation tolerance and on electrical thermal properties were studied for thin TaN/TiN and AlN/TiN multilayered films with varying nanolayer thickness, interfacial density and crystal phase such as epitaxial cubic phase and polycrystalline.

Epitaxial cubic multilayer films, TaN/TiN and AlN/TiN nanolayers were grown on Si(001) by Pulsed Laser Deposition (PLD) with various nanolayer thicknesses and number of interface. Microstructural studies include X-ray diffraction (XRD), transmission electron microscopy (TEM) and high resolution TEM with ion-irradiation experiments. Electrical, mechanical and thermal property studies were conducted for the interface and size effects on the nanolayers by using nanoindentation and Transient Thermo-Reflectance (TTR) methods.

Microstructural and hardness study on TaN/TiN films before and after ion irradiation (12 keV and 50 keV He^{+}) suggest that no obvious microstructural or mechanical behavior change due to ion irradiation. In addition, the size effect on electrical resistivity is dominant in both of the epitaxial cubic and the polycrystalline

TiN thin films in the thickness ranged from ~60 nm down to ~35nm. In the TaN/TiN multilayer, the grain scattering effect on resistivity is dominant rather than interface influence on the resistivity with comparing epitaxial cubic phase and polycrystalline phase.

Evolution of the microstructure and hardness of the AlN/TiN multilayer films were examined on the specimens before and after He^+ implantation to a fluence of 4×10^{16} cm^{-2} at 50 keV. The suppression of amorphization in AlN layers and the reduction of radiation-induced softening were observed in all nanolayer films. Radiation tolerance was found to be size dependent and the layer thickness leading to the highest radiation tolerance was 10 nm.

The embedded epitaxial cubic AlN and polycrystalline AlN nanolayer with cladding TiN layers as TiN/AlN/TiN system were studied for thermal conductivity. In addition, single layered epitaxial and polycrystalline TiN films with various thicknesses were prepared at 700 °C and room temperature. Microstructure and thermal transport properties of the films have been experimentally investigated for crystal phase and size effects in the TiN single layer and the embedded AlN layer in three-layered TiN/AlN/TiN films. The through-plane intrinsic thermal conductivity K_{int} was significantly decreased from 9.6 $Wm^{-1}K^{-1}$ at 41 nm down to 6.0 $Wm^{-1}K^{-1}$ at 9 nm thick epitaxial TiN film by surface boundary scattering of heat carrier. In addition, polycrystalline TiN film showed thermal conductivity drop that is from 8.0 $Wm^{-1}K^{-1}$ at 38 nm down to 4.6 $Wm^{-1}K^{-1}$ at 9 nm, which is influenced by additional grain boundary scattering of carrier.

Depending on phase of the embedded AlN by cladding TiN, the epitaxial cubic AlN showed higher effective thermal conductivity than that of polycrystalline AlN in the thickness ranged from 10 nm down to 2 nm. Grain boundary scattering of phonon and the crystal phase of structure effect on thermal conductivity are still dominant in the ultra-thin nanolayer regime as well as the surface boundary scattering of phonon. The embedded epitaxial cubic AlN experienced the suppressed size effect, which reduces the amount of decrease in through-plane thermal conductivity. The minimum effective thermal conductivity of the embedded c-AlN with 2 nm thickness was higher than that of single layered c-AlN with 200 nm thickness reported. It confirms the phonon confinement effect in multilayer as well as the importance of film thickness, interface and microstructure for material properties in nanolayers.

Titanium nitride that serves as effective diffusion barrier to prevent the inter-diffusion between the nuclear fuel and the cladding material was studied in order to enhance the lifetime of the fuels and the reliability of the fuel claddings. The TiN has good adhesion with the stainless steel and higher hardness than that of bulk TiN on the stainless steel. Thermal conductivity test demonstrated that the thin TiN film has compatible thermal conductivity as the MA957 and HT-9 bars.

REFERENCES

[1] S. Cho, K. Lee, P. Song, H. Jeon, Y. Kim, Jpn J Appl Phys 1, 46 (2007) 4085-4088.

[2] A.E. Kaloyeros, E. Eisenbraun, Annu Rev Mater Sci, 30 (2000) 363-385.

[3] R. Nowak, C.L. Li, Thin Solid Films, 305 (1997) 297-303.

[4] J.H. Sung, T.H. Kim, S.S. Kim, Wear, 250 (2001) 658-664.

[5] H. Wang, R. Araujo, J.G. Swadener, Y.Q. Wang, X. Zhang, E.G. Fu, T. Cagin, Nucl Instrum Meth B, 261 (2007) 1162-1166.

[6] W.J. Weber, Nucl Instrum Meth B, 166 (2000) 98-106.

[7] E.G. Fu, J. Carter, G. Swadener, A. Misra, L. Shao, H. Wang, X. Zhang, J Nucl Mater, 385 (2009) 629-632.

[8] N. Li, E.G. Fu, H. Wang, J.J. Carter, L. Shao, S.A. Maloy, A. Misra, X. Zhang, J Nucl Mater, 389 (2009) 233-238.

[9] M. Milosavljevic, D. Perusko, V. Milinovic, Z. Stojanovic, A. Zalar, J. Kovac, C. Jeynes, J Phys D Appl Phys, 43 (2010) 65302.

[10] H. Ohara, A. Nakayama, T. Nomura, J Vac Sci Technol A, 15 (1997) 2609-2614.

[11] A.L. Lima, X. Zhang, A. Misra, C.H. Booth, E.D. Bauer, M.F. Hundley, Thin Solid Films, 515 (2007) 3574-3579.

[12] J. Zou, X. Lange, C. Richardson, J Appl Phys, 100 (2006) 104309.

[13] K. Watari, H. Nakano, K. Urabe, K. Ishizaki, S.X. Cao, K. Mori, J Mater Res, 17 (2002) 2940-2944.

[14] K. Watari, H. Nakano, T. Tsugoshi, T. Nagaoka, K. Urabe, S. Cao, K. Mori, K. Ishizaki, Key Eng Mat, 247 (2003) 361-364.

[15] A. Misra, M.F. Hundley, D. Hristova, H. Kung, T.E. Mitchell, M. Nastasi, J.D. Embury, J Appl Phys, 85 (1999) 302-309.

[16] X. Zhang, N. Li, O. Anderoglu, H. Wang, J.G. Swadener, T. Hochbauer, A. Misra, R.G. Hoagland, Nucl Instrum Meth B, 261 (2007) 1129-1132.

[17] N. Li, M.S. Martin, O. Anderoglu, A. Misra, L. Shao, H. Wang, X. Zhang, J Appl Phys, 105 (2009) 123522.

[18] A. Misra, M.J. Demkowicz, X. Zhang, R.G. Hoagland, JOM-J Min Met Mat S, 59 (2007) 62-65.

[19] W.M. Rohsenow, H.Y. Choi, Heat, Mass, and Momentum Transfer, Prentice-Hall, Englewood Cliffs, NJ, 1961.

[20] D.G. Cahill, H.E. Fischer, T. Klitsner, E.T. Swartz, R.O. Pohl, J Vac Sci Technol A, 7 (1989) 1259-1266.

[21] M.A. Omar, Elementary Solid State Physics, Addison-Wesley Publishing Company, Massachusetts, 1993.

[22] M.I. Flik, B.I. Choi, K.E. Goodson, J Heat Trans-T ASME, 114 (1992) 666-674.

[23] R.M. Costescu, M.A. Wall, D.G. Cahill, Phys Rev B, 67 (2003) 054302.

[24] G. Pernot, M. Stoffel, I. Savic, F. Pezzoli, P. Chen, G. Savelli, A. Jacquot, J. Schumann, U. Denker, I. Monch, C. Deneke, O.G. Schmidt, J.M. Rampnoux, S. Wang, M. Plissonnier, A. Rastelli, S. Dilhaire, N. Mingo, Nat Mater, 9 (2010) 491-495.

[25] M.G. Burzo, P.L. Komarov, P.E. Raad, IEEE T Compon Pack T, 26 (2003) 80-88.

[26] J. Park, D.J. Kim, Y.K. Kim, K.H. Lee, K.H. Lee, H. Lee, S. Ahn, Thin Solid Films, 435 (2003) 102-107.

[27] A. Horling, L. Hultman, M. Oden, J. Sjolen, L. Karlsson, J Vac Sci Technol A, 20 (2002) 1815-1823.

[28] A. Kimura, H. Hasegawa, K. Yamada, T. Suzuki, J Mater Sci Lett, 19 (2000) 601-602.

[29] J. Musil, H. Hruby, Thin Solid Films, 365 (2000) 104-109.

[30] M. Takeyama, A. Noya, T. Sase, A. Ohta, K. Sasaki, J. Vac. Sci. Technol., B, 14 (1996) 674-678.

[31] M. Setoyama, A. Nakayama, M. Tanaka, N. Kitagawa, T. Nomura, Surf Coat Tech, 87-8 (1996) 225-230.

[32] G.A. Slack, R.A. Tanzilli, R.O. Pohl, J.W. Vandersande, J Phys Chem Solids, 48 (1987) 641-647.

[33] H.O. Pierson, Handbook of Refractory Nitrides and Carbides, Noyes Publications, New York, 1996.

[34] J.T. Cheung, H. Sankur, Crit Rev Solid State, 15 (1988) 63-109.

[35] H.M. Smith, A.F. Turner, Appl Optics, 4 (1965) 1673-1674.

[36] D.B.Chrisey.G.K. Hubler, Pulsed Laser Deposition of Thin Films, Wiley-VCH, New York, 2003.

[37] R.K. Singh, O.W. Holland, J. Narayan, J Appl Phys, 68 (1990) 233-247.

[38] R.K. Singh, J. Narayan, Phys Rev B, 41 (1990) 8843-8859.

[39] C. Suryanarayana, M.G. Norton, X-Ray Diffraction: A Practical Approach, Springer, New York, 1998.

[40] B.D. Cullity, Elements of X-ray Diffraction, Addison-Wesley, Massachusetts, 1978.

[41] J. Als-Nielsen, D. McMorrow, Elements of Modern X-ray Physics, John Wiley & Sons Ltd., London, 2001.

[42] P.J.Goodhew, F.J. Humphreys, R. Beanland, Electron Microscopy and Analysis, Taylor & Francis, New York, 2000.

[43] J.J. Bozzola, L.D. Russell, Electron Microscopy: Principles and Techniques for Biologists, Jones and Bartlett Inc., Sudbury, 1999.

[44] M.G. Burzo, P.L. Komarov, P.E. Raad, J Heat Trans-T ASME, 124 (2002) 1009-1018.

[45] P.L. Komarov, M.G. Burzo, G. Kaytaz, P.E. Raad, Microelectr J, 34 (2003) 1115-1118.

[46] S.J. Kline, F.A. McClintock, Mech Eng 75 (1953), 3-8

[47] M.G. Burzo, Transient Thermoreflectance Measurements of the Thermal Properties of Metallized Thin-Film Electronics Materials, Ph.D. Dissertation, Mechanical Engineering, Southern Methodist University, Dallas, TX, 2001.

[48] L.B. Valdes, PIRE, 42 (1954) 420-427.

[49] H. Wang, A. Gupta, A. Tiwari, X. Zhang, J. Narayan, J Electron Mater, 32 (2003) 994-999.

[50] H. Wang, X. Zhang, A. Gupta, A. Tiwari, J. Narayan, Appl Phys Lett, 83 (2003) 3072-3074.

[51] ITRS, Process Integration, Devices, and Structures, 2007 http://www.itrs.net/Links/2007ITRS/2007_Chapters/2007_PIDS.pdf

[52] J.F. Ziegler, Radiat Eff Deffct S, 141 (1997) 455-455.

[53] Y. Katoh, M. Ando, A. Kohyama, J Nucl Mater, 323 (2003) 251-262.

[54] R.L. Klueh, D.S. Gelles, S. Jitsukawa, A. Kimura, G.R. Odette, B. van der Schaaf, M. Victoria, J Nucl Mater, 307 (2002) 455-465.

[55] H. Trinkaus, H. Ullmaier, J Nucl Mater, 215 (1994) 303-309.

[56] L.L. Snead, S.J. Zinkle, J.C. Hay, M.C. Osborne, Nucl Instrum Meth B, 141 (1998) 123-132.

[57] S.J. Bull, T.F. Page, J Mater Sci, 27 (1992) 3605-3616.

[58] L. Boudoukha, S. Paletto, G. Fantozzi, F. Halitim, J Mater Sci, 32 (1997) 2911-2920.

[59] K. Yokota, K. Nakamura, T. Kasuya, K. Mukai, M. Ohnishi, J Phys D Appl Phys, 37 (2004) 1095-1101.

[60] H. Shen, R. Ramanathan, Microelectron Eng, 83 (2006) 206-212.

[61] K. Kaneko, Y. Furuya, M. Kikuchi, Fusion Eng Des, 19 (1992) 293-298.

[62] T.D. Shen, Nucl Instrum Meth B, 266 (2008) 921-925.

[63] T.D. Shen, S. Feng, M. Tang, J.A. Valdez, Y. Wang, K.E. Sickafus, Appl Phys Lett, 90 (2007) 263115.

[64] G.A. Kachurin, M.O. Ruault, A.K. Gutakovsky, O. Kaitasov, S.G. Yanovskaya, K.S. Zhuravlev, H. Bernas, Nucl Instrum Meth B, 147 (1999) 356-360.

[65] A. Meldrum, L.A. Boatner, R.C. Ewing, Phys Rev Lett, 88 (2002) 25503.

[66] A. Meldrum, L.A. Boatner, R.C. Ewing, Nucl Instrum Meth B, 207 (2003) 28-35.

[67] T.A. Rawdanowicz, V. Godbole, J. Narayan, J. Sankar, A. Sharma, Compos Part B-Eng, 30 (1999) 657-665.

[68] S.O. Kucheyev, J.S. Williams, C. Jagadish, G. Li, S.J. Pearton, Appl Phys Lett, 76 (2000) 3899-3901.

[69] S.O. Kucheyev, J.S. Williams, J. Zou, C. Jagadish, M. Pophristic, S. Guo, I.T. Ferguson, M.O. Manasreh, J Appl Phys, 92 (2002) 3554-3558.

[70] T. Yano, K. Ichikawa, M. Akiyoshi, Y. Tachi, J Nucl Mater, 283 (2000) 947-951.

[71] L. David, S. Gomes, G. Carlot, J.P. Roger, D. Fournier, C. Valot, M. Raynaud, J Phys D Appl Phys, 41 (2008) 035502.

[72] M. Tajika, H. Matsubara, W. Rafaniello, Mater Lett, 41 (1999) 139-144.

[73] M.K. Lee, W.W. Kim, J.S. Kim, W.J. Lee, J Nucl Mater, 254 (1998) 42-48.

[74] M. Setoyama, M. Irie, H. Ohara, M. Tsujioka, Y. Takeda, T. Nomura, N. Kitagawa, Thin Solid Films, 341 (1999) 126-131.

[75] D.G. Cahill, W.K. Ford, K.E. Goodson, G.D. Mahan, A. Majumdar, H.J. Maris, R. Merlin, S.R. Phillpot, J Appl Phys, 93 (2003) 793-818.

[76] M.I. Flik, C.L. Tien, J Heat Trans-T ASME, 112 (1990) 872-881.

[77] S.P. Gurrum, W.P. King, Y.K. Joshi, K. Ramakrishna, J Heat Trans-T ASME, 130 (2008) 082403.

[78] B. Feng, Z.X. Li, X. Zhang, J Appl Phys, 105 (2009) 104315.

[79] B. Feng, Z.X. Li, X. Zhang, Thin Solid Films, 517 (2009) 2803-2807.

[80] P.K. Kuo, G.W. Auner, Z.L. Wu, Thin Solid Films, 253 (1994) 223-227.

[81] S.R. Choi, D. Kim, S.H. Choa, S.H. Lee, J.K. Kim, Int J Thermophys, 27 (2006) 896-905.

[82] A.A. Irudayaraj, R. Srinivasan, P. Kuppusami, E. Mohandas, S. Kalainathan, K. Ramachandran, J Mater Sci, 43 (2008) 1114-1120.

[83] A. Majumdar, J Heat Trans-T ASME, 115 (1993) 7-16.

[84] M.G. Burzo, P.L. Komarov, P.E. Raad, Microelectr J, 33 (2002) 697-703.

[85] P.L. Komarov, P.E. Raad, Int J Heat Mass Tran, 47 (2004) 3233-3244.

[86] M.G. Burzo, P.L. Komarov, P.E. Raad, IEEE T Compon Pack T, 28 (2005) 39-44.

[87] J.F. Shackelford, W. Alexander, Materials Science and Engineering Handbook, CRC Press LLC, Boca Raton, 2001.

[88] V. Giraud, J. Cluzel, V. Sousa, A. Jacquot, A. Dauscher, B. Lenoir, H. Scherrer, S. Romer, J Appl Phys, 98 (2005) 013520.

[89] P. Patsalas, C. Charitidis, S. Logothetidis, Surf Coat Tech, 125 (2000) 335-340.

[90] O. Lefeuvre, P. Zinin, G.A.D. Briggs, Ultrasonics, 36 (1998) 229-232.

[91] A. AlShaikhi, G.P. Srivastava, Phys Rev B, 76 (2007) 195205.

[92] A. AlShaikhi, G.P. Srivastava, J Appl Phys, 103 (2008) 083554.

[93] M. Bickermann, B.M. Epelbaum, A. Winnacker, J Cryst Growth, 269 (2004) 432-442.

[94] S.H. Kim, H. Park, K.H. Lee, S.H. Jee, D.J. Kim, Y.S. Yoon, H.B. Chae, J Ceram Process Res, 10 (2009) 49-53.

[95] L. Leibowitz, R.A. Blomquist, Int J Thermophys, 9 (1988) 873-883.

[96] B. Yarlagadda, Elevated Temperature Mechanical Properties And Corrosion Characteristics Evaluation Of Alloy HT-9, M.S. Thesis, Mechanical Engineering, University of Nevada, Las Vegas, NV, 2004.

[97] S.T. Oyama, The Chemistry of Transition Metal Carbides and Nitrides, Blackie Academic and Professional, New York, 1996.

[98] L.E. Toth, Transition Metal Carbides and Nitrides, Academic, New York, 1971.

VITA

Ickchan Kim received his M.S. in mechanical engineering from Texas A&M University, College Station in 2007 and his B.S. in mechanical engineering from In-Ha University, Incheon, Korea (R.O.K.) in 1999.

Ickchan Kim graduated with his Ph.D. in May 2011 at Texas A&M University in the Electrical Engineering Department specializing in solid state electronics, photonics and nano-engineering group under Dr. Wang, Haiyan.

Ickchan Kim may be reached at 546 Southwest Parkway Apt A, College Station, TX 77840. His email is ickchan.kim11@gmail.com.